Technische Universität München
TUM School of Engineering and Design

Prediction and Investigation of Rotating Stall in Axial Flow Compressors by means of High- and Low-Fidelity Methods

Dominik Schlüter

Vollständiger Abdruck der von der TUM School of Engineering and Design der Technischen Universität München zur Erlangung des akademischen Grades eines

Doktors der Ingenieurwissenschaften (Dr.-Ing.)

genehmigten Dissertation.

Vorsitzende:	Prof. Dr. Sophie Armanini
Prüfer der Dissertation:	Prof. Dr.-Ing. Volker Gümmer Prof. Dr.-Ing. Heinz-Peter Schiffer

Die Dissertation wurde am 02.09.2021 bei der Technischen Universität München eingereicht und durch die TUM School of Engineering and Design am 21.02.2022 angenommen.

To my family.

Abstract

Rotating stall is a disturbance in axial compressors arising at operating conditions beyond the stability limit of a stage. Mitigation is aggravated due to a lack of both, feasible prediction methods and knowledge about control possibilities. This thesis verifies the capability of a modified low-fidelity approach to predict rotating stall. Moreover, the impact of certain compressor features on the stall cell details is investigated allowing for the identification of underlying physical mechanisms.

In order to provide a numerical reference for the low-order method, results of high-fidelity computations of a one-and-a-half stage axial compressor are presented and validated against experimental findings. The simulations accurately predict the single-cell rotating stall with a discrepancy in speed and circumferential size by about 15% and 7.9%, respectively. Moreover, the calculations reveal a part-span tip-section stall covering a region between 85% and 100% blade span.

The selected low-fidelity approach resembles a narrow quasi two-dimensional section of the compressor tip region. The method reproduces the single-cell stall with a minimum deviation in rotational speed of about 14.9% with reference to the high-fidelity result. Despite a matching circumferential extent, overall the reduced method exhibits larger disturbances expanding into multiple rows. The discrepancy in speed is found to result from the difference in cell blockage. Based on the insights, the method is concluded to be more suitable for the prediction of large perturbations like full-span stall.

Using a design of experiments the impact of compressor shaft speed, guide vane angle and nozzle area ratio, representing the throttle setting, on rotating stall is investigated. Furthermore, the main drivers determining the stall cell details are identified. While the propagation speed is found to linearly correlate to the individual stall cell size, the cell count appears to depend on the ratio between disturbance size and compressor shaft speed.

Kurzfassung

Rotating Stall beschreibt eine Strömungsstörung in Axialverdichtern, welche eintritt, wenn der Betriebspunkt die Stabilitätsgrenze einer Stufe überschreitet. Die Mitigation ist durch das Fehlen praktikabler Vorhersagemethoden sowie fundiertes Wissen über mögliche Kontrollmechanismen erschwert. In dieser Arbeit wird das Potential eines modifizierten Low-Fidelity-Ansatzes zur Vorhersage von Rotating Stall überprüft. Darüber hinaus werden die Einflüsse unterschiedlicher Verdichterparameter auf die signifikantesten Eigenschaften der Stall-Zellen untersucht, sodass sich zugrundeliegende physikalische Mechanismen ableiten lassen.
Um die simplifizierte Methode mit einer numerischen Referenz vergleichen zu können, werden Ergebnisse aus High-Fidelity-Simulationen eines anderthalbstufigen Axialverdichters präsentiert und mittels experimenteller Daten validiert. Es wird gezeigt, dass die numerischen Rechnungen den einzelligen Stall korrekt abbilden. Die Abweichungen bezüglich der Umfangsgeschwindigkeit und -ausdehnung liegen bei 15% sowie 7.9%. Zudem geht hervor, dass die Stallzelle einen Bereich in Blattspitzennähe zwischen 85% und 100% der relativen Kanalhöhe einnimmt.
Der gewählte Low-Fidelity-Ansatz bildet eine schmale quasi-zweidimensionale Sektion des Schaufelspitzenbereichs ab. Die Methode gibt den einzelligen Stall mit einer maximalen Abweichung von 14.9% in der Ausbreitungsgeschwindigkeit bezogen auf die Referenzrechnung wieder. Trotz übereinstimmender Zellausdehnung in Umfangsrichtung weist das Modell größere Instabilitäten auf, welche sich axial bis in benachbarte Schaufelreihen ausbreiten. Die Diskrepanz in der Ausbreitungsgeschwindigkeit ist auf die Unterschiede in der Zellblockage zurückzuführen. Basierend auf den Erkenntnissen ist davon auszugehen, dass die Low-Fidelity-Methode zur Vorhersage großer Störungen wie *full-span* Stall besser geeignet ist.
Mittels einer statistischen Versuchsplanung werden die Einflüsse von Drehzahl, Leitradverstellung sowie Düsenquerschnittsfläche, welche den Drosselgrad repräsentiert, auf Rotating Stall untersucht. Daraus resultierend erfolgt die Identifikation physikalischer Haupttreiber. Während die Ausbreitungsgeschwindigkeit linear mit der individuellen Zellgröße korreliert, scheint die Anzahl der Zellen vom Verhältnis zwischen Zellgröße und Drehzahl abzuhängen.

Acknowledgements

The work presented in this dissertation was conducted in the research and development department at Siemens Energy AG in Mülheim an der Ruhr between May 2017 and April 2021. It would have never been completed, however, without the academic and administrative support of various institutions and individuals.
The author wishes therefore to express his sincerest appreciation for the guidance received from Dr. Robert Grewe who initiated and supervised this work. Moreover, the advice and encouragement of Professor Volker Gümmer is gratefully acknowledged.
Further special thanks are extended to Dr. Markus Raben, Dr. Gregor Schmid, Dr. Sebastian Hohenstein, Dr. Christian Cornelius and Dr. Sebastian Robens, who significantly enhanced the quality of both, computational and experimental results presented in this thesis by their invaluable experience. The administrative help and advice received from Dr. Dirk Nürnberger and Dr. Mirko Restemeier is greatly appreciated.
Thanks are also extended to Christian Kunkel and Jan Werner at Technische Universität Darmstadt for providing experimental data and insights into the measurements. The support and help by Dr. Fabian Wartzek in regards to coordinating the continuous exchange is gratefully acknowledged.
For the enlightening discussions and much needed sense of humour throughout this journey, the author would also like to thank his fellow PhD students at Siemens Energy as well as at Technical University of Munich. The assistance received from Anekan Gnanasampanthan is greatly appreciated.
Furthermore, the author wishes to express his deep gratitude to his family and close friends. Stays in Munich during workshops or seminars were only enabled by the hospitality of Maximilian Schuhbeck. The support and pleasant vacations in Salach and Turkey provided by Ahmet Menderes Ayral and his family have always been of tremendous value. The company of Siegfried Detert as well as Sandra, Jakob and Leonard Schlüter was in many ways uplifting. And finally, I am much obliged to my mother Annette Schlüter and my brother Torben Schlüter. Without your encouragement this would not have been possible.

Table of contents

Nomenclature **xi**

1 Introduction **1**
1.1 Challenges of rotating stall mitigation 3
1.2 Research scope and thesis outline 4

2 Fundamental compressor aerodynamics **7**
2.1 Stage flow 7
2.2 Performance map 8
2.3 Stall inception 10
2.3.1 Spike-type disturbances 11
2.3.2 Modal-type disturbances 12
2.4 Rotating stall 13
2.4.1 Classifications 14
2.4.2 Stall cell structure 15
2.5 Stage matching effects 17

3 Literature review **19**
3.1 Low-fidelity methods 19
3.1.1 Parallel compressor model 19
3.1.2 Small disturbance theory 21
3.1.3 Greitzer-Moore model 21
3.1.4 Two-dimensional and quasi two-dimensional approaches 22
3.1.5 Three-dimensional approaches 24
3.2 Rotating stall sensitivities 25
3.2.1 Flow coefficient 25
3.2.2 Compressor shaft speed 26
3.2.3 Stagger angles 27
3.2.4 Other parameters 27
3.3 Conclusions 28

4 Experimental method **33**
4.1 Rig overview 33
4.2 Compressor module 34
4.3 Instrumentation 35

5 Computational method **37**
5.1 Flow solver TRACE 39
5.2 Solver properties 39
5.3 Convergence criteria 40
5.4 Nozzle exit boundary condition 40
5.5 Geometry considerations 41
5.5.1 Circumferential extent 42
5.5.2 Axial extent 42
5.5.3 Hybrid models 43
5.5.4 Mistuning 43
5.6 Speedline process 44
5.7 Signal analysis techniques 45
5.7.1 Frequency spectra 45
5.7.2 Circumferential speeds 47
5.7.3 Circumferential modes 47
5.8 Conclusions 48

6 High-fidelity computations **51**
6.1 Steady simulations 51
6.1.1 Domain and boundary conditions 51
6.1.2 Computational grid 53
6.1.3 Post-processing considerations 55
6.1.4 Compressor performance 56
6.2 Unsteady simulations 59
6.2.1 Domain and boundary conditions 59
6.2.2 Compressor performance 60
6.2.3 Circumferential pressure distributions 63
6.2.4 Frequency spectra 64
6.2.5 Unsteady casing wall contours 67
6.2.6 Summary of rotating stall details 68
6.2.7 Spike-stall structure 70
6.2.8 Stall cell structure 71
6.3 Conclusions 72

7 Low-fidelity computations **75**
7.1 Methodology . . . 75
7.2 Performance characteristics . . . 77
7.3 Stall onset . . . 79
7.4 Pre-stall activity . . . 81
7.5 Stall cell speed and count . . . 84
7.6 Stall cell sizes . . . 87
7.7 Rotating stall sensitivities . . . 89
7.8 Conclusions . . . 91

8 Design of experiments **93**
8.1 Parameter space . . . 93
8.2 Performance characteristics . . . 95
8.3 Stall cell split-up . . . 96
8.4 Rotating stall size considerations . . . 98
8.5 Operational parameter impact . . . 99
8.5.1 Stall cell size . . . 99
8.5.2 Stall cell number . . . 101
8.5.3 Stall cell speed . . . 103
8.6 Fundamental mechanisms . . . 105
8.6.1 Stall cell size . . . 105
8.6.2 Stall cell number . . . 106
8.6.3 Stall cell speed . . . 108
8.7 Conclusions . . . 109

9 Transferability of findings **111**
9.1 Governing relations . . . 111
9.1.1 Individual blockage . . . 111
9.1.2 Relative blockage . . . 113
9.2 Parameter effects . . . 114
9.2.1 Shaft speed . . . 114
9.2.2 Stagger angle . . . 116
9.3 Conclusions . . . 117

10 Main conclusions and future work **119**
10.1 Main conclusions . . . 119
10.2 Future work . . . 122

Nomenclature

Abbreviations

2D	Two-dimensional
3D	Three-dimensional
ADP	Aerodynamic design point
BP	Blade passing
CFD	Compuational fluid dynamics
CPU	Central processing unit
DLR	German Aerospace Center
DoE	Design of experiments
EXP	Experiment
FB	Front boundary of stall cell
HCF	High cycle fatigue
Hifi	High-fidelity
LE	Leading edge
Lofi	Low-fidelity
NC	Near choke
NS	Near stall
OGV	Oulet guide vane
OP	Operating point
PSM	Passage spectral method
Q2D	Quasi two-dimensional
RANS	Reynolds-averaged Navier-Stokes
RB	Rear boundary of stall cell
RI	Rotating instability
ROI	Region of interest
RQ	Research question
RS	Rotating stall
SI	Stall inception
TE	Trailing edge
TL	Tip leakage
TRACE	Turbomachinery research aerodynamic computational environment
URANS	Unsteady Reynolds-averaged Navier-Stokes
VIGV	Variable inlet guide vane

VSV	Variable stator vane	

Greek symbols

α	Guide vane angle	[°]
γ	Rotor stagger angle	[°]
Δ	Difference or change, e.g. $\Delta\Omega_S$	
ϵ	Error or discrepancy	[%]
η_{is}	Isentropic efficiency	[-]
θ	Coordinate in circumferential direction	[°]
Θ_{RS}	Fraction of circumference occupied by rotating stall	[-]
Θ_t	Total-to-total temperature ratio	[-]
κ	Heat capacity ratio	[-]
λ_{RS}	Blockage factor	[-]
π	Propability	[-]
Π_t	Total-to-total pressure ratio	[-]
ρ	Density	[kg/m^3]
σ	Solidity	[-]
φ	Flow coefficient	[-]
φ^*	Flow coefficient in the unstalled portion of the annulus	[-]
χ_{RS}	Relative blockage	[-]
ψ	Total-to-static pressure rise coeffient	[-]
ω_{RS}	Individual stall cell speed	[Hz]
Ω_{RS}	Rotating stall frequency	[Hz]
Ω_S	Shaft rotation frequency with $\Omega_S = N/60$	[Hz]

Latin symbols

A	Nozzle inlet area	[m^2]
A^*	Nozzle throat area	[m^2]
D	Compressor diameter	[m]
DF	Lieblein diffusion factor	[-]
e	Euler's number	[-]
EO	Engine order	[-]
f	Signal frequency	[Hz]
g	Function	[-]
h_{rel}	Relative channel height or span location	[-]
h_t	Stagnation enthalphy	[m^2/s^2]
L_x	Axial row gap	[m]
$\dot{m}$	Mass flow rate	[kg/s]

$\dot{m}_{corr}$	Corrected mass flow rate	[kg/s]
M	Mach number	[-]
n_{RS}	Number of stall cells	[-]
n_S	Number of stages	[-]
N	Shaft rotation speed	[1/min]
p	Static pressure	[Pa]
p_t	Stagnation pressure	[Pa]
r	Coordinate in radial direction	[m]
r_h/r_t	Compressor hub-to-tip ratio	[-]
R	Ideal gas constant	[J/kgK]
R^2	Coefficient of determination	[-]
R_{xy}	Cross-correlation coefficient	[-]
t	Time	[s]
T	Period	[s]
T_t	Stagnation temperature	[K]
U	Rotor tip speed	[m/s]
v	Velocity in stationary frame	[m/s]
v_x	Velocity in axial direction	[m/s]
v_θ	Circumferential velocity in stationary frame	[m/s]
w	Velocity in rotating frame	[m/s]
w_θ	Circumferential velocity in rotating frame	[m/s]
x	Coordinate in axial direction	[m]

Subscripts

$\square_{0,1,2,3}$	Different states
$\square_{ex}$	Exit
$\square_{in}$	Inlet
$\square_{ISA}$	International standard atmosphere
$\square_{NC}$	Near choke conditions
$\square_{NS}$	Near stall conditions
$\square_{RS}$	Rotating stall quantity

Miscellaneous

$\square'$	Amplitude or fluctuation of a quantity
$\overline{\square}$	Averaged quantity
$\widehat{\square}$	Predicted quantity

Chapter 1
Introduction

Since the invention of the first jet engines by Frank Whittle (Britain) and Hans von Ohain (Germany) in the late 1930s, the gas turbine gained considerable importance in numerous fields of application. The most common examples are aircraft engines and heavy-duty industrial gas turbines for electric power generation. The enormous significance of the innovation can be properly appreciated considering the prosperity associated with it. Depicted in Figure 1.1-A is the growth in global energy consumption and air traffic during the past decades. Although the gas turbine can not be held accountable for enabling such an advance alone, it definitely contributed substantially.

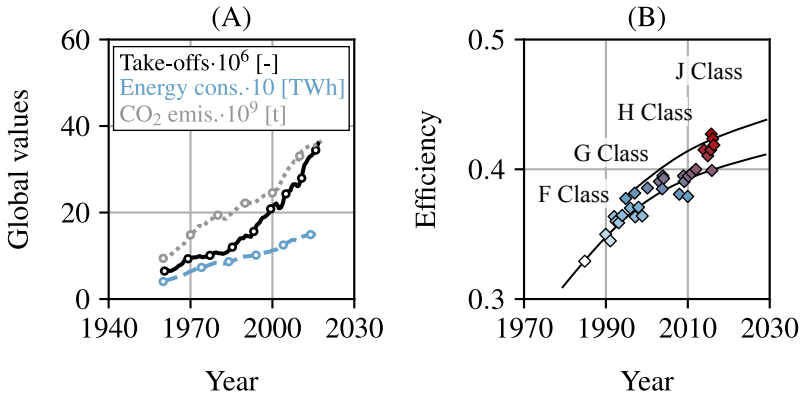

Figure 1.1: Review of global air traffic (Kaltschmitt and Neuling (2018) [1]), primary energy consumption and CO_2 emissions (Ritchie and Roser (2020) [2]) (A) as well as evolution of gas turbine efficiency (Gülen (2019) [3]) (B)

Due to the simultaneous increase of greenhouse gas emissions, also shown in Figure 1.1-A, the demands on future engine technologies increased immensely. Environmental sustainability has become a key factor in the course of climate protection setting the boundaries for prospective com-

petitiveness. Low emission level requirements confront both the aerospace and power generation industry with the challenge of higher efficiencies more than ever.
The increase in single-cycle gas turbine efficiency over time is illustrated in Figure 1.1-B. According to Lechner and Seume (2019) [4], it is accompanied by a trend towards higher compressor pressure ratios at a minimum number of stages. Gas turbines of the G/H-classes with pressure ratios of about 20 are already settled at 13 to 14 stages. This number will decrease even further through the technologies of upcoming generations with even higher delivery pressures. With respect to aircraft engines, a decreasing number of stages is especially desirable in terms of reduced size, weight and costs.

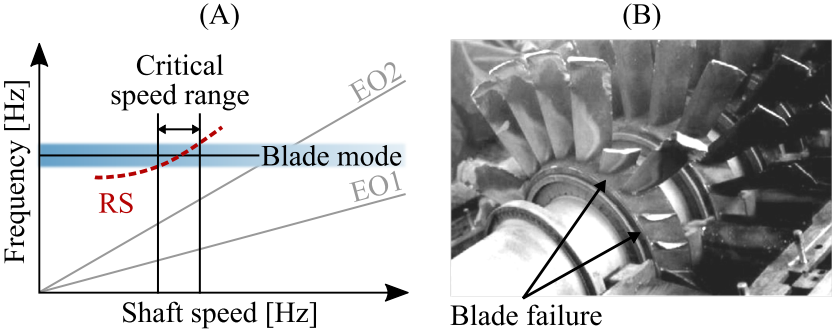

Figure 1.2: Campbell diagram with blade mode excitation through rotating stall (A) and image of failed blades taken from Luo and Wu (2016) [5] (B)

As a consequence of this trend, higher stage loadings lead to operating conditions closer to the stability limit. With it, the risk of emerging compressor instabilities rises. The most common phenomena are rotating stall and surge. Due to large safety margins, nowadays the latter is fortunately less likely to occur. Rotating stall (RS) on the other hand, is still a major concern, especially during engine start-up and shut-down. Stall cells, separated flow regions spread over blades, travel in engine rotation direction at a defined speed. As cell number and speed result in a determined angular frequency, rotating stall can induce severe blade vibrations. Figure 1.2-A illustrates a typical Campbell diagram with blade mode excitation

through rotating stall during an engine start-up. In addition, an exemplary case of rotating-stall-induced fatigue in an industrial compressor is given in Figure 1.2-B. Clearly visible is the first stage blade failure.
With structural fatigue and associated engine shut-downs posing a risk to manufacturers and customers, strategies of how to deal with rotating stall are of growing importance. For this reason, the unsteady phenomenon and associated challenges represent central topics of this work.

1.1 Challenges of rotating stall mitigation

The management of rotating stall in axial flow compressors has become a necessity in order to prevent unexpected excitations. Subsequently, the main challenges associated with the development of mitigation strategies are introduced. For clarification, they are broken down into two essential aspects, rotating stall prediction and control.

I. **Prediction:** During the design phase, accurately predicting the rotating stall onset, pattern and frequency is a delicate task. High-fidelity models applying unsteady full-wheel multi-stage computational fluid dynamics (CFD) are time consuming and CPU intensive. In other terms, they are not applicable in the day-to-day business. Feasible and reliable low-order methods, in turn, are yet not available. What remains are commercial CFD practices represented by single-passage steady-state approaches. As these have proven to be valid particularly near design conditions they are used in regards to compressor efficiency optimizations. Apart from that, stall margin predictions remain doubtful and instabilities irresolvable due to simplifications. Eventually, knowledge about compressor stall conditions is still derived from post-design engine tests.

II. **Control:** Assuming well-known stall conditions during design phases, the current unavailability of criteria dealing with instabilities would impede any prevention. Although many tests and studies have been carried out throughout the decades, the driving mechanisms determining the number of spatial modes and their propagation velocity are still unknown. One common approach to control rotating stall is using guide vane schedules adjusting the inflow conditions at part-speed. The principle idea is not to prevent the instabilities from emerging, but to alter the associated frequencies and suppress possible blade excitations. As

the exact impact of the guide vane setting on rotating stall is however unknown, finding an appropriate schedule is mainly based on trial and error during engine tests.

In summary, the main difficulties in terms of mitigating rotating stall are associated with a lack of a) feasible yet accurate prediction methods or models and b) detailed knowledge about the driving mechanisms controlling the disturbance characteristics.

1.2 Research scope and thesis outline

With the main challenges at hand, both scope and structure of this thesis are subsequently described.
In general, the work aims at tackling the current lacks associated with rotating stall mitigation. With respect to the unavailability of efficient prediction methods, the determination, development and examination of a suitable low-fidelity approach is pursued. By means of this method, larger sets of parameter investigations are then envisaged in order to expand the knowledge about what controls rotating stall. The objective is to identify both, the impact of selected compressor features and the underlying physical mechanisms determining rotating stall characteristics. In short, the following research questions (RQ) are defined for this work:

RQ 1.1 *What features are required for a promising low-fidelity method for RS prediction?*

RQ 1.2 *How capable is the derived low-order model to predict RS?*

RQ 1.3 *How do selected compressor parameters affect RS?*

RQ 1.4 *What are the underlying physical mechanisms controlling the RS characteristics?*

RQ 1.5 *Are the findings derived in this work universally applicable or constrained to certain cases?*

In order to answer the individual research questions, the thesis is subdivided into different chapters. Each of them deals with a distinct subject as illustrated in Figure 1.3.

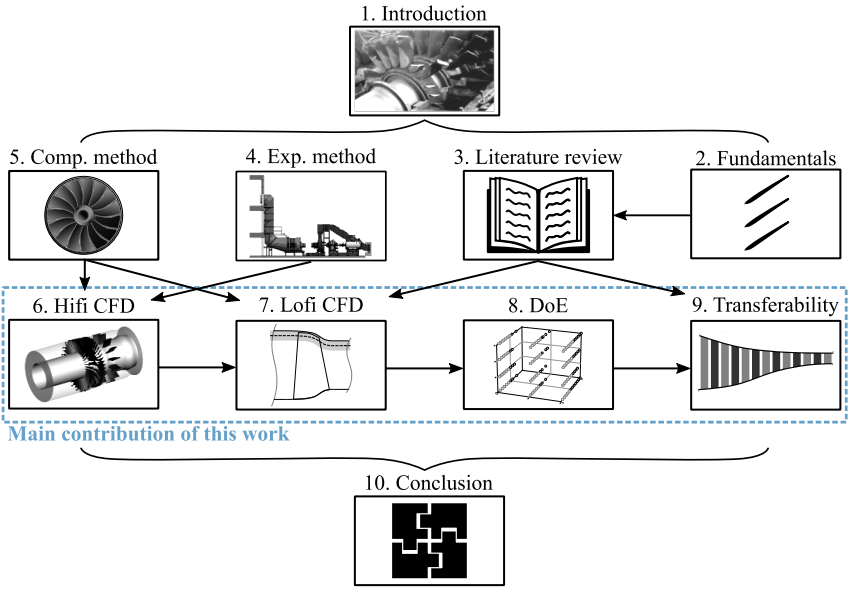

Figure 1.3: Thesis structure

After a brief recap of fundamentals in the field of compressor aerodynamics provided in Chapter 2, a review of relevant and available literature is presented in Chapter 3. The review focuses on computational and analytical approaches that have been applied to predict rotating stall. Additionally, a closer look is taken at parameter studies conducted in order to determine stall cell sensitivities towards various compressor features.
For an in-depth analysis of the low-fidelity approach derived in this work, a numerical reference is created by means of a high-fidelity model. Therefore, experimental data of measurements performed in a test rig, introduced in Chapter 4, and numerical strategies for accurate stall predictions, described in Chapter 5, are utilized. The high-fidelity results are subsequently presented in Chapter 6. Plausibility and accuracy of the computations is verified on the basis of the experimental findings.
From the insights gained in the literature review, a modified version of the most promising low-fidelity approach is described and investigated in Chapter 7. By comparing results from both, the high- and low-fidelity methods, capabilities and limitations of the reduced approach are verified.

Subsequently, a design of experiments is conducted in Chapter 8 in order to determine the impact of different compressor features on rotating stall. For this purpose, the low-fidelity model is applied. Moreover, the large dataset is used to identify some of the underlying physical mechanisms controlling the instability.
In Chapter 9, the findings are then compared to additional data from other compressor builds. The aim is to verify the generality of results and the transferability to other engines.
Finally, key conclusions and a possible outlook are provided in Chapter 10.

Chapter 2
Fundamental compressor aerodynamics

In this chapter essential aerodynamic features of single and multi-stage compressors are described. The following sections are therefore meant to provide basic knowledge about characteristic parameters and flow mechanisms relevant to this work.

2.1 Stage flow

The most important design components of a compressor are its blades and vanes. They impart momentum and turn the flow through pressure gradients. Figure 2.1 illustrates a generic compressor front stage. It includes three rows with inlet guide vanes, rotor blades and stator vanes.

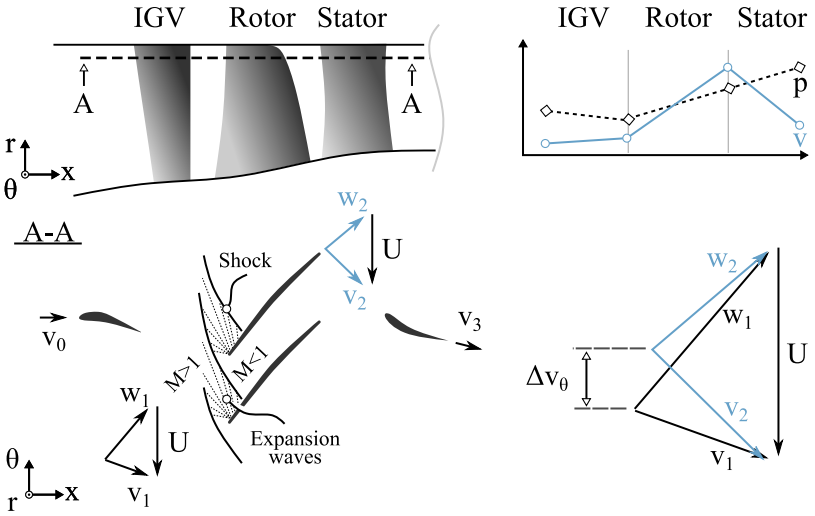

Figure 2.1: Principle function of a compressor stage

The section A-A in the tip region provides a view on the velocity triangles in between those rows. Absolute and relative velocity components are denoted by v and w. After passing the guide vanes, the flow direction is changed due to the geometry curvature. Pre-swirl is added to ensure a

proper level of rotor inlet Mach number conditions in the relative frame of reference. Although the flow is subsonic in the stationary frame of reference, the high circumferential blade speed U causes a supersonic rotor inflow at a Mach number $M > 1$. As a consequence, a pattern of shock and expansion waves occurs in proximity to the leading edges. At first, the flow passes the shock of the preceding blade and decelerates. Subsequently, due to the blade curvature, a Prandtl-Meyer expansion fan is induced accelerating the flow. When passing the following passage shock, the flow is again decelerated leading to subsonic exit conditions at $M < 1$. The decrease in relative velocity results in a deflection in the stationary frame. Depending on the number of stages, the subsequent stator vane then either ensures suitable conditions for the downstream rotor or removes the swirl when the compressor exit is reached.
Also depicted in Figure 2.1 are the magnitudes of the static pressure p and the absolute velocity v throughout the compressor. Within the guide vane row, the static pressure is slightly reduced while the velocity increases. The main reason for this is the decreasing passage throat area lowering the exit pressure and accelerating the flow. In the rotor, kinetic energy is added to the fluid and hence the velocity rises. The static pressure increases as a result of the passage shock. In the stator, the kinetic energy is converted into internal energy, leading to an increased static pressure and a reduced flow velocity.

$$\Delta h_t = U \cdot \Delta v_\theta \tag{2.1}$$

The energy transfer from blade to fluid Δh_t is defined by Euler's equation for turbomachinery (Eq. 2.1, Cumpsty (2004) [6]). Raising the energy input requires higher circumferential velocities U or deflections Δv_θ. The magnitude of both parameters, however, is limited. While the rotor speed cannot be increased infinitely due to mechanical loads, the maximum flow turning is constrained aerodynamically. Exceeding the aerodynamic stability limit will result in compressor stall.

2.2 Performance map

The performance of a compressor is mapped using a number of speedlines, often named characteristics. An example is illustrated in Figure 2.2 for a single-stage compressor. In general, the pressure rise is plotted against the

flow rate for different shaft speeds N. In terms of the output pressure level either the total-to-total pressure ratio Π_t or the total-to-static pressure rise coefficient ψ is applied. The flow function is represented by the corrected mass flow rate $\dot{m}_{corr}$ or the flow coefficient φ. The corresponding relations are provided by Equations 2.2 - 2.3.

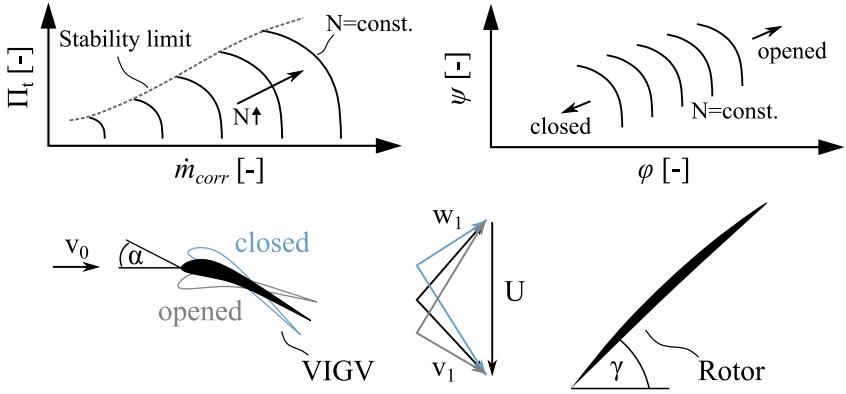

Figure 2.2: Performance map of a single-stage compressor and impact of the stagger angle on a constant speed characteristic

Reducing the mass flow rate at a constant speed increases the delivery pressure due to a higher flow turning. As the operating point moves further towards the left portion of the characteristic, losses and secondary flow effects arise. With the maximum deflection being constrained, the point at minimum mass flow rate denotes the aerodynamic stability limit. Beyond this point, at even lower mass flow rates, compressor flow instabilities occur.

$$\Pi_t = \frac{p_{t,ex}}{p_{t,in}} \qquad \text{and} \qquad \dot{m}_{corr} = \dot{m} \cdot \frac{p_{t,ISA}}{p_{t,in}} \cdot \sqrt{\frac{T_{t,in}}{T_{t,ISA}}} \tag{2.2}$$

$$\varphi = \frac{v_x}{U} \qquad \text{and} \qquad \psi = \frac{2 \cdot (p_{ex} - p_{t,in})}{\rho U^2} \tag{2.3}$$

Also indicated in Figure 2.2 is the impact of the guide vane (α) and rotor (γ) stagger angles on the compressor stage performance. Increasing the stagger angle is generally denoted as closing the row, while decreasing the parameter leads to opened vanes or blades. For a constant speed N,

opening the variable inlet guide vanes (VIGV) for example reduces the pre-swirl and leads to an increased flow incidence. As a result, the characteristic is shifted towards higher pressure rise coefficients ψ and flow coefficients φ. The opposite effect occurs when the VIGV is closed. The characteristic is influenced by the rotor stagger angle in a similar manner.

2.3 Stall inception

In this section the topic of stall inception is introduced, providing an overview of the initial flow mechanisms involved in compressor stall.
As previously described, the aerodynamic performance of a stage is constrained by the stability limit. The reason for this are flow perturbations arising as the inlet angle of the approaching air stream becomes too high. The resulting *stall* is generally associated with low axial absolute velocities and an increasing drag on the blade due to boundary layer separations on the suction side (Figure 2.3-A, Gülen (2019) [3]).

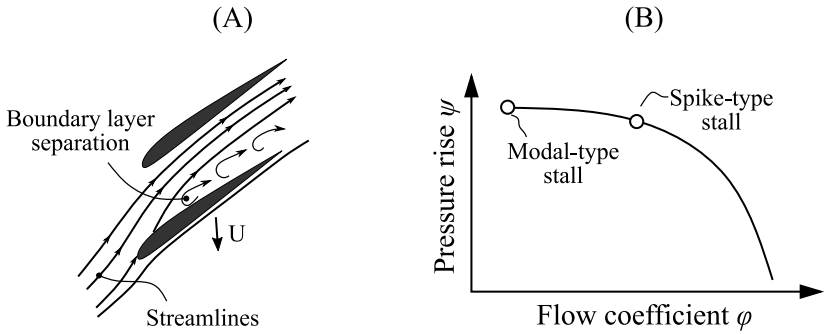

Figure 2.3: Beginning of stall in a blade row from Gülen (2019) [3] (A) and stall inception model based on Camp and Day (1997) [7] (B)

In order to increase the operating range of a compressor, the broad topic of stall inception focuses on understanding the mechanisms behind the onset of stall. The first theoretical explanation was given by Moore and Greitzer (1986) [8], postulating infinitesimal disturbances with length scales of the order of the compressor diameter. Later on, experimental evidence for the existence of these so-called modes was reported by McDougall et al. (1990) [9]. In addition to modal-type disturbances, McDougall et al.

(1990) [9] as well as Day (1993) [10] were able to observe a second type of stall precursor in their studies named spike. This form of disturbance is described as short length scale perturbation moving around the circumference and occurring as sharp peaks in the time-resolved velocity signals of the flow field.
A generic model indicating whether modal oscillations or spikes appear as stall precursor was reported by Camp and Day (1997) [7]. The basic idea is illustrated in Figure 2.3-B. Therein, a distinction between both perturbation types is based on the slope of the total-to-static pressure rise characteristic at the stall point. If the compressor reaches the stability limit while operating on the negatively-sloped portion, the stable flow breakdown is usually linked to spike-type inception. In case the characteristic reaches zero-slope before stall, a modal activity is involved. At this point, the slope can either be zero or slightly positive.

2.3.1 Spike-type disturbances

According to Camp and Day (1997) [7], Spike-type stall inception describes a stalling behaviour caused by transient perturbations of short length scale and large amplitude compared to the mean velocity. Due to their small circumferential extend of a few blade passages, spikes exhibit higher angular velocities than modal disturbances, initially between 60% and 80% of the shaft rotation frequency Ω_S. As they grow in size, their speed reduces leading to the development of rotating stall which usually happens within half a rotor revolution.
The first flow field image related to spike-type perturbations was proposed by Inoue et al. (2000) [11] describing a vortex tube that spans from blade to casing. By considering computational and experimental results, Pullan et al. (2015) [12] were able to extend the knowledge about this so-called tornado-vortex shown in Figure 2.4-A. In their findings, the vortical disturbance originally emerges from a leading edge separation caused by a locally high flow incidence. From the vorticity shed by this separation, the tornado-type disturbance is formed with its upper end on the casing and the lower end on the blade's suction side. With the following blade passing through the vortex, a new leading edge separation is triggered, resulting in the convection of the spike. The combination of regions with high static pressure in front of the flow separation and low static pressure on the compressor casing leads to the typically sharp up-down signature

detected by upstream probes (see Fig. 2.4-B).
Despite the common believe that spike-type stall inception is a highly three-dimensional phenomenon due to the radial and circumferential extend of the tornado-like vortex, Pullan et al. (2012) [12] were also able to evince spikes in a two-dimensional cascade. Furthermore, the vortical disturbance appears not to be tied to the presence of tip leakage flow as it was found to occur in blade rows with and without tip clearance. The geometrical feature, however, can play a role in triggering the initial leading edge separation, as the tip leakage flow may increase the local flow incidence.

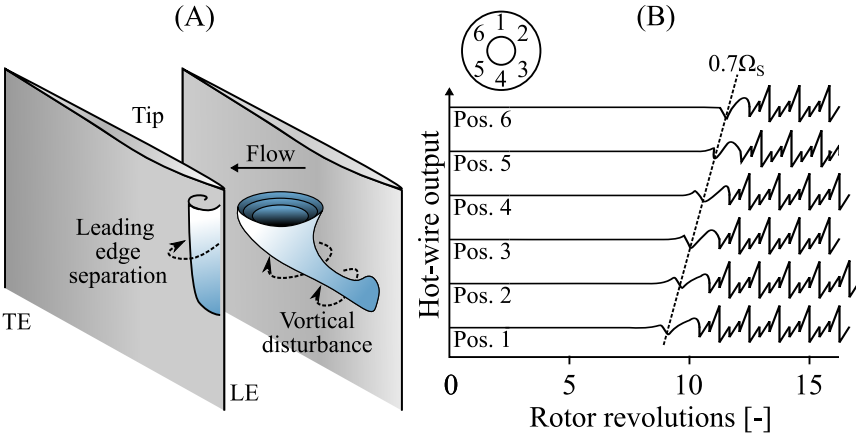

Figure 2.4: Schematic representation of the spike-type stall inception mechanism based on Inoue et al. (2000) [11] and Pullan et al. (2015) [12] (A) and associated signals acquired by hot-wires placed around the annulus (B).

2.3.2 Modal-type disturbances

As described before, modes are disturbances which usually appear with a wave length equal to the rotor circumference. They can be seen as solely two-dimensional oscillations of the whole compressor flow field. A schematic representation of a first order mode is given in Figure 2.5 together with exemplary signal traces captured by circumferentially positioned hot-wires.

In their studies, Camp and Day (1997) [7] stated that the rotation frequency of modes is generally below 50% of the rotor speed. With comparatively small magnitudes, the oscillations rarely exceed 2-3% of the freestream velocity. As modal disturbances gradually build up in time, however, they can eventually give rise to flow separations in multiple blade passages transitioning into a finite rotating stall cell. The time between the first sign of an undulation until the occurrence of rotating stall may take several revolutions. The final amplitude a mode will reach before stall occurs depends on how much loading any particular blade row can sustain before becoming critically overloaded.

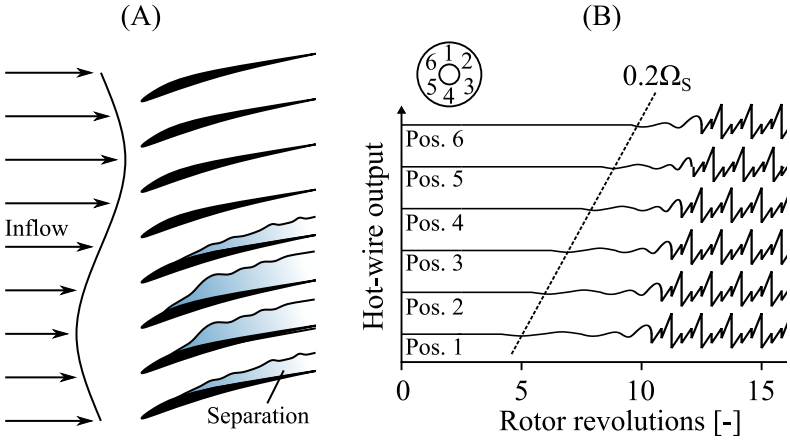

Figure 2.5: Scheme of a modal-type oscillation based on Day (1993) [10] (A) and associated signals acquired by hot-wires placed around the annulus (B).

2.4 Rotating stall

In proximity to the stability limit, stall inception is initiated by flow perturbations of different length scales. As the initial disturbances grow in size rotating stall emerges. In the following sections, the unsteady phenomenon is presented in greater detail.

In general, rotating stall describes a non-axisymmetric disturbance in axial compressors arising at operating conditions beyond the stability limit of a stage. The unsteadiness typically manifests itself as one or more

regions of retarded flow dividing the annulus into defined stalled and unstalled sectors. The instabilities referred to as stall cells travel in engine rotation direction at a defined speed. As the stall cell number n_{RS} and the individual cell speed ω_{RS} result in a determined angular frequency Ω_{RS}, rotating stall can induce severe blade vibrations. The relation specifying the rotating stall frequency is represented by Equation 2.4.

$$\Omega_{RS} = n_{RS} \cdot \omega_{RS} \tag{2.4}$$

According to Day (2015) [13], a compressor that is stalled repetitively at otherwise fixed boundary conditions will stall in the same manner each time. This means, the stall point, the number of stall cells and their speed will remain unchanged.

2.4.1 Classifications

In order to provide a basic overview, the different kinds of rotating stall are introduced. Typically, a distinction is made between two types or patterns. These are *abrupt stall* and *progressive stall* which are both illustrated in Figure 2.6-A.

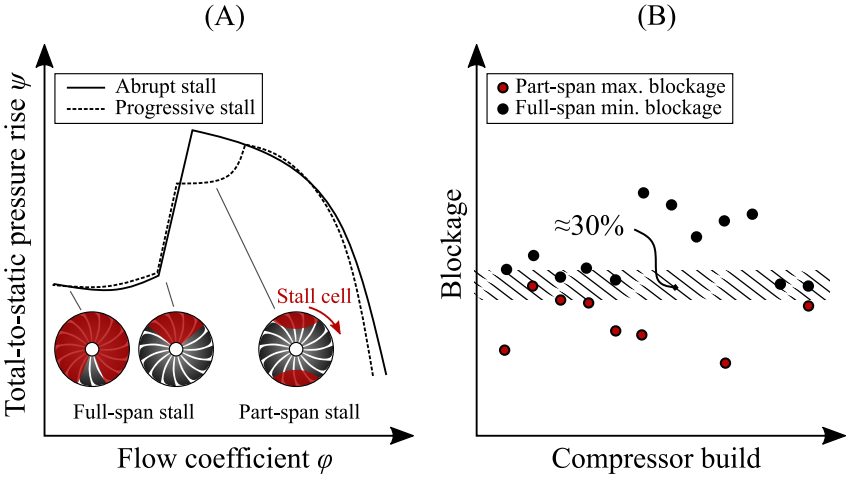

Figure 2.6: Classification of rotating stall types based on Grieb (2009) [14] and Day et al. (1978) [15]

Progressive stall is characterized by a gradual drop in pressure rise and

flow coefficient at the stability limit. The emerging stall cells cover several blades on a portion of the annulus height, wherefore this formation is denoted as part-span stall. The number of part-span cells can vary, but is usually found to be more than one. Although in this example illustrated at the blade tip, they can also emerge at the hub.
At even smaller flow rates, the pressure rise exhibits a large drop accompanied with a change in rotating stall type. The arising full-span stall is known to cover a large sector of the annulus over the complete radial height. It usually consists of a single cell increasing in circumferential size while the compressor is further throttled at an almost constant pressure rise. The transition from part-span to full-span stall occurs as the stalled portion of the annulus exceeds a value of approximately 30%. The empirical correlation was found by Day et al. (1978) [15] and is based on stall data of multiple axial compressors (see Figure 2.6-B).
Unlike progressive stall, abrupt stall is associated with the discontinuity in pressure rise and flow coefficient already occurring at the stability limit of the stage. As the delivery pressure drops, the compressor instantaneously exhibits the single-cell full-span rotating stall.

2.4.2 Stall cell structure

A first conceptional description of the flow field associated with rotating stall was introduced by Emmons et al. (1955) [16]. The essential parts of the famous sketch are included in Figure 2.7-A. The principle idea behind this illustration is to consider some blade passages to be blocked by flow separations due to high incidence. The incoming flow is influenced by the upstream effect resulting in different inflow angles along the cell leading edge. While the incidence on the right-hand side is decreased leading to improved conditions, it is increased on the left part. As a consequence, a flow separation is triggered on the approaching blade. As this mechanism continues, the cell propagates in opposite rotor direction in the relative frame. In the stationary frame, the cell moves in shaft rotation direction, but only at a fraction of the rotor speed.
Until extensive effort in respective measurements was undertaken, stall cells were considered as dead wakes similar to the flow behind a solid body. This would imply, that the cell edges are oriented according to the streamlines surrounding them. Day (1976) [17] was the first to establish a different theory supported by results from various compressor rig tests.

As the rotor blades transport fluid from one cell side to the other (Figure 2.7-A), they can be seen as highly energetic and active rather than passive regions.
Considering a part-span stall cell in the meridional plane, the fluid is forced to move in both the positive and negative axial direction. A fraction of the flow dives below the stalled region and enters the rotor at the hub. After emerging from the trailing edge, the flow velocity is comparatively small and predominantly tangential. The other fraction of the fluid entering the stalled region is centrifuged towards the tip in a recirculatory fashion. Day (2015) [13] pointed out, that the three-dimensional nature of the cells results in increased casing pressures and potential tip rubs.
Recent studies by Dodds and Vahdati (2015) [18] eventually gave more insights into the three-dimensional structure of cells as illustrated in Figure 2.7-B. Clearly visible is the vortex-like pattern similar to the tornado-vortices in the context of spike-type stall inception. In contrast to spikes, however, the rotating stall vortices block multiple blade passages.

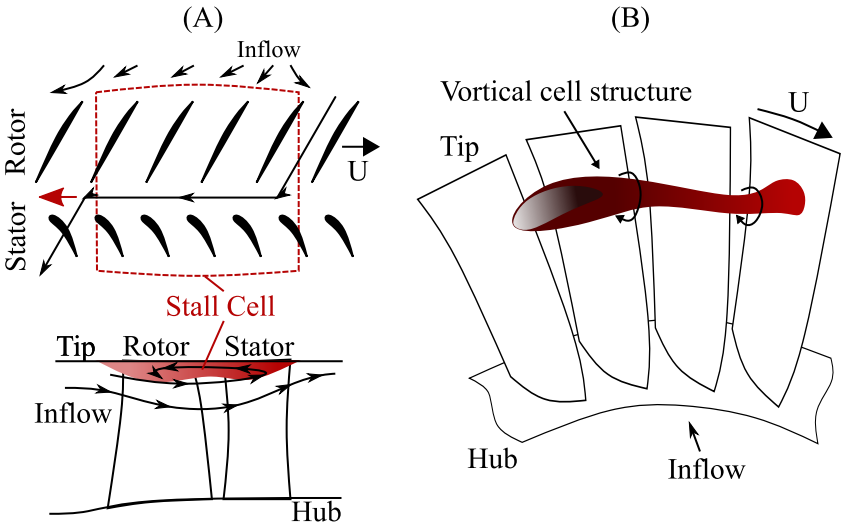

Figure 2.7: Stall cell flow in the relative frame of reference based on experimental findings by Emmons et al. (1955) [16] and Day (1976) [17] (A) and three-dimensional structure derived from computational results by Dodds and Vahdati (2015) [18] (B)

2.5 Stage matching effects

In the previous parts, solely the performances of single-stage compressors have been considered. Real engine compressors, however, act as a group of multiple stacked stages, implying that the overall matching is of high importance. Figure 2.8-A illustrates a schematic performance map of a multi-stage compressor. Shown is the overall total-to-total pressure ratio Π_t against the corrected inlet mass flow rate $\dot{m}_{corr}$ at different shaft speeds N. Also included are lines of constant isentropic efficiency η_{is} defined by Equation (2.5). The working line denotes the path a compressor operates on during ramp-up or shut-down. Along this line, the shaft speed is continuously increased, as are the mass flow rate and the total pressure ratio. At the aerodynamic design point (ADP), the compressor operates at highest realisable efficiency.

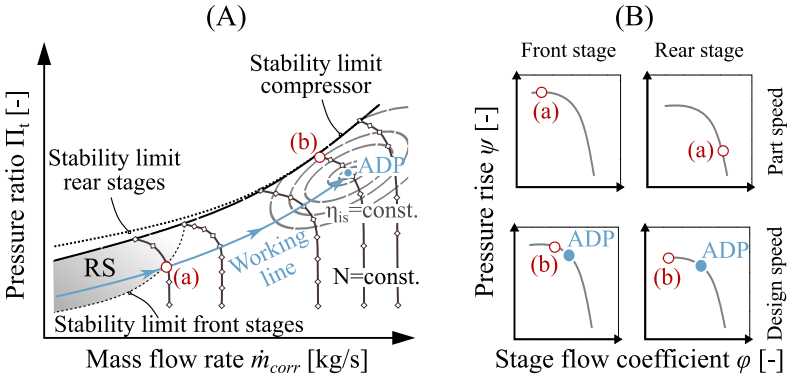

Figure 2.8: Exemplary multi-stage compressor map based on Bräunling (2001) [19] (A) and associated stage matching effects as depicted in Cumpsty (2004) [6] (B)

Also depicted in Figure 2.8-A are different stability limits of the compression system. The line along the pressure rise maxima is denoted as the limit of the whole compression system or *surge line*. Different from single-stage test rigs, exceeding this limit will result in compressor surge instead of rotating stall. The reason for this is the impact of large plenum volumes like combustion chambers on the whole system. As surge is not an important aspect of this thesis, it will not be discussed in further detail. Additional information on the subject can be found in the pertinent litera-

ture.
Besides the surge line, the aerodynamic stability limit of the front stages is depicted in the performance map. In multi-stage compressors, each row can locally exceed the individual stall limit at off-design conditions, while the compressor as a whole remains stable, see Longley and Hynes (1990) [20]. More insight is provided by Figure 2.8-B, illustrating the front and rear stage performance at part and design speed. With respect to lower compressor speeds, especially the front stages are prone to stall. Considering the large cross-sectional area at the compressor entry plane, the circumferential velocities in the first stages are comparatively high. In combination with low axial velocities, the flow coefficient φ becomes small, moving the operating point denoted as (a) towards the stall limit. For this reason, the front stages are often observed to exhibit rotating stall during engine starts.

$$\eta_{is} = \frac{\Pi_t^{\frac{\kappa-1}{\kappa}} - 1}{\Theta_t - 1} \qquad \text{with} \qquad \Theta_t = \frac{T_{t,ex}}{T_{t,in}} \tag{2.5}$$

At higher speeds, each row can be seen to operate near its efficiency maximum in the ADP. In this regime, however, the rear stages can be subject to unfavourable flow conditions. Moving the operating point away from the ADP towards point (b) at higher pressure ratios will increase the coefficient ψ significantly in the rear stages. The reason for this is the cumulative increase in the pressure ratio with each stage. Accompanied with the high back pressure and density are small axial velocities leading to a decreased flow coefficient φ. As a result, the operating point crosses the individual stability limit of the last stages. Due to the high discharge pressures, the flow breakdown in the downstream stages usually leads to the onset of surge instead of rotating stall. Hence, the stability limit of the rear stages coincides with the boundary of the whole compression system towards higher speeds.

Chapter 3
Literature review

In this chapter the focus is put upon studies published in the available open literature dealing with rotating stall prediction methods and sensitivity studies.
Of particular interest are reduced-order models used to forecast and study compressor instabilities. Important factors are their applicability, accuracy and possible limitations.
Moreover, numerical and experimental investigations on rotating stall sensitivities towards compressor operation and design parameters are presented. The knowledge about dependencies and correlations is considered crucial in order to determine mechanisms controlling the instability.
In general, the following research questions are ought to be answered in this chapter:

RQ 3.1 *What kind of low-order methods have been derived to predict rotating stall, how successful were they and what features did they incorporate?*

RQ 3.2 *Which parameters were found to influence rotating stall and in what way do they affect its characteristics?*

3.1 Low-fidelity methods

At this point, different analytical and computational low-order methods are presented and discussed.

3.1.1 Parallel compressor model

The parallel compressor model was first published by Day et al. (1978) [15] and aims at estimating the compressor performance in rotating stall. The basic idea is to consider the annulus as divided into stalled and unstalled sectors.
While the flow rate in a stall cell is almost zero, the flow through the unstalled portion is above average. With this in mind, the compressor can be assumed to simultaneously operate at two different conditions B and C

as illustrated in Figure 3.1. Both points are located at equal values of the pressure rise coefficient ψ since the static exit pressure behind both sectors, stalled and unstalled, is assumed to be identical. The combination of both points B and C eventually leads to the averaged post-stall operating point A.

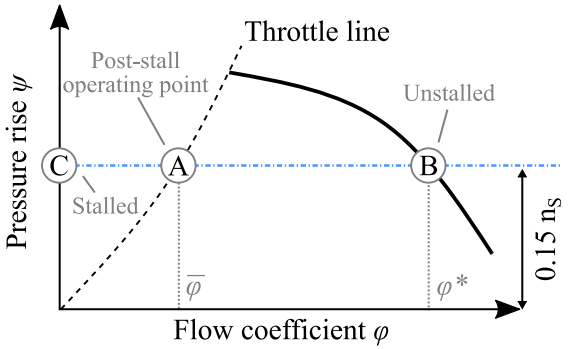

Figure 3.1: Estimated compressor performance based on the parallel compressor model by Day et al. (1978) [15]

By testing different multi-stage compressors, the pressure rise at stalled conditions was found to be almost independent of the compressor design. As main driver the number of stages n_S was identified. Using the correlation published in Day (2015) [13], the location of the horizontal line can be estimated to ψ=0.15n_S.
The distances along the horizontal line AB and CB also allow for the determination of the stalled portion of the compressor annulus. In general, the so-called blockage factor is calculated by λ_{RS}=AB/CB. As the distances involve the average flow coefficient $\overline{\varphi}$ and the flow rate through the unstalled portion φ^*, the blockage factor is defined by Equation 3.1.

$$\lambda_{RS} = \frac{\varphi^* - \overline{\varphi}}{\varphi^*} = 1 - \frac{\overline{\varphi}}{\varphi^*} \tag{3.1}$$

In combination with the knowledge about the critical blockage value of 30% as presented in section 2.4.1, the type of rotating stall in the compression system can be estimated. In case λ_{RS}<30%, part-span stall is likely to be present, otherwise full-span stall can be assumed.

3.1.2 Small disturbance theory

A fairly successful relation approximating the rotational speed of stall cells was published by Cumpsty and Greitzer (1982) [21] and subsequently improved by Moore (1984) [22]. Herein the impact of several compressor parameters like rotor stagger angle γ, number of stages n_S, axial row gap L_x, compressor diameter D as well as internal and external net lags m/k is taken into account. Furthermore, the propagation velocity is considered to depend on the number of stall cells n_{RS} since single full-span cells were observed to move at lower speeds than multiple part-span cells. The respective expression is represented by Equation 3.2.

$$\frac{\omega_{RS}}{\Omega_S} = \frac{0.5}{1 + \frac{m}{k}\cos^2(\gamma)\frac{D}{4n_{RS}n_S L_X} + \frac{0.5(1+\cos^2(\gamma))}{n_S}} \tag{3.2}$$

A main feature of this model is that the propagation speed ω_{RS}/Ω_S reaches an asymptotic value of 0.5 as the number of stages increases. This result is based on Cumpsty and Greitzer (1982) [21] who stated that in multi-stage compressors propagation velocities never exceed 50% of Ω_S. Larger stagger angles or respectively small design flow coefficients will lead to higher cell velocities. The influence of guide vanes, in turn, is little or even negligible. The given relation was found to be in good agreement with experimental data despite its simplicity. Nevertheless it is constraint to concrete cases with single-cell full-span stall. Agreement for stall patterns exhibiting multiple zones was concluded to be more or less fortuitous.

3.1.3 Greitzer-Moore model

Although not applied in this thesis, the Greitzer-Moore model is considered as an important milestone in the field of rotating stall research and therefore briefly presented.
Based on the analytical studies published in Moore (1984) [22, 23, 24], a low-order model predicting the post-stall transients of low-speed axial compression systems was proposed in Moore and Greitzer (1986) [8] and Greitzer and Moore (1986) [25]. The model assumes an axisymmetric or cubic performance characteristic and describes the dynamic response of multi-stage compressors during stall and surge. The two-dimensional representation of the unsteady flow involves a set of three non-linear differential equations derived from a Galerkin approximation. The corresponding

relations yield the pressure rise, the average flow coefficient as well as the rotating stall amplitude as a function of time. The model has been widely used to model the operating conditions in stall or surge and was applied to study parameter effects on the stalled performance branch in e.g. Backi et al. (2016) [26], Hõs et al. (2003) [27] or Gravdahl and Egeland (1997) [28].

3.1.4 Two-dimensional and quasi two-dimensional approaches

While analytical models are beneficial in terms of applicability, they lack detailed information about the fluid dynamics inside stalled blade rows. Consequently, a wide variety of two-dimensional (2D) and quasi two-dimensional (Q2D) computational approaches has been developed especially in the early years of CFD. The basic idea is to extract the blade shapes at a predefined span location of the original three-dimensional (3D) geometry and compute the flow conditions within a blade-to-blade domain. An example is given in Figure 3.2. The difference of a quasi two-dimensional method in comparison to a two-dimensional approach is associated with the slice width. In a Q2D domain, the radial flow component is for the most part negligible, however not completely absent due to a marginal radial extent Δr.

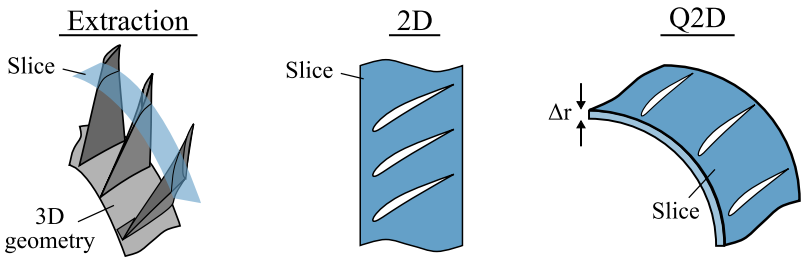

Figure 3.2: Schematic representation of two-dimensional and quasi two-dimensional computational domains

In the following, different studies applying 2D and Q2D methods are presented. Due to the large variety, only those methods validated against experimental data are considered.
Nishizawa and Takata (1994) [29] studied rotating stall in a two-dimensional finite pitch cascade by means of a vortex method. The results were com-

pared to experimental data reported in Kriebel et al. (1960) [30]. Although the numerical procedure did not match the original cascade geometry, features such as pitch-to-chord ratio, stagger angle and Reynolds number were almost the same. The data was found to be in acceptable agreement regarding the circumferential stall cell size of 4 to 5 blade pitches with a difference in cell propagation velocity of -8% relative to the circumferential velocity component v_θ.

Outa et al. (1994) [31] conducted both, numerical and experimental investigations of a single-stage low-speed compressor rig. The two-dimensional computational model included the rotor and stator geometries at 66.5% span. The blade-to-vane count ratio was reduced from 37:62 to 6:10. To keep the original solidity, the stator vanes were slightly enlarged. The numerical code was designed to solve the unsteady compressible Navier-Stokes equations for perfect gas. Depending on the loading position, different types of rotating stall were observed. Besides deep stall comprising both blade rows, the computations exhibited rotor as well as stator stall independently. At deep stall conditions, the difference between calculated and measured cell speed was about +10% relative to the rotor speed. It was concluded, that the blade count restriction prevented the stall cell from growing and therefore decelerating.

By means of an unsteady two-dimensional Euler approach, Saxer-Felici et al. (1999) [32] investigated rotating stall in a four-stage low-speed compressor. The numerical domain was reduced to a single stage including half of the original blade and vane counts. The geometries corresponded to a cut at the root-mean-square Euler radius of the four-stage compressor. Despite the differences, both, the experiment and the computation exhibited one full-span stall cell with a consistent blockage factor λ_{RS} between 31% to 46%. The cell propagation speed in the CFD was slightly higher by about +8% relative to the rotor speed.

More recent studies by Ferlauto and Taddei (2015) [33] made use of a quasi two-dimensional mean radius model. While the flow inside the compressor was solved by means of the Euler equations, blade rows were represented by non-linear actuator disks. Loss and deviation models relying on empirical correlations were applied to ensure realistic operating conditions in the stalled regime. Validation of the code was based on the experimental results of a transonic rotor reported in Seyler and Gostelow (1967) [34]. Four different rotor speeds were investigated with the nu-

merical procedure predicting the propagation speed of the full-span stall remarkably well. The relative error between numerical and experimental results ranged from -4% to -10% based on the rotor speed. However, as the model required the induction of initial flow perturbations for rotating stall to emerge, the unsteady Euler equations gave rise to multiple possible solutions. The stall cell count relied heavily on the number of initial perturbation spots.
In summary, both the 2D and Q2D methods predicted the rotating stall characteristics strikingly well with matching stall cell counts and a maximum discrepancy in relative cell speed of about 10%. Especially in consideration of those simplifications additionally introduced into the models like e.g. reduced row and blade counts, loss correlations or Euler solvers. The accuracy of the approaches can hence be assumed to increase as these simplifications are omitted. Furthermore, the methods were solely validated against full-span rotating stall, a disturbance on a large scale. As the models, in turn, resembled only a narrow slice, characteristics of smaller disturbances like part-span rotating stall might be predicted even better.

3.1.5 Three-dimensional approaches

Besides two-dimensional methods, some works introduced higher-order models considering the three-dimensional nature of compressor flows.
Righi et al. (2018) [35] developed a 3D through-flow method resolving rotating stall and surge in axial compressors. The code was based on the cylindrical Euler equations including a body force approach to mimic the presence of blades. Performances were captured through empirical correlations and a flow recirculation model. Validation was done against test data of a low-speed three-stage compressor reported by Eastland (1982) [36] and Gamache (1985) [37]. Good agreement was found with respect to the single-cell full-span rotating stall. As the model required little computational resources, the complete stalled branch of a constant speed line could be obtained. The maximum relative difference between calculated and measured cell speed was approximately -6%. The trend of increasing circumferential cell extent with diminishing flow coefficient was captured accurately.
A passage-spectral method (PSM) for unsteady flows was utilized by Romera and Corral (2019) [38]. Based on the Navier-Stokes Equations, the approach required only a small number of blade passages, reducing

the computational time by a factor of 3 to 7. By using spatial Fourier coefficients, the flow variables at the periodic boundaries were continuously readjusted. The method was validated against experimental (steady) and CFD (stall) data of the NASA rotor 67. The results revealed a good agreement of the PSM with the full-annulus CFD. The method accurately matched the number of stall cells, whereas the difference in cell speed was not stated precisely.
In general, the presented three-dimensional methods are associated with high model complexities. The implementation either requires access to the source code of an existing solver or a design from scratch.

3.2 Rotating stall sensitivities

In this part, a review with focus on rotating stall sensitivities towards compressor parameters is presented. The main objective is to identify influences on the stall cell speed ω_{RS}, count n_{RS} and size. The latter is either assessed on the basis of the previously introduced blockage factor λ_{RS} or the disturbance extent in circumferential direction Θ_{RS}.
Despite the variety of features a compressor incorporates, a closer look is especially taken at the impact of the shaft speed Ω_S, the flow coefficient φ and the stagger angles α and γ. The reason for this is the fact, that these parameters have been the primary subject in most studies.
Furthermore, it has to be considered that the majority of investigations was conducted experimentally as the application of computational fluid dynamics for parameter studies in this field is still cumbersome.
A general overview of the literature included in this review is presented in Tables 3.1 and 3.2. They are divided into investigations of single- and multi-stage builds, respectively.

3.2.1 Flow coefficient

The effect of the flow coefficient φ on the rotating stall attributes has been reported extensively. The most unequivocal impact was determined with respect to the disturbance size. In accordance with the definition of the blockage factor λ_{RS} (see Eq. 3.1), the disturbance extent was repeatedly observed to increase linearly towards reduced flow rates in Ref. [39], [40], [41, 42], [36], [37], [43] and [17].
With respect to the cell speed, the influence is less clear. In general, ω_{RS}

is assumed to diminish with φ due to the increase in disturbance size. As stated by Day (2015) [13], larger perturbations usually rotate at lower speeds. The observation is supported by studies published in Ref. [44], [41, 42], [45] and [36]. A different correlation, in turn, was reported in Ref. [40], [37], [43] and [17]. After an initial decrease of cell speed with disturbance size, the cell speed began to increase again.
For the number of stalled zones, a decrease towards diminishing flow coefficients was reported by Costilow and Huppert (1956) [44]. Apart from that, the stall cell count was either reported to remain constant by Hickman and Morris (2017) [41, 42], Eastland (1982) [36], Gamache (1985) [37] and Day (1976) [17] or observed to vary between different states by Tanaka and Murata (1975) [40] and Lavrich (1988) [43].
Overall, conformity in the observations is only found for the effect of the flow coefficient φ on the stall cell size. With respect to the impact on the stall cell speed and number, ambiguous results have been reported. Hence influences and trends are not clearly identifiable.

3.2.2 Compressor shaft speed

The compressor shaft speed Ω_S has mainly been investigated in order to understand its impact on the stall cell speed ω_{RS}. Studies on single-stage builds were performed by Choi et al. (2011) [46, 47] and Day (2015) [13]. While the former observed an increase in ω_{RS} with Ω_S, the latter did not identify any substantial impact. With respect to multi-stage compressors, investigations were reported in Huppert et al. (1954) [48], Dodds and Vahdati (2015) [49, 18] and Dodds (2016) [50]. Similar to the single-stage builds, different observations were made. While in Huppert et al. (1954) [48] as well as in Dodds and Vahdati (2015) [49, 18] the stall cell propagation velocity can be noticed to increase with compressor speed, Dodds (2016) [50] later concluded an only minor impact.
With respect to the number of stall cells n_{RS}, no variations were observed in the single-stage investigations by Choi et al. (2011) [46, 47]. The data reported by Huppert et al. (1954) [48] in contrast, indicates an increasing disturbance count towards higher speeds. A similar observation is made for the rotor tip stall reported in Dodds and Vahdati (2015) [49]. For the stator hub stall, in turn, the number of cells was seen to first increase and then decrease again at compressor ramp-up.
The impact of the shaft speed on the disturbance size was briefly discussed

in Choi et al. (2011) [46, 47]. The effect, however, appears to be negligible.
In summary, no clear influence of the compressor speed on the stall cell characteristics is determinable due to varying observations. A particular problem associated with changes in Ω_S is the direct impact on the flow coefficient φ (see Eq. 2.3). Increasing the circumferential speed will always affect the flow coefficient simultaneously. Consequently, separating and correctly assigning the influences of both parameters on rotating stall is aggravated.

3.2.3 Stagger angles

At this point, the impact of both blade (γ) and vane (α) staggers is presented. The former was mainly studied in single-stage builds. While the data in Fabri and Siestrunck (1957) [39] indicates almost no impact of γ on ω_{RS}, Day (2015) [13] reported a slight increase in cell speed for closed blades. In addition, Fabri and Siestrunck (1957) [39] reported shrinking disturbances for increasing rotor stagger angles. The effect, however, is influenced by the flow coefficient and diminishes at low values of φ.
The guide vane angle α was investigated by Costilow and Huppert (1956) [44] and observed to neither have impact on the cell speed nor the number of stall cells. A different picture was presented by Dodds (2016) [50]. For rotor tip stall, closed vanes were found to increase the cell speed while the opposite behaviour was seen for stator hub stall.
Similar to the compressor shaft speed, identifying the stagger effect on rotating stall is aggravated due to the simultaneous impact on the operating point and hence flow coefficient. Dodds (2016) [50] pointed out, that the observed changes in cell speed ω_{RS} may rather be assigned to the variation in axial velocity caused by the guide vane angle adjustments.

3.2.4 Other parameters

Besides those parameters presented above, additional features were studied in the past.
The axial row gap L_x in single-stage compressors for example was investigated by Tanaka and Murata (1975) [40] and Day (2015) [13]. In both works, increasing the row spacing is seen to increase the stall cell speed ω_{RS}. Moreover, the stall cell count and disturbance size appear to increase

for larger values of L_x.
Also studied by Tanaka and Murata (1975) [40] was the hub-to-tip ratio r_h/r_t. In general, increasing the parameter can be concluded to increase the likelihood of full-span stall after stall inception. According to this, larger blockage factor λ_{RS} and overall cell sizes can be expected. In addition, the number of stall cells and their propagation speed are found to reduce towards higher values of r_h/r_t.
In Day (1976) [17] and Day (1978) [15] a high number of stages n_S was concluded to increase both, the stall cell speed and size.
Parameters without significant impact on the propagation speed ω_{RS}, in turn, were found to be the tip clearance and the overall blade profile in Day (2015) [13].

3.3 Conclusions

In this chapter a review of available publications on the topics rotating stall prediction and control was presented. Different analytical low-order models and methods were discussed in order to assess their suitability for rotating stall predictions. Furthermore, studies were shown in which selected compressor features were varied with the aim to identify related stall cell sensitivities.
In summary, the key findings referring to the initial research questions of this chapter are as follows:

3.1-1 In the course of rotating stall research, analytical models based on empirical correlations as well as two-dimensional and more recently three-dimensional computational approaches have been developed.

3.1-2 For the prediction of the stall cell details (e.g. ω_{RS} and n_{RS}), the computational 2D and Q2D methods are found to be most promising. The reason for this is their comparably low complexity in combination with a generally good agreement with experimental data. More precisely, the models exhibited matching cell counts and a maximum difference in cell speed of about 10%. Furthermore, they were not reported to be constrained to particular use cases such as the analytical approaches.

3.1-3 In consideration of numerical and geometrical simplifications addi-

tionally introduced into the two-dimensional methods, such as e.g. reduced blade counts or loss correlations, the accuracy is assumed to increase even further by omitting these modifications.

3.1-4 As the 2D methods were solely validated against full-span stall, although resembling only a thin fraction of the annulus, the prediction of smaller disturbances like part-span stall might lead to even more accurate results.

3.1-5 The two-dimensional methodology for rotating stall predictions is hence the subject of further investigations in this work.

3.2-1 With respect to the impact of compressor features on the stall cell details, different studies were examined. In general, the compressor shaft speed Ω_S, the flow rate φ and the row staggers α and γ were the primary subject in various studies.

3.2-2 Different observations were reported in regards to feature impacts on the stall cell speed, count and size. Sensitivities towards parameter variations are hence not clearly identifiable.

3.2-3 The determination of effects is additionally aggravated by the fact, that stagger angle and shaft speed variations are usually accompanied by simultaneous changes in the flow coefficient. Identifying and assigning stall cell sensitivities to a particular parameter impact is therefore barely possible.

3.2-4 For this reason, the influences of the compressor shaft speed, flow rate and stagger angles will be studied in greater detail in this work.

Ref.	Test conditions	Parameter variations	Impact on ω_{RS}	Impact on n_{RS}	Impact on λ_{RS} or Θ_{RS}	Comments
Costilow and Huppert (1956) [44]	Single-stage / high-speed / EXP	α ↑	~ const.	~ const.	n/a	-
		φ ↓	↓	↓	n/a	-
Fabri and Siestrunck (1957) [39]	Single rotor / low-speed / EXP	φ ↓	~ const.	n/a	↑	
		γ ↑	~ const.	n/a	↓	Impact on λ_{RS} decreases with φ
Tanaka and Murata (1975) [40]	Single-stage / low-speed / EXP	φ ↓	↓ and ↑	↑ and ↓	↑	-
		r_h/r_t ↑	↓	↓	↑	Part-span RS becomes full-span RS
		L_x ↑	↑	↑	↑	Effect on ω_{RS} lessens for full-span RS
Choi et al. (2011) [46, 47]	Single-stage / high-speed / EXP & CFD	Ω_S ↑	↑	const.	~ const.	-
Day (2015) [13]	Single-stage / - / EXP	Ω_S ↑	~ const.	n/a	n/a	Lack of detailed information
		γ ↑	↑	n/a	n/a	
		L_x ↑	↑	n/a	n/a	
		Blading -	~ const.	n/a	n/a	
		Tip gap ↑	~ const.	n/a	n/a	
Hickman and Morris (2017) [41, 42]	Single-stage / high-speed / EXP	φ ↓	↓	const.	↑	-

⊠ Increases in row angles correspond to closed blades

Table 3.1: Literature review on rotating stall parameter studies with focus on single-stage builds

Ref.	Test conditions	Parameter variations	Impact on			Comments
			ω_{RS}	n_{RS}	λ_{RS} or Θ_{RS}	
Huppert et al. (1954) [48]	Multi-stage / high-speed / EXP	Ω_S ↑	↑	↑	n/a	-
Calvert et al. (1956) [45]	Multi-stage / high-speed / EXP	φ ↓	↓	unclear	n/a	-
Eastland (1982) [36]	Multi-stage / low-speed / EXP	φ ↓	↓	const.	↑	-
Gamache (1985) [37]	Multi-stage / low-speed / EXP	φ ↓	↓ and ↑	const.	↑	-
Lavrich (1988)[43]	Multi-stage / low-speed / EXP	φ ↓	↓ and ↑	varying	↑	-
Day (1976) [17], Day (1978) [15]	Multi-stage / low-speed / EXP	φ ↓ n_S ↑	↓ and ↑ ↑	const. ~ const.	↑ ↑	- Part-span RS becomes full-span RS
Dodds and Vahdati (2015) [49, 18], Dodds (2016) [50]	Multi-stage / high-speed / EXP & CFD	Ω_S ↑ α ↑	~ const. ↓ and ↑	unclear unclear	n/a n/a	When effect is decoupled from vane schedule ω_{RS}↓ : S1 hub stall / ω_{RS}↑: R1 tip stall

⊠ Increases in row angles correspond to closed blades

Table 3.2: Literature review on rotating stall parameter studies with focus on multi-stage builds

Chapter 4
Experimental method

Despite the increased liability of numerical methods, rig testing still plays an essential role in the design of gas turbines. To provide experimental verification of the numerical approaches used in this thesis, tests were performed on the high-speed rig at Technische Universität Darmstadt. The work has been part of the AG-Turbo COOREFLEX 1.2.5a project (FKZ 03ET7021P). Detailed information is given in Kunkel et al. (2019) [51] and Kunkel and Werner (2019) [52].
In the following sections, the overall rig specifications are described comprising a general overview of the test facility, the core module and the measurement equipment.

4.1 Rig overview

The basic setup of the compressor test rig is presented in Figure 4.1. The open loop cycle is fed with ambient air by the buildings air intake system. Guided by bends and a subsequent diffuser, the air enters the settling chamber (1) in which the flow is homogenized and the turbulence level reduced by a sieve. Passing by the mass flow measurement section (2), the air stream enters the compressor core module (3) followed by the exhaust collector box (4). The non-contact torque transducer (5) monitors the power input to the compressor which is driven by a 1.8 MW AC-Motor (8) including a planetary gearbox (6). Due to high rotational speeds up to 20000 rpm, a safety clutch (7) with membrane coupling connects motor and gearbox preventing severe damages in case of major component failures.

Total pressure ratio [-]	> 1.7	Mass flow rate [kg/s]	> 25
Max. shaft speed [rpm]	20000	Inlet diameter [mm]	< 500
Rotor tip speed [m/s]	> 400	Nominal power [MW]	1.8

Table 4.1: Compressor test rig parameters from Kunkel et al. (2019) [51]

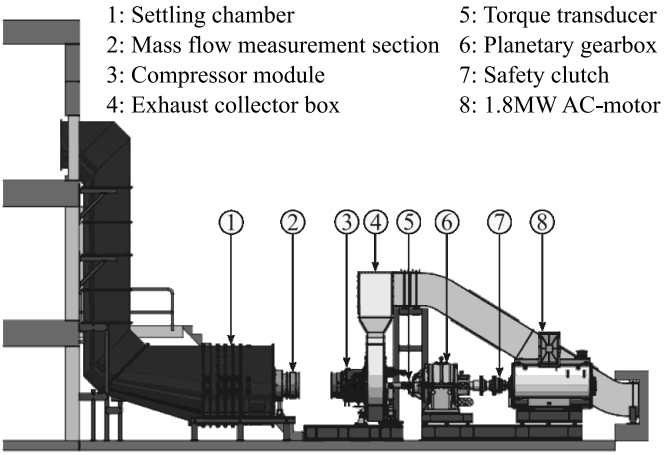

Figure 4.1: Sketch of the test facility for transonic compressor stages at Technische Universität Darmstadt based on Kunkel et al. (2019) [51]

4.2 Compressor module

The compressor module is the core of the test rig as shown in Figure 4.1 at station (3). It is a scaled one-and-a-half stage representative of a gas turbine compressor front stage, designed by Siemens AG. Rows of variable inlet guide vanes (VIGV) and stator vanes (VSV) enclose the three-dimensionally optimized rotor geometry. To ensure the Mach number similarity, scaling was based on realisable rotational speeds. The modular design in combination with a cantilevered rotor position allows short turnaround times between geometry changes.
Operating conditions of the compressor are altered using a ring throttle located subsequent to the radial diffuser. The throttle valve features two concentric rings with a set of slots. By rotating the outer ring, the slots can be closed or opened depending on their relative position. With this changing the area at the compressor outlet, the mass flow rate and hence the operating point can be controlled. Closing is done using pneumatic cylinders pushing against a spring preload. In case of unfavourable operating conditions, e.g. during rotating stall, the compressor can quickly be dethrottled by releasing pressure from the cylinders and opening the slots.

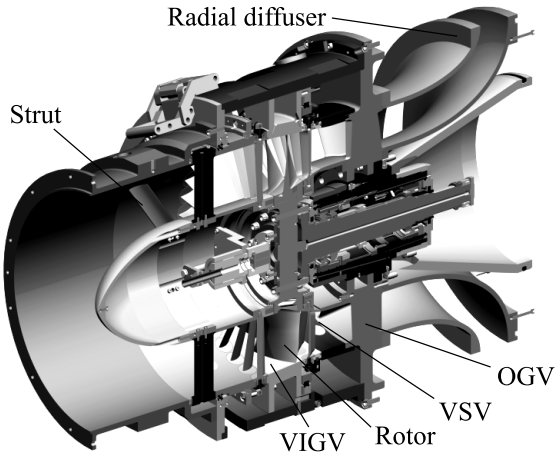

Figure 4.2: Sectional view of the compressor core module from Kunkel and Werner (2019) [52]

4.3 Instrumentation

Both, the core module and the rig are extensively equipped with steady and unsteady instrumentation to monitor and analyse the compressor performance. In total 169 pressure and 64 thermocouple channels for steady measurements are available. Additionally, up to 48 piezoresistive pressure transducers can be recorded simultaneously. Figure 4.3 provides an overview of the different rig measurement sections which are subsequently described in more detail.
In plane A of the settling chamber, two rakes with combined kielheads are aligned in vertical and horizontal direction measuring both total pressure and total temperature. Along with the data acquired by the subsequent inlet rake in plane B, mass flow measurements are conducted using a differential pressure approach. As the rake is traversable by 360 degree, it is also used to check the homogeneity of the incoming flow which was found to be sufficient. Boundary layer profiles and total quantities are acquired using a corresponding rake in front of the struts in plane Strut_{in}.
The rotor exit flow is assessed by stator leading edge instrumentation (VSV_{in}) located at two different vanes. Each of them contains five probes along the channel height for total pressure and total temperature measurements. Additional data of higher resolution can be obtained using

traversable five hole probes. Using an axial array of 23 piezoresistive pressure transducers mounted to the rotor casing, the unsteady wall pressures are measured with a sampling frequency of 500 kHz. The data is primarily used for flow field visualization by means of pseudo-spatial contours. Further transducers were placed around the annulus to capture the circumferential movement of emerging flow disturbances.
The total quantities at the stage exit are measured in between VSV and OGV. The corresponding plane is denoted as OGV_{in}. Two circumferentially distributed rakes as well as a rake of five-hole probes are utilized in this section.

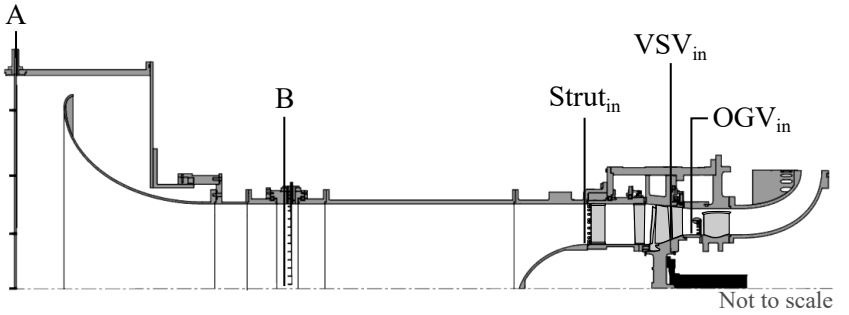

Figure 4.3: Sectional view of the compressor test rig indicating the different measurement planes based on Kunkel et al. (2019) [51]

Chapter 5
Computational method

Compressor stall computations are generally associated with higher modelling requirements due to unsteadiness and the involvement of multiple blade passages. The prediction of compressor stall is hence considered as one of the most challenging task to which computational fluid dynamics is applied (see Denton (2010) [53]).
The following chapter focuses on different methodologies applied in the context of stall computations and evaluation methods. It describes the approach used in this work and (where possible) takes a closer look at those reported in the literature. Based on the information listed in Table 5.1, the decisions made for the applied methodology will be elaborated underlining the increased demands upon the numerical procedure for stall computations. The chapter hence deals with the research questions specified below:

RQ 5.1 *Which modelling approaches and numerical strategies have to be considered for feasible yet accurate stall computations?*

RQ 5.2 *Which analysis techniques are most suitable for rotating stall evaluations?*

Authors	Compressor build	Turbulence model	Time steps		Exit condition	Trigger	Mesh resolution		Difference to EXP		Comments
			Per rev.	Per pitch			Passage	Total	Cell count	Cell speed	
Vahdati et al. (2008) [54]	Multi-stage (H-FA)	Spalart-Allmaras	n/a	n/a	Nozzle	Mistuning (−0.5°)	n/a	60 x 10^6	±1	n/a	-
Gourdain et al. (2010) [55]	Single-stage (FA)	Spalart-Allmaras	10000	≈ 333	Quadratic law	None	500 x 10^3	31 x 10^6	+2	+15.0%	-
Choi and Vahdati (2011) [56]	Single-stage (FA and H-FA)	n/a	n/a	n/a	Conv. nozzle	Mistuning (−0.5°)	n/a	n/a	n/a	n/a	Cell speed in H-FA case differed by ca. -52% from all FA cases + No impact of mistuning on solution
Choi et al. (2011) [46]	Single-stage (FA)	n/a	n/a	n/a	Conv. nozzle	Mistuning	n/a	24 x 10^6	n/a	n/a	-
Choi et al. (2012) [47]	Single-stage (FA)	n/a	1200	≈ 45	Conv. nozzle	Mistuning (−0.5°)	n/a	20 x 10^6	0 0	+6.2% +1.3%	Case 1: 60% design speed Case 2: 95% design speed
Li and Sayma (2012) [57], Li (2013) [58]	Single-stage (FA)	Spalart-Allmaras	1350	≈ 37.5	Conv. nozzle	Mistuning (−0.2°) + damaging	165 x 10^3	10 x 10^6	n/a	n/a	Cell count differed in case with damaged blade by +5 from reference
Dodds and Vahdati (2014) [18], Dodds (2016) [50]	Multi-stage (H-FA)	Spalart-Allmaras	1200	≈ 35	Conv. nozzle	None	300 x 10^3	70 x 10^6	0 -3	-15% +5%	Case D: Stator hub stall Case G: Rotor tip stall
Lee et al. (2018) [59]	Single-stage (FA)	Spalart-Allmaras	n/a	n/a	Conv. nozzle	None	300 x 10^3	13 x 10^6	0	max. +3.1%	-
Kim et al. (2019) [60]	Single-stage (FA)	Spalart-Allmaras	n/a	160	Conv. nozzle	Mistuning (−0.2°)	n/a	100 x 10^6	0 0	+7% +4%	Case 1: Full-span stall Case 2: Part-span stall

⊠ FA = Full-Annulus / H-FA = Hybrid Full-Annulus

Table 5.1: Literature review on rotating stall computations applying high-fidelity CFD

5.1 Flow solver TRACE

All CFD calculations mentioned in the present work were performed using the numerical flow solver TRACE version 9.1. It is developed by German Aerospace Center (DLR) and especially designed for problems in turbomachinery. Based on the cell-centered finite-volume-method, TRACE solves the compressible Reynolds-averaged Navier-Stokes equations in a rotating frame of reference. The inviscid fluxes at the cell interfaces are calculated from Roe's flux-difference splitting method together with an upwind approximation. Additionally, a MUSCL-scheme and a van Albada-Limiter are utilized. All calculations are second-order accurate in space and time by means of the implicit backward Euler scheme. Time marching is carried out by a dual time stepping technique. Further details on the code can be found in Ashcroft et al. (2010) [61], Becker et al. (2010) [62] or the official user guide [63].

5.2 Solver properties

In all computations the fluid was treated as ideal gas. Solid surfaces were assumed adiabatic and smooth applying wall functions where necessary. Due to the implicit behaviour of TRACE, high Courant–Friedrichs–Lewy (CFL) numbers are possible without affecting the numerical stability. Typically a value of 100 was used allowing fast convergence.
As presented in Table 5.1, in most stall computations turbulent viscosity is approximated using the Spalart-Allmaras one-equation model (see Spalart and Allmaras (1992) [64]) in a standard or modified form. In this thesis, the suitability of the k-ω SST two-equation model by Menter (2003) [65] was investigated additionally.
Time scales in the unsteady computations are usually based on the number of steps and sub-iterations per blade passing. The minimally required time steps size for accurate results usually depends on different factors. These are for example the time scales of the phenomenon to be studied or the spatial grid resolution. Finding an appropriate amount of steps is hence cumbersome and requires extensive sensitivity studies. Considering Table 5.1, the values can vary between 35 and 333. However, comparing the details from Choi et al. (2012) [47] and Gourdain et al. (2010) [55], more time steps per pitch do not necessarily lead to more accurate results. For this reason, the number of time steps per blade passing was set to 30 with

20 inner loops.

5.3 Convergence criteria

Convergence of the steady-sate RANS computations was considered to be reached as the maximum residuals fell below 10^{-3} with the mass flow rate and pressure fluctuations in each row reducing to 0.1% over the last 1000 iterations.
For the unsteady URANS computations the default convergence criteria are impractical due to oscillations caused by instabilities. Therefore, an additional premise was introduced taking the dominant harmonics into account. This was done by analysing the pressure and velocity traces captured by numerical probes. By applying a sliding discrete Fourier transformation (see section 5.7.1), the evolution of the signal and hence of any disturbance can be assessed. Convergence was assumed in case the first three harmonics remained constant for at least 10 revolutions. This equals about five flow-through times from domain inlet to exit.

5.4 Nozzle exit boundary condition

It is usual to predefine the static pressure at the compressor exit. At stalled conditions, however, the flow becomes non-uniform and unsteady. Therefore, applying a time-invariant static exit pressure is inappropriate. An alternative method is represented by a variable-area nozzle added to the domain exit. The approach was first reported by Vahdati *et al.* (2004) [66] and is hence commonly applied in the context of stall computations (see Ref. [47, 18, 67, 68]). The major advantage of this approach is its reliability and accuracy. By using the alternative method, the pressure behind the compressor becomes flexible and adjusts automatically, while the nozzle outlet pressure p_{ex} is fixed. In case of the nozzle being choked, the flow becomes independent of the outlet conditions. For an ideal gas, the mass flow rate is mainly determined by the total pressure $p_{t,in}$ and total temperature $T_{t,in}$ at the nozzle entry plane and the throat area A^* (Eq. (5.1), Bräunling (2001) [19]).

$$\dot{m} = \frac{A^* \cdot p_{t,in}}{\sqrt{T_{t,in}}} \sqrt{\frac{\kappa}{R}} \left(\frac{2}{\kappa + 1} \right)^{\frac{\kappa+1}{2(\kappa-1)}} \tag{5.1}$$

The concept usually applies a simple convergent nozzle with the throat

area matching the domain outlet (see Table 5.1). In the current work, the numerical stability was observed to decrease when the exit Mach number was large at choked conditions. For this reason, the approach was modified using a convergent-divergent nozzle as shown in Figure 5.1. The basic idea is to enforce a shock in the divergent section leading to a flow deceleration and exit Mach numbers below unity. In order to obtain such conditions, the back pressure has to be sufficiently high to provoke the shock, but still small enough to maintain a choked nozzle.

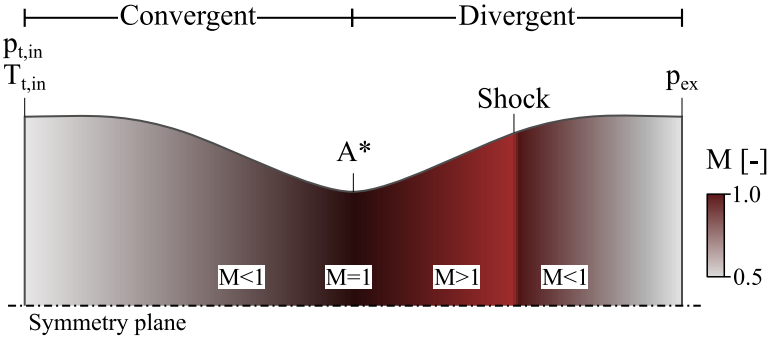

Figure 5.1: Schematic of a convergent-divergent nozzle

5.5 Geometry considerations

Computations on the steady branch of a constant speed characteristic are generally performed using single-passage RANS models. Especially close to the design point, the calculations have proven to be reliable. Near the peak of a speed line, the models usually fail due to the growth of large separations. The computations do either not converge or stop because of recirculations reaching the mixing interfaces. The failure is then referred to as numerical stall. For an accurate prediction of the stalling behaviour, however, the single-passage approach is not suitable. In the following, some aspect regarding the computational domain in the context of unsteady stall computations will be discussed.

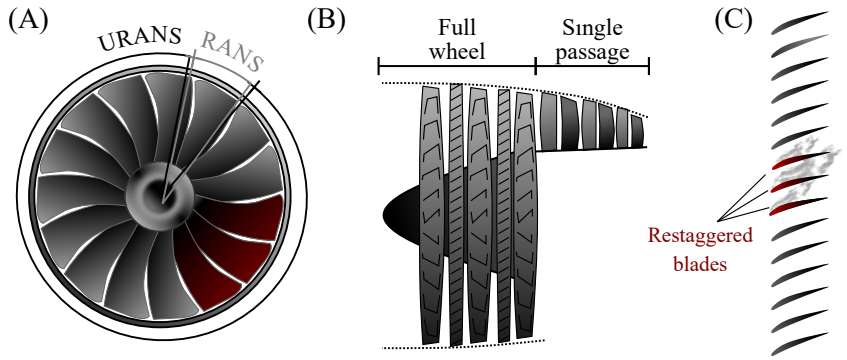

Figure 5.2: Schematic of different geometrical features used in the context of rotating stall computations

5.5.1 Circumferential extent

As compressor stall is usually initiated by disturbances propagating around the annulus, a sufficient number of passages has to be modelled. For spike-type stall inception, this was shown by Pullan et al. (2015) [12]. By comparing the results of a single-passage and a quarter-annulus domain, they observed the latter to stall at higher mass flow rates. The early formation of spikes was hence concluded to require multiple passages. For disturbances on a larger scale, such as rotating stall, Crevel at al. (2014) [69] compared computations applying one eighth of the annulus to experimental data. The results showed, that the CFD could neither match the odd number of stall cells nor their propagation speed due to the forced periodicity. Hence, in this work full-wheel domains were applied for computations near and beyond the stability limit as shown in Figure 5.2-A.

5.5.2 Axial extent

Crevel at al. (2014) [69] examined the impact of upstream and downstream volumes on the stalling pattern. Therefore, two different models were investigated. The first configuration solely included the core compressor, whereas the other one contained the whole test rig. While the propagation speed marginally increased by about 2%, the number of stall cells fell from 24 to 16 as the rig volumes were taken into account. For

this reason, parts of the upstream and downstream ducting were taken into account in this thesis. Due to computational costs, however, the complete rig geometry could not be considered.

5.5.3 Hybrid models

On one hand, the studies mentioned above emphasize the necessity of full-wheel models including supporting structures like struts or the ducting for accurate results. The accompanying computational costs, however, can rise tremendously. A compromise is represented by hybrid models applied in References [54, 56, 18, 50]. The idea is to model parts of the compressor in a full-wheel fashion for URANS computations. For the downstream rows, in turn, a single-passage steady-state approach is applied. An exemplary sketch is illustrated in Figure 5.2-B. The advantages of this method are the integration of large volumes at manageable costs. Additionally, downstream domain and hence row interactions are modelled automatically. The downside of using a hybrid model is that it is only reasonable if the location of the stalling blade row is known. Furthermore, Choi and Vahdati (2011) [56] compared results of a hybrid approach to data from a conventional full-wheel model. The study revealed a discrepancy in cell speed by -69.7%. As a consequence, the hybrid approach was not considered in this work.

5.5.4 Mistuning

Another important aspect is the initiation of stall at an early stage. For a perfectly symmetric full-wheel geometry, the development of inhomogeneities from locally high incidences can take several revolutions. In order to reduce the computational time, Vahdati et al. (2008) [54] introduced an aerodynamic mistuning by changing the stagger angle of a few adjacent rotor blades. As the flow is impaired by the restaggered blades, the compressor begins to stall as depicted in Figure 5.2-C. The procedure was since used in various computational studies (see Ref. [12, 56, 46, 47]). The introduced mistuning usually varies between -0.2° and -0.5° as shown in Table 5.1. In general, small stagger changes do not affect the converged solution. Larger deviations, in turn, can lead to discrepancies in the stalling pattern. This was shown by Li and Sayma (2012) [57] who compared a case with a partly restaggered rotor to computations including

a damaged blade. The latter led to six stall cells, whereas the reference case was observed to exhibit single-cell rotating stall. In this work, three adjacent rotor blades were restaggered by -1° opening the passage.

5.6 Speedline process

Knowledge about the overall performance curve is crucial when focusing on compressor stall. Based upon the slope, characteristics like the stability limit or the inception type can be derived. The process applied to compute a performance curve is illustrated in Figure 5.3.

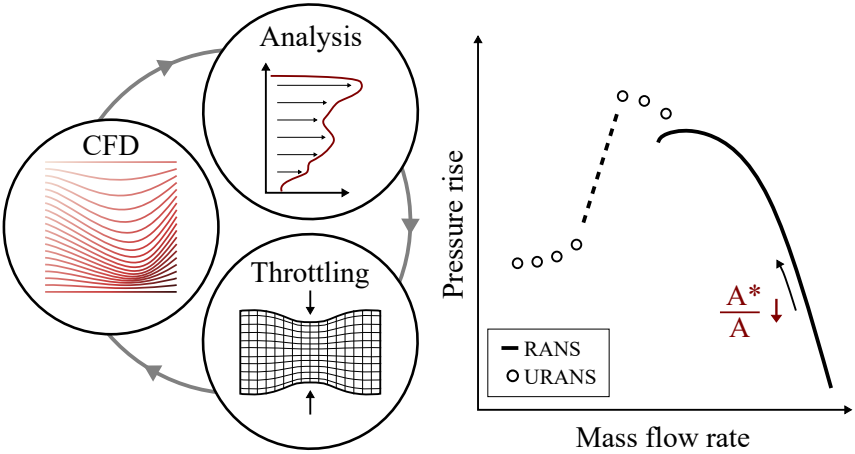

Figure 5.3: Procedure for the computation of a compressor performance curve

In general, the curve is obtained by calculating multiple operating points at different mass flow rates. Each computation is divided into three steps. In the first part, a CFD is conducted at given boundary conditions. Subsequently, the converged solution is analysed to derive all relevant flow parameters. Afterwards, the compressor is throttled by reducing the nozzle area ratio A^*/A (see section 5.4). Thus, the following CFD computes an operating point at smaller mass flow rates. During the last step, the static exit pressure is adapted to the area ratio and the total pressure at the nozzle entry plane. This ensures the nozzle to be choked with a perpendicular shock within the diverging section.
The steady branch of the performance curve is computed using single-

passage RANS CFD. The procedure starts with an operating point at high mass flow rates near compressor choke conditions. The procedure stops as the stability limit is reached. Subsequently, the model is adjusted using the steps described in section 5.5. The resulting full-wheel URANS CFD starts at the last stable operating point obtained from the single-passage RANS computations and is throttled into compressor stall incrementally.

5.7 Signal analysis techniques

For the evaluation of the unsteady compressor flow field, both numerical and experimental signal traces were analysed. By using different techniques, the data captured by probes then allowed for the determination of the rotating stall properties. In the following, the methodologies applied to derive the characteristic quantities are presented and discussed.

5.7.1 Frequency spectra

The frequency spectra of each signal were obtained by applying the Discrete Fourier Transform (DFT) with the efficient Fast Fourier Transform (FFT) algorithm described by Cooley and Tukey [70]. The DFT is the equivalent of the continuous Fourier Transform for signals of a finite number of samples and yields a corresponding complex-valued function of frequencies f.

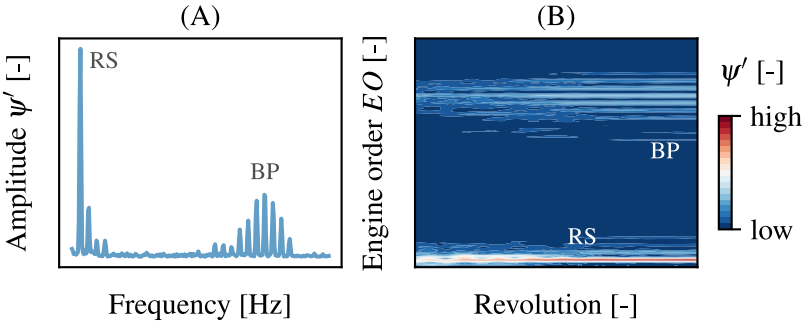

Figure 5.4: Exemplary frequency spectrum (A) and spectrogram (B) showing the occurrence of rotating stall

An exemplary frequency spectrum is depicted in Figure 5.4-A exhibiting significant peaks at high and low frequencies. In this case, both peaks are assigned to the blade passing (BP) period and a propagating rotating stall. In order to evaluate the occurring frequencies over time, a sliding DFT was used. The approach applies a DFT over a fixed sample interval continuously moving along a signal stream. As a result, a frequency spectrogram is generated as illustrated in Figure 5.4-B. The engine order (EO) on the ordinate is commonly applied to obtain a non-dimensional quantity defined by Equation 5.2.

$$EO = \frac{f}{\Omega_S} \tag{5.2}$$

Due to shortcomings of the DFT some additional features were implemented. These for instance concern reduced resolutions of the frequency spectrum resulting from small sample sizes. The effect is depicted in Figure 5.5-A. To circumvent this loss in accuracy, a parabolic interpolation was applied as proposed by Gasior and Gonzalez (2004) [71].

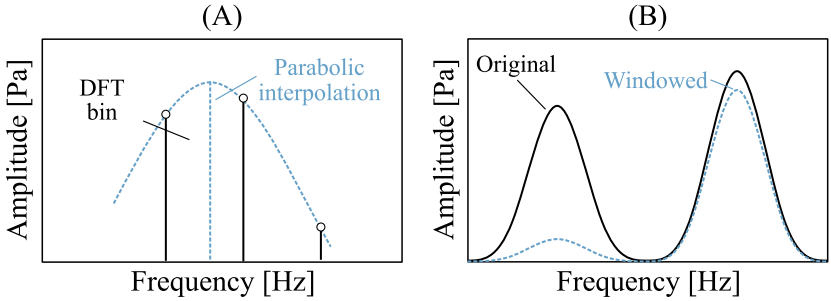

Figure 5.5: Exemplary parabolic interpolation (A) and frequency spectrum of a signal superimposed by a window function (B)

A second disadvantage of the DFT is associated with data set lengths not corresponding to an exact signal period. In this case, the energy of single bins is often experienced to spread as shown in Figure 5.5-B. The so-called spectral leakage can be reduced by superimposing the original signal with a window function. The purpose is to attenuate the samples in proximity to the boundaries and fit adjacent periods smoothly. The effect was also studied in Gasior and Gonzalez (2004) [71] using different functions. Based on the results, the Blackman window was selected in this work (see Blackman and Tukey (1958) [72]).

5.7.2 Circumferential speeds

The cross-correlation function offers a way to determine the propagation speed of any arising disturbance in circumferential direction. Therefore, two probes with a slight angular offset $\Delta\theta$ are required. Using the corresponding time-dependent signals x(t) and y(t), the correlation function can be calculated via Eq. 5.3 (see Bendat and Piersol (2010) [73]). Therein, T and R_{xy} represent the measurement period and the correlation coefficient. When both signals x(t) and y(t) are almost identical and only shifted in time, the maximum of the cross-correlation function is located at the time-shift Δt.

$$R_{xy}(\Delta t) = \frac{1}{T} \int_{-T/2}^{T/2} x(t) \cdot y(t + \Delta t) \cdot dt \tag{5.3}$$

Using both, the angular offset $\Delta\theta$ and difference in time Δt required by the perturbation to travel circumferentially, the individual cell speed ω_{RS} can be calculated.

5.7.3 Circumferential modes

In order to determine the number of disturbances travelling around the annulus, two different approaches were applied.

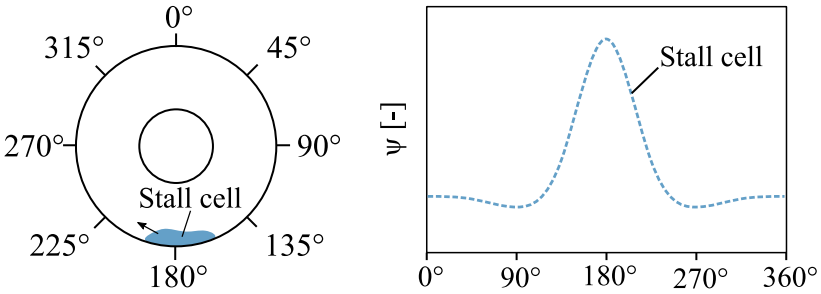

Figure 5.6: Representation of circumferential modes captured by multiple probes

The first method was proposed by Dodds and Vahdati (2015) [49] and evaluates the engine orders in the rotating EO_{rot} and stationary EO_{stat} frame of reference. The number of stall cells n_{RS} for example is then

calculated using Equation 5.4.

$$n_{RS} = EO_{RS,rot} + EO_{RS,stat} \tag{5.4}$$

The second approach was suggested by McDougall et al. (1990) [9] in which the velocity or pressure traces were captured at multiple locations around the annulus. The signals were then combined at each instance in time to obtain a circumferential distribution as depicted in Figure 5.6. Subsequently, the dominant circumferential harmonics were obtained by using a Fourier analysis.

5.8 Conclusions

In this chapter the general computational method was presented and discussed. Based on approaches reported in the available literature, decisions regarding the numerical setup were made. With respect to the initial research questions defined at the beginning, the following conclusions can be drawn:

5.1-1 The Spalart-Allmaras model was found to be the main turbulence model applied to rotating stall computations in other works. For this reason, the Spalart-Allmaras and the Wilcox k-ω-SST model were subsequently investigated.

5.1-2 As 35 time steps per pitch were seen to be sufficient for accurate stall predictions, the amount of time steps for the unsteady computations was set to 30 with 20 inner loops.

5.1-3 To enable a time-variant static exit pressure at the domain outlet, a variable-area nozzle was added. In contrast to the commonly used convergent geometry, a convergent-divergent nozzle was applied to increase the numerical stability.

5.1-4 Regarding the computational domain a full-wheel model was applied in order to avoid inaccuracies associated with forced periodicities. As the axial extent was concluded to affect the stall cell number, parts of the upstream and downstream ducting were taken into account. To accelerate the development of inhomogeneities, three adjacent rotor blades were restaggered and opened by 1 degree initiating the stalling process at an early stage.

5.2-1 The rotating stall frequency Ω_{RS} was derived using the DFT and the sliding DFT enhanced by a parabolic interpolation and the application of a Blackman window function.

5.2-2 The stall cell speed ω_{RS} was determined by applying the cross-correlation function to signal traces captured by two probes located at different circumferential positions.

5.2-3 The number of stall cells was calculated from the engine orders in the stationary and rotating frame of reference. Additionally, the Fourier analysis of the circumferential pressure distribution was applied to obtain the spatial harmonics.

Chapter 6
High-fidelity computations

In this chapter a three-dimensional high-fidelity model of the TU Darmstadt high-speed compressor and the respective simulation results obtained are presented and discussed. The main objective is the generation of a numerical reference which the low-fidelity method will be compared to in detail in Chapter 7.
Plausibility and accuracy of the computational results is validated using experimental findings. To the authors knowledge, this is the first time the capabilities of the flow solver TRACE are so widely verified in terms of compressor stall simulations. As the results allow for an enhanced interpretation of the measured findings, additional light is shed on the aerodynamic phenomena involved at near stall and stalled compressor operation. In general, the following research questions are of interest and will be answered in this chapter:

RQ 6.1 *To what degree is the flow solver TRACE capable to predict compressor stall?*

RQ 6.2 *What insights can be derived from the computations regarding the stall mechanisms?*

6.1 Steady simulations

The steady-state compressor performance is predicted using single-passage RANS computations. Information on both the numerical setup and domain is presented subsequently. Additionally, considerations regarding different post-processing approaches are discussed. Eventually, the computational results are validated against experimental data.

6.1.1 Domain and boundary conditions

The numerical model used for the steady-state computations is illustrated in Figure 6.1. Besides the compressor core module, the intake section as well as supporting structures like strut and outlet guide vanes are included.

Due to the different blade counts, the single-passage model contained mixing interfaces in between all rows.
The inlet boundary condition was defined as uniform preserving the total conditions in the test facility. More detail is provided in Table 6.1. Both, the values for the turbulent intensity and length scale were estimated due to a lack of hot wire measurements.

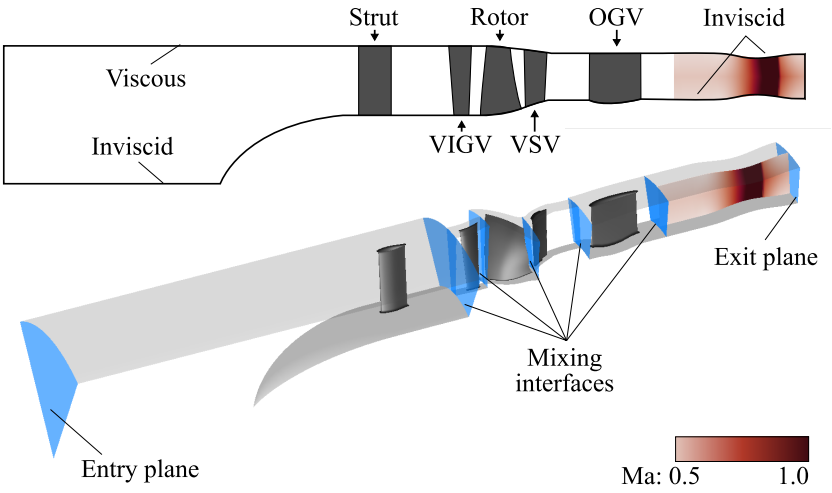

Figure 6.1: Schematic view of the computational single-passage model

At the exit, a fully meshed convergent-divergent nozzle was added. With the nozzle being choked, the compressor operating conditions were altered by adjusting the throat area. As described in section 5.4, the performance hence was independent of the static exit pressure defined at the domain outlet. Solid walls in the nozzle block were modelled as inviscid.

Total pressure [Pa]	101325.0	Turbulent intensity [%]	1.0
Total temperature [K]	288.15	Turbulent length scale [m]	0.001

Table 6.1: Inlet boundary conditions

6.1.2 Computational grid

In order to ensure independence of the numerical results from the spatial grid resolution, four different meshes were investigated. The number of grid cells ranged from 1.5 to 6.5 $\cdot 10^6$. Simulations were performed resolving a complete constant speed characteristic. The level of uncertainty is assessed by the percentage error ϵ relative to the measured data.

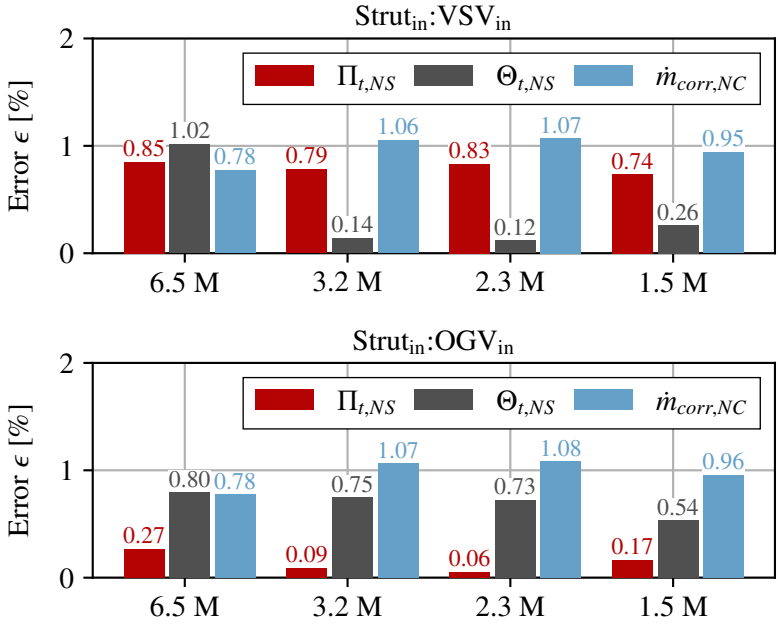

Figure 6.2: Error ϵ relative to measured data obtained from different meshes applied for the computation of a constant speed characteristic

Figure 6.2 depicts the relative discrepancies for two different control volumes. One ranging from strut to VSV (top) and the other one from strut to OGV (bottom). Usually mesh studies are performed to investigate the grid independence in the aerodynamic design point. In this work a more comprising evaluation was pursued by focusing on three distinctive quantities at the near stall (NS) and near choke (NC) conditions. These are the total pressure ratio $\Pi_{t,NS}$, the total temperature ratio $\Theta_{t,NS}$ and the corrected

mass flow rate $\dot{m}_{corr,NC}$.
In general, the maximum deviation of the numerical results from the measured data is close to 1% and hence considered small. Regarding the impact of the spatial resolution on the accuracy no clear trend can be noticed. In other words, the application of the highly resolved mesh with about $6.5 \cdot 10^6$ cells does not result in substantial improvements compared to the more feasible grids. For all subsequent investigations the mesh comprising $3.2 \cdot 10^6$ cells was chosen, although a less sophisticated resolution might have been suitable as well.

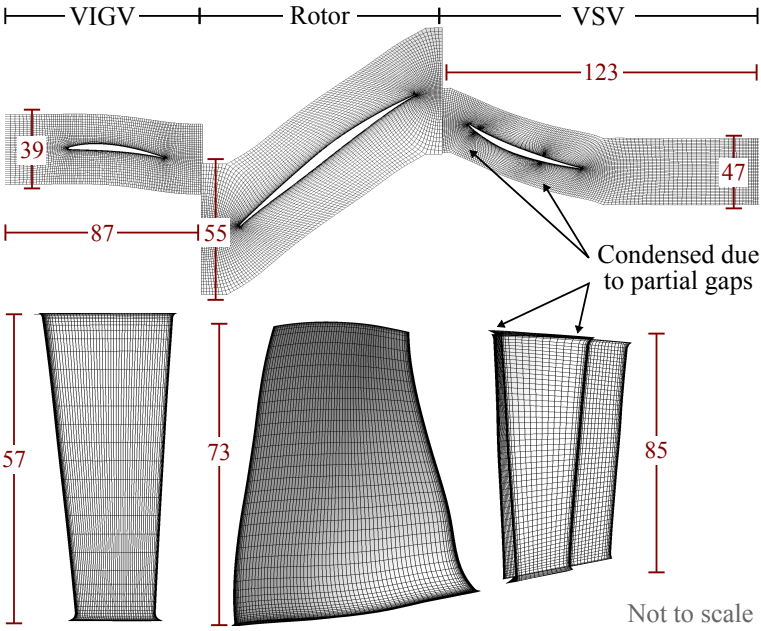

Figure 6.3: Mesh resolution in the core compressor module with $3.2 \cdot 10^6$ cells

The grid within the core compressor rows is illustrated in Figure 6.3. Indicated by the red numbers is the amount of cells in each direction. The structured grid had about 250 to $500 \cdot 10^3$ cells per passage which is in accordance to the resolutions used in other works reviewed in Table 5.1. Blade features like fillets, rotor tip gap and stator partial gaps were included. With a non-dimensional wall coordinate of $y+ \leq 1$ in close prox-

imity to solid walls, boundary layers were sufficiently resolved.

6.1.3 Post-processing considerations

The standard post-processing of numerical data usually differs from experimental approaches. In CFD quantities are calculated in every cell while measurements are performed at distinct locations within the flow field using probes and sensors. When deriving the characteristic compressor parameters by building the circumferential and radial area-averages, discrepancies can result from different resolutions.

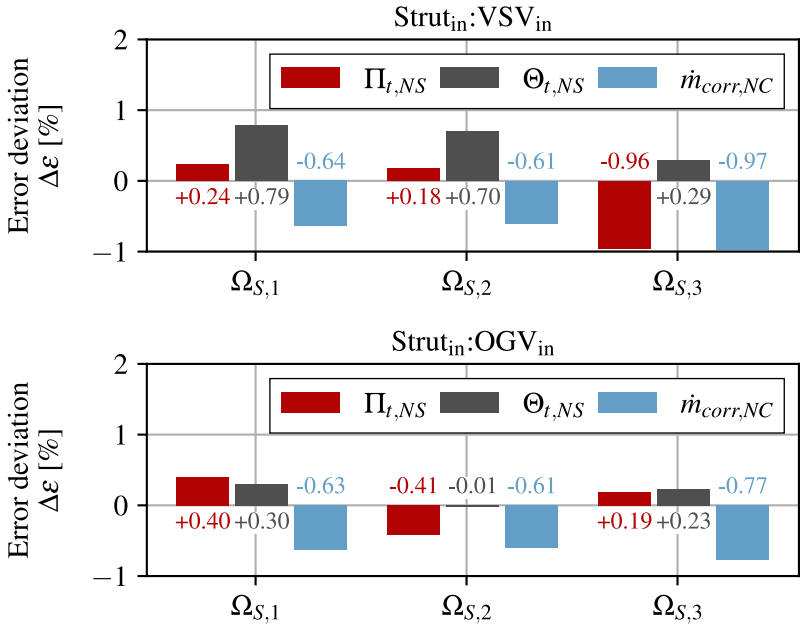

Figure 6.4: Differences in the data of the standard and modified post-processing approaches relative to the measured data

In order to assess the discrepancies between numerical and experimental findings due to post-processing differences, an adapted approach was developed. The routine evaluates the compressor parameters at those locations predefined by the rig instrumentation. More information on the approach can be found in Gnanasampanthan (2019) [74].

Figure 6.4 illustrates the error deviation $\Delta\epsilon$. The parameter represents the differences in the data of the standard and modified post-processings relative to the measured values. In order to obtain the total relative discrepancy to the experimental data, $\Delta\epsilon$ has to be added to the errors ϵ defined in the previous section. Again, two control volumes were taken into account. Additionally, the impact was studied for three different compressor shaft speeds with $\Omega_{S,1} > \Omega_{S,2} > \Omega_{S,3}$.
Overall, the deviations associated with the modified post-processing are below 1% and therefore rated small. An explicit tendency of the additional error $\Delta\epsilon$ towards smaller shaft speeds Ω_S is not identifiable. Due to the rather marginal discrepancies, the standard post-processing was kept for all data presented hereinafter. The decision was also made, since the domain for the unsteady computations did not include the strut geometry. An experimentally-based post-processing was hence not applied.

6.1.4 Compressor performance

In the following, the compressor performance is presented and discussed by means of calculated and measured characteristics. In addition, the suitability of different turbulence models for the given compressor test case is investigated.
Figure 6.5 illustrates the total-to-total pressure and temperature rise characteristics for $\Omega_{S,1}$. Due to confidentiality, the abscissa is set in relation to the corrected mass flow rate at choked conditions $\dot{m}_{corr,NC}$. The ordinate, in turn, is divided by the total pressure ratio $\Pi_{t,NS}$ and the total temperature ratio $\Theta_{t,NS}$ near compressor stall. Also included are error bars of 1% relative to the measured data. The studied turbulence models are the two-equation models by Menter (2003) [65] and Wilcox (1988) [75] as well as the single-equation approach by Spalart and Allmaras (1992) [64]. They are denoted as k-ω-SST, k-ω and SA, respectively.
Clearly visible for all computed speedlines is the good agreement with the experimental data. For almost all measured operating points, the discrepancies are close to the indicated error of 1%. With respect to the SA-model, the best alignment with the experimental slope can be observed. However, the turbulence model fails to yield the operating points near the measured stability limit due to a prediction of the stall onset at 7.1% higher mass flow rates. Both two-equation models, in contrast, are able to capture the whole operating range. The corresponding speed lines are

nearly identical with negligible differences. Regarding the stalling point, the models underpredict the onset by about 2.2% in corrected mass flow rate.

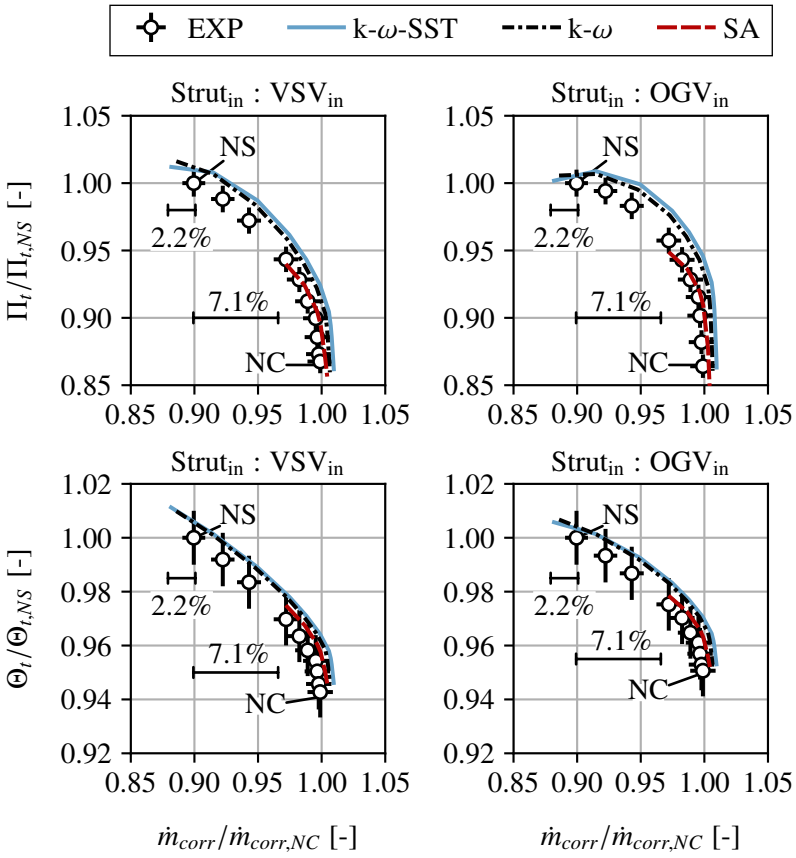

Figure 6.5: Measured and computed total-to-total pressure and temperature rise characteristics for $\Omega_{S,1}$

The radial total-to-total pressure and temperature ratio profiles behind the rotor and VSV are depicted in Figure 6.6. Presented are both conditions, near choke and near stall. For the latter, the SA model is not included as it failed to resolve the corresponding operating point.
Similar to the performance curves, agreement with the experimental re-

sults is sufficiently good. The CFD captures the radial diversion of both quantities towards the casing with decreasing mass flow rate accurately. The higher loading in the rotor tip area at near stall conditions also indicates in which region compressor stall is initiated. The design can hence be considered as tip critical.

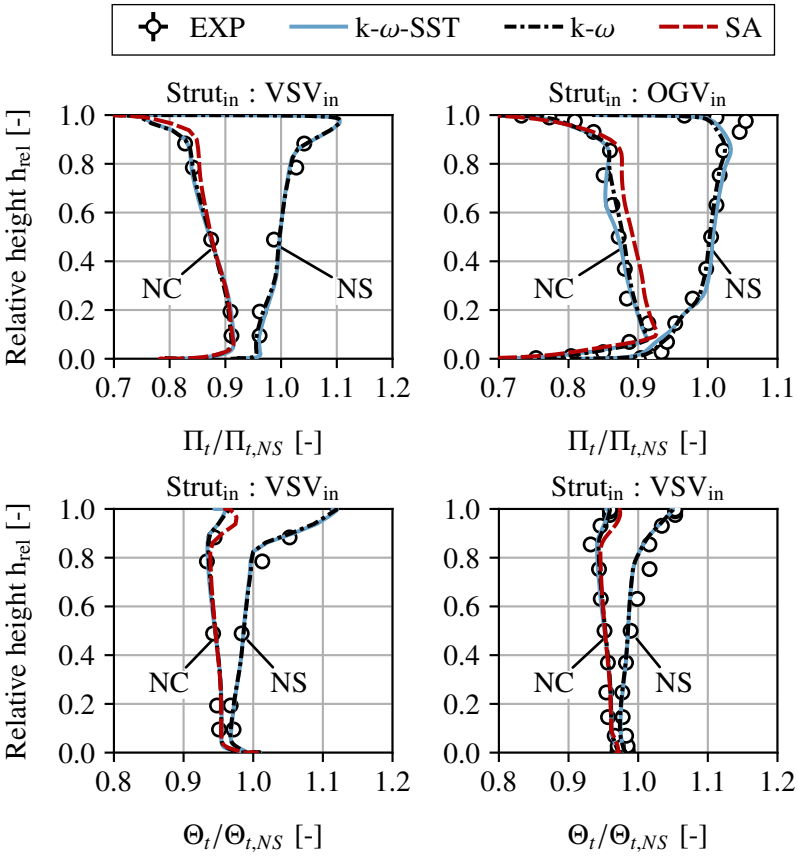

Figure 6.6: Measured and computed total-to-total pressure and temperature profiles for $\Omega_{S,1}$ at near choke (NC) and near stall (NS) conditions

With respect to the capabilities of the investigated turbulence models, the differences between the two-equation approaches is considered negligible.

Therefore, the k-ω model is not be utilized hereinafter.

6.2 Unsteady simulations

In order to resolve any form of instability arising in proximity to the stability limit and beyond, URANS computations are performed. The applied numerical model differed from the RANS setup previously presented. The adapted domain and boundary conditions are hence described in the following. After assessing the overall compressor performance in stall, both the inception mechanism and rotating stall type are evaluated in greater detail.

6.2.1 Domain and boundary conditions

The numerical model used for the unsteady computations is illustrated in Figure 6.7. Besides applying a full-wheel domain, the nose cone along with the strut were excluded to reduce computational costs and time. To avoid unphysical coupling with the inlet plane, an inviscid duct was added upstream to the VIGV. The flow conditions behind the strut were extracted at the previous interface plane and applied as new entry boundary condition. The OGV was kept since the vane count ratio between VSV and OGV was an integer number. In case of any resulting interferences, the model was hence able to capture them. In order to initiate stall at an early stage, three adjacent rotor blades were restaggered by 1 degree as described in section 5.5. The entire setup contained around $70 \cdot 10^6$ cells, leading to a runtime of 8 hours per revolution on 240 CPU with 30 time steps per blade passing period.
For the evaluation of the unsteady compressor flow field, as described in section 5.7, numerical probes were placed around the annulus in each row. Depending on the location, blade or vane, signals were captured in either the rotating or stationary frame of reference. The probes were placed close to the leading edges with the total number depending on the blade count. Consequently, the blade-to-probe ratio in the rotor and stator domains was one and two, respectively.

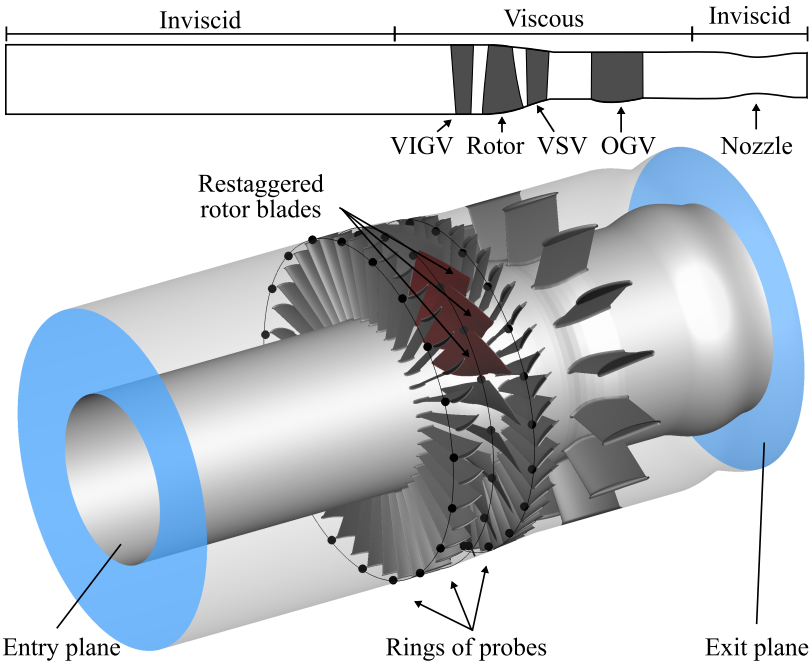

Figure 6.7: Numerical full-wheel model applied for the unsteady computations

6.2.2 Compressor performance

For a global view on the conditions in proximity to the stability limit and beyond, the computed compressor performances are discussed.
As usually applied in the context of compressor stall, the total-to-static pressure rise ψ is plotted against the flow coefficient φ in Figure 6.8. For an easier validation of the stalling point, the abscissa as well as the ordinate are set into relation with the near stall conditions. With respect to the turbulence modelling, the k-ω-SST as well as the Spalart-Allmaras approaches were applied. Due to the negligible differences between the two-equation methods, the Wilcox k-ω model was not considered.
With the strut geometry being left out in the adapted setup, the data could not be compared to the experimental data used before. Hence plausibility and accuracy of the modified models are verified on the basis of the previously validated RANS computations. Since no significant discrepancies

are apparent in the steady performances, the adapted setup is concluded to be without additional inaccuracies due to the modifications.

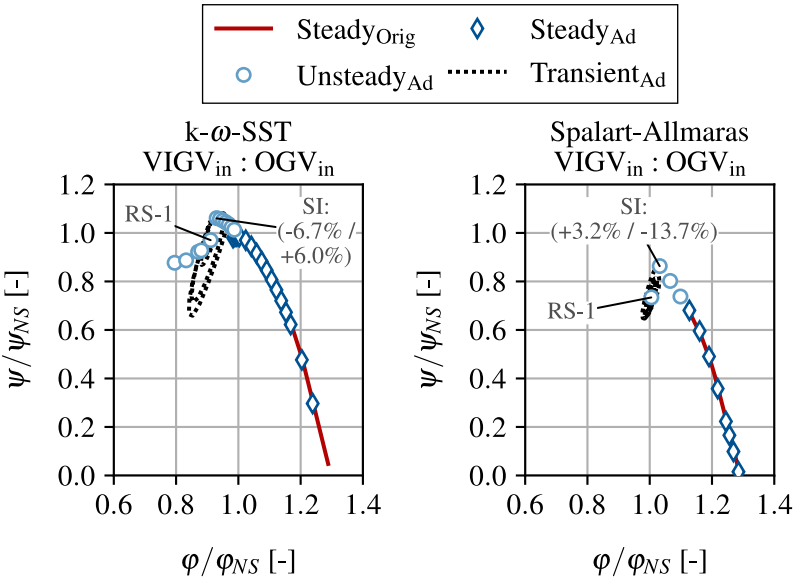

Figure 6.8: Compressor performance represented by the total-to-static pressure rise ψ against the flow coefficient φ

The unsteady procedure was initiated close to the steady-state near stall point. In comparison to the single-passage computations, an increase in the operating ranges can be observed for both applied turbulence models. The last stable operating points prior to stall inception (SI) are marked in Figure 6.8, indicating the individual discrepancy to the experimental stalling point. While for the k-ω-SST simulations flow rate and pressure rise are mismatched by about -6.7% and 6%, the SA-model evinces differences of approximately 3.2% and -13.7%. As the stalling process was initiated slightly prior to the peak of the total-to-static pressure rise characteristics, spike-type stall inception can be assumed. The expectation will be verified in section 6.2.3.

After crossing the stability limit, the compressor encountered volatile operating conditions. The transient behaviour is indicated by the dashed lines in Figure 6.8 and explicitly shown in Figure 6.9. With respect to the

k-ω-SST model, the pressure rise and flow rate oscillations are observed to diminish in time. As a consequence, the transient performance curve exhibits a spiral shape resulting in a stable operating point after about 25 revolutions. The point is denoted as RS-1 in the compressor map. Further throttling resulted in additional solutions which converged after about 10 revolutions each. Contrary to this behaviour, the SA model did not yield stable conditions within the computed time range of 35 revolutions. The depicted operating point RS-1 hence represents the average flow rate and pressure rise. With the loss in pressure rise being comparably mild in both characteristics, the arising disturbance can already be associated with progressive or part-span stall introduced in section 2.4.1. The hypothesis is evaluated in section 6.2.8.

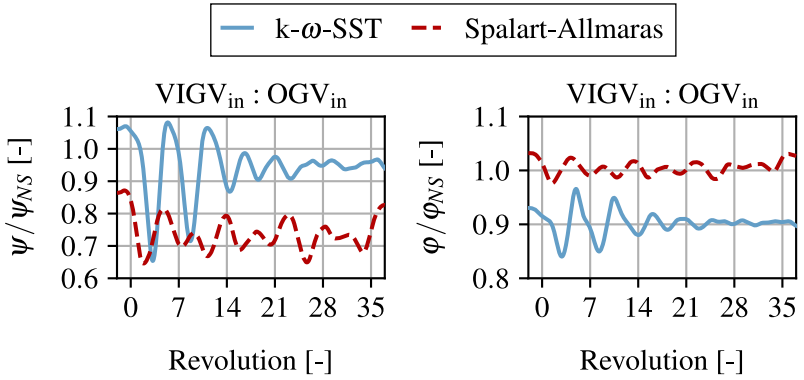

Figure 6.9: Oscillations in flow coefficient φ and pressure rise coefficient ψ as the compressor transitions into stall

As the performance branch at stalled conditions could not be acquired experimentally, respective data for comparison was not available. In order to verify the stall computations, the results are subsequently validated against stall cell details derived from unsteady pressure signals. Plausibility and accuracy are hence primarily examined on the basis of the stall cell speed ω_{RS}, count n_{RS} and circumferential extent Θ_{RS}. In the following, this is done with focus on those operating points marked as RS-1 as they include both the stall inception process and the accompanied transition into stall.

6.2.3 Circumferential pressure distributions

In order to derive the stall inception type and stall cell propagation speed ω_{RS}, the circumferential distribution of the pressure traces is evaluated.

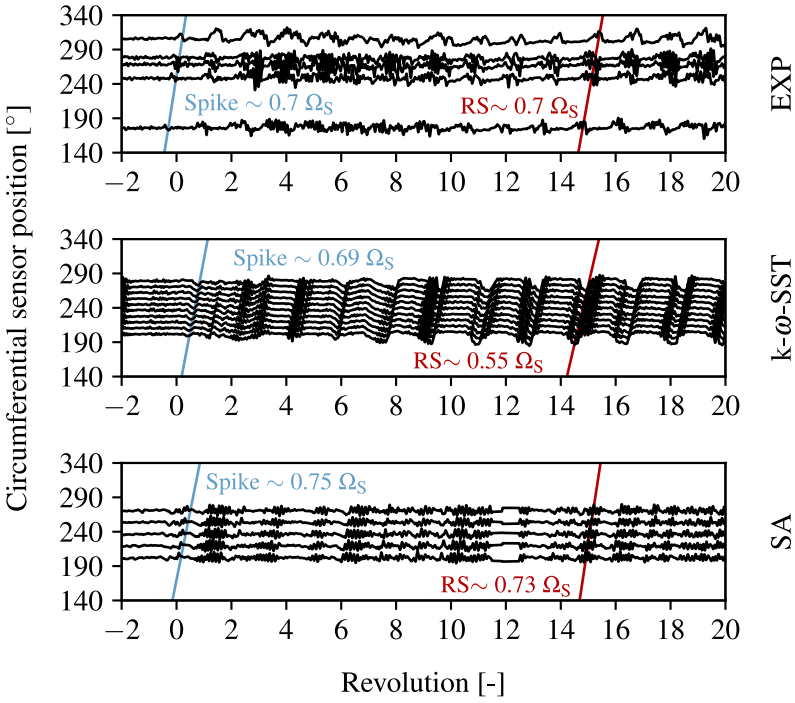

Figure 6.10: Circumferential distribution of pressure traces captured by experimental Kulite sensors and numerical probes in the stationary frame of reference

Both, the measured and computed results are illustrated in Figure 6.10. For clarity, the zeroth revolution denotes the onset of compressor stall. At this point, the experimental signal data evinces a sharp peak travelling in circumferential direction at about $0.7\Omega_S$. Considering the short-length scale and comparably high propagation velocity, the stall precursor can be determined as a spike-type disturbance. Within a few revolutions, the amplitude of the pressure fluctuation increases indicating the transition of

the spike into a stall cell. Interestingly, the propagation speed remains identical with ω_{RS}=0.7Ω_S despite the disturbance growth. This is rather atypical, as spikes were often observed to decelerate as they increase in size until they have become a fully developed stall cell.
With respect to the computation applying the k-ω-SST model, a spike-type fluctuation is noticeable in the pressure traces at revolution zero. The circumferential speed is at about 0.69Ω_S which agrees well with the measurements considering the error of 1%. As the compressor gradually transitions into stalled operation, the spike evolves into rotating stall. Due to the oscillating operating conditions, depicted in Figure 6.9, this process takes about 5 revolutions until the individual cell speed reaches a final value of ω_{RS}=0.55Ω_S. The propagation velocity hence differs by about 15% from the measurements.
Similar to the previous results, the data of the Spalart-Allmaras model computation exhibits the presence of a short-length scale disturbance prior to rotating stall. The spike-type precursor travels at approximately 0.75Ω_S. With a discrepancy of 5%, the result is in good agreement with the experimental findings. Since the performance curve was already observed to oscillate without reaching a stable operating point, neither the amplitude nor the frequency of the disturbance are noticed to change significantly over time. After about 15 revolutions, the propagation velocity is at about ω_{RS}=0.73Ω_S. In regards to the error of 3%, the finding correlates well with the experimental data.
In consideration of the propagation speeds derived from the circumferential pressure distributions, the results exhibited by the computations applying the Spalart-Allmaras model appear to be most promising, at first glance. In the following, however, a more clearer picture is provided.

6.2.4 Frequency spectra

For a detailed look at the various frequencies arising as the compressor crosses its stability limit, the spectrograms of the unsteady pressure signals are analysed. Based on these, the rotating stall frequency Ω_{RS} within the stationary frame of reference is determined. In combination with the previously gained knowledge about the cell speed ω_{RS}, the number of stall cells n_{RS} is derived using Equation 2.4.
The different frequencies emerging over time are presented in Figure 6.11. The corresponding amplitudes of the unsteady pressure ψ' are provided

as percentage of the pressure rise coefficient at near stall condition ψ_{NS}. The zeroth revolution on the abscissa denotes the beginning of compressor stall. For those points in time which are of particular interest, the frequency spectra are depicted additionally on the right. The plots hence allow for an easier determination of the primary engine orders which are defined by Equation 5.2.

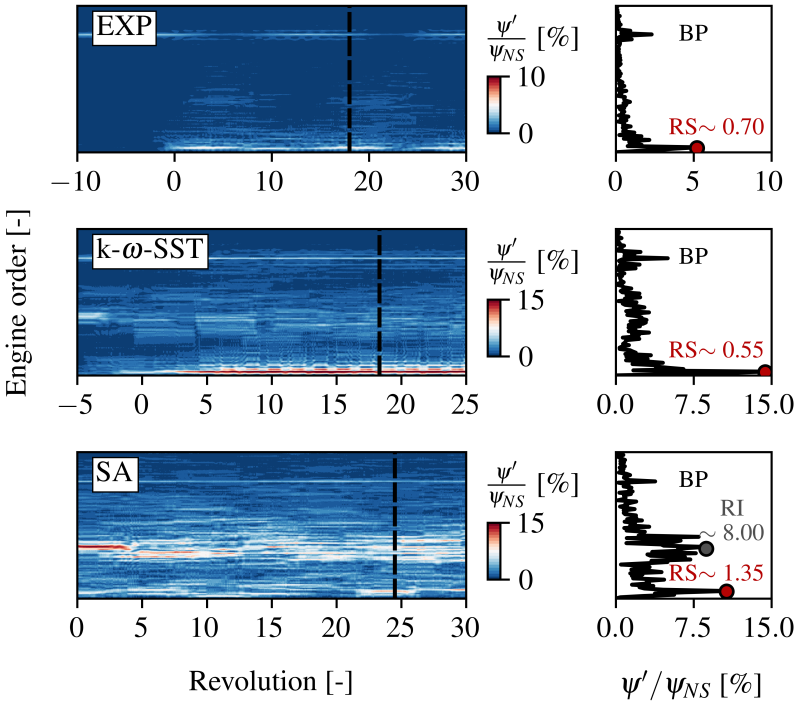

Figure 6.11: Spectrograms of the unsteady pressures acquired by experimental Kulite sensors and numerical probes in the stationary frame of reference

Clearly visible in all three datasets is the blade passing (BP) frequency at higher engine orders. As the blades continuously rotate at constant speed, the frequency band is permanently apparent. With respect to the experimental data, additional frequencies are not emerging before the zeroth revolution. As the compressor begins to stall, however, a significant peak

becomes identifiable in the frequency spectra which is assigned to the emerging rotating stall. The engine order of the disturbance is determined to 0.7 with a corresponding amplitude of 5.2% at revolution sixteen. The intensity, however, is observed to vary over time in accordance with the operating conditions presented before. Based on the rotating stall frequency $\Omega_{RS}=0.7\Omega_S$ and the individual cell speed $\omega_{RS}=0.7\Omega_S$, the number of stall cells is $n_{RS}=1$. For the experimental test rig, a single-cell rotating stall can hence be considered as main disturbance pattern.
In regards to the computation applying the k-ω-SST model, the emerging rotating stall is seen to exhibit some differences to the experimental data. First of all, the disturbance requires about five revolutions to establish a periodic signal which was also observed in the preceding section. After this time range, the corresponding engine order is at about 0.55 and hence below the measured value by -15%. The relative amplitude, in turn, is almost three times as large with $\psi'/\psi_{NS}=14.4\%$. One reason for the discrepancy in the unsteady pressure amplitude can be associated with a sightly different axial location of the numerical probes. In order to obtain the signals in the stationary frame, probes were located further downstream in the stator domain. Based on the presented results, a single-cell rotating stall with $n_{RS}=1$ can be concluded for the k-ω-SST computations, matching the experimental findings.
For the computation including the SA model, no constant frequency band besides that of the blade passing is clearly identifiable. At lower engine orders of approximately 8.0, a broad spectrum can be seen. As described in Day (2015) [13], such *broadband humps* are typically associated with rotating instabilities (RI). The term defines disturbances with a time varying nature due to changing frequencies, wave numbers and intensities. In this case, the average amplitude of the disturbance is $\psi'/\psi_{NS}=8.7\%$ with a wave mode of about 11. The highest peak in the frequency spectrum, however, is found at a smaller engine order of 1.35. The peak is associated with a discontinuously emerging rotating stall with an intensity of about 10.6%. Considering both, the rotating stall frequency of $\Omega_{RS}=1.35\Omega_S$ and the propagation speed of $\omega_{RS}=0.73\Omega_S$, the number of cells can be determined to $n_{RS}\approx 2$. In general, the results of the Spalart-Allmaras computation are found to agree rather poorly with the experimental data.

6.2.5 Unsteady casing wall contours

For a more detailed look at flow structures inside the rotor domain, the unwrapped casing wall pressure contours are presented. Thereupon, the circumferential extent of the rotating stall patterns Θ_{RS} is extracted.

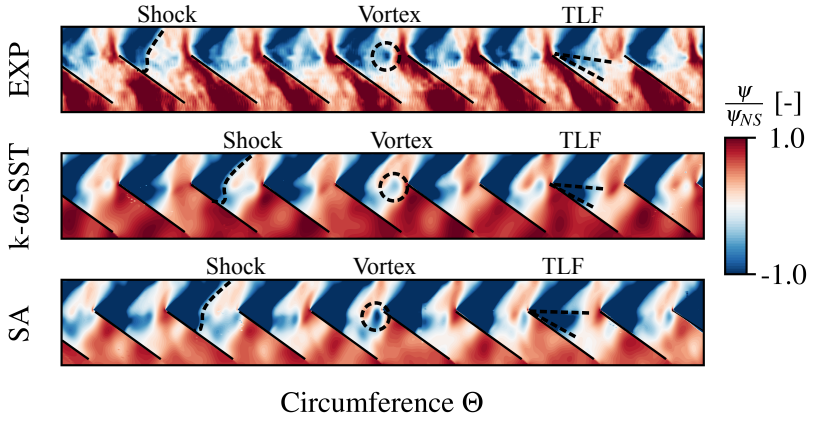

Figure 6.12: Casing wall pressure contours at near stall conditions

The results of the measured and computed datasets at near stall conditions are depicted in Figure 6.12. Note, that the experimental finding represents a pseudo-spatial pressure distribution, whereas the numerical data shows the pressure contour at a particular point in time. In all three illustrations the shock and tip leakage flows (TLF) are apparent in every passage. For an easier identification, the corresponding structures are exemplarily indicated by dashed lines. Besides these patterns, distinctive regions of low pressure are observed in proximity to single leading edges. With their time stamp being identical to the previously mentioned spikes in the pressure traces, they are assigned to the inception process. In more detail, these regions of low pressure are associated with radial vortices described in section 2.3.1 and labelled accordingly in the Figure.
The casing wall pressure contours at stalled conditions are presented in Figure 6.13. Large areas of perturbed flow comprising several blade passages are identifiable in these plots. With respect to the previously identified rotating stall, the regions are assigned to the disturbance. Based on the contours, the single-cell rotating stall becomes apparent which was

concluded for the experiments and k-ω-SST simulations. In contrast, the result derived from the computation applying the Spalart-Allmaras model exhibits the previously estimated twin-cell pattern. The disturbances, however, are observed to differ in size and intensity verifying that the pattern is not yet fully established at this point in time.

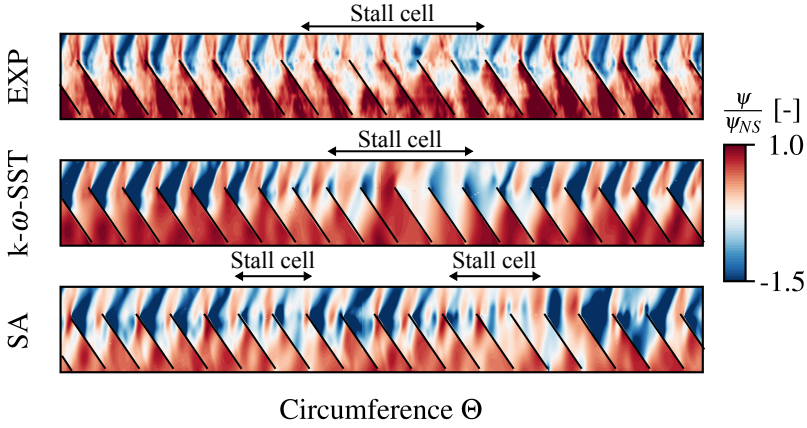

Figure 6.13: Casing wall pressure contours at stalled conditions

By analysing the pressure distributions along the leading edges, both disturbance extent and amplitude can be assessed roughly. The interval in which the pressure rise exceeds the mean value is considered as circumferential disturbance size. Hence, for the measured data a rotating stall extent of about Θ_{RS}=33% is derived, whereas the k-ω-SST and the Spalart-Allmaras simulations yield 25.1% and 21.9%. The results are therefore in acceptable agreement with the experimental findings. The solution of the k-ω-SST computation is considered best due to the matching stall cell count.

6.2.6 Summary of rotating stall details

For an enhanced comprehension of the disturbance properties determined in the previous sections, a general overview is presented. Based on the derived cell speed ω_{RS}/Ω_S, count n_{RS} and circumferential extent Θ_{RS}, the stall prediction capability of the numerical models is assessed.
The rotating stall details of the experimental and computational studies

are listed in Table 6.2. With respect to the k-ω-SST model, additional points computed at smaller mass flow rates than RS-1 (see section 6.2.2) are included as well for the sake of completeness. Also presented is the blockage factor λ_{RS} which was calculated via Equation 3.1 for each numerical point.

Model	$\frac{\varphi}{\varphi_{NS}}$ [-]	$\frac{\psi}{\psi_{NS}}$ [-]	$\frac{\omega_{RS}}{\Omega_S}$ [-]	n_{RS} [-]	Θ_{RS} [-]	λ_{RS} [-]
EXP	n/a	n/a	0.700	1.0	0.330	n/a
k-ω-SST	0.911	0.970	0.550	1.0	0.251	0.110
	0.881	0.928	0.500	1.0	0.287	0.162
	0.871	0.922	0.490	1.0	0.316	0.174
	0.832	0.887	0.473	1.0	0.421	0.224
	0.795	0.877	0.466	1.0	0.503	0.262
SA	1.005	0.734	0.730	~2.0	0.219	0.086

Table 6.2: Measured and computed rotating stall details

In general, the computations applying the k-ω-SST-model exhibit the best agreement with the experimental data with a matching single-cell rotating stall and discrepancies in cell speed and size of about 15% and 7.9%. Considering those operating points at reduced flow rates, an improvement with respect to the circumferential cell size is apparent. The trade-off, however, are larger differences in the cell propagation speed as throttling the compressor led to reduced values of ω_{RS}/Ω_S. The correlation between cell growth and cell propagation speed was already observed by Day (2015) [13] who stated that larger disturbances usually rotate slower.
Regarding the SA model simulation, a different stalling pattern was observed. Although the individual propagation speed of ω_{RS}/Ω_S=0.73 agrees well with the experimental findings, the number of circumferential modes is determined to n_{RS}=2. Furthermore, the emerging rotating stall was accompanied by secondary disturbances associated with rotating instabilities. These, in turn, were not observed in the experimental data. Conclusively, the SA model was not applied hereinafter for further investigations of rotating stall.

6.2.7 Spike-stall structure

In the previous sections, spike-type stall inception was concluded to initiate the stalling process in the one-and-a-half stage high-speed compressor. In this part, the fluid dynamic process leading to the formation of the spike as well as its structure will be discussed.

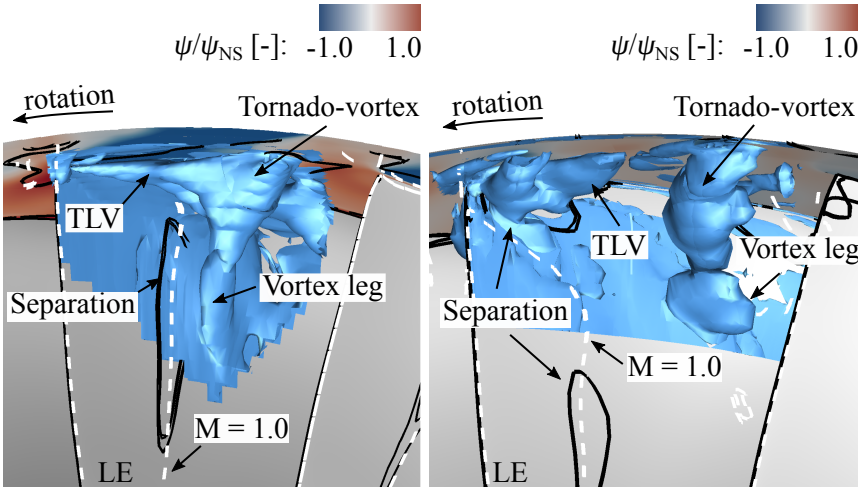

Figure 6.14: Formation of radial vortices at different operating conditions resulting in spike-type stall inception

The flow conditions in the rotor tip area of the numerical computations are depicted in Figure 6.14. Presented are the results of the k-ω-SST model simulations.
The conditions prior to the stall onset are shown in part A of the figure. Included is the iso-surface of the λ_2 criterion visualizing the already well-known vortex-tube. The short length scale disturbance can be observed to draw fluid from the tip leakage vortex (TLV) while connecting the casing wall and the blade suction side through the vortex leg. Also illustrated by the black lines is a region of reversed flow indicating a blade suction side separation at mid-chord. As the location of the recirculation area coincides with the white iso-line of M=1.0, there is indication for a shock-induced boundary-layer separation. Further downstream, the suction side separation begins to roll-up, eventually forming the vortex leg. As the

disturbance emerges inside the passage, it propagates solely downstream, barely influencing the adjacent blades.
With the operating point moving towards the stability limit, the vortex-tube grows in size. As a result, the passage becomes blocked by the enlarged disturbance leading to spill-forward. Due to the accompanied increase in incidence of the adjacent blade, the suction side separation is now triggered at the leading edge, as shown in Figure 6.14-B. Consequently, the interaction between tip leakage flow and leading edge separation initiates the radial vortex further upstream. At this stage, the propagation process described by Pullan et al. (2015) [12] begins. With the disturbance arising upstream, it gets caught by the following blade triggering a new leading edge separation. The flow process continues accordingly, involving the disturbance to start travelling in circumferential direction and eventually resulting in rotating stall.

6.2.8 Stall cell structure

Both the experimental data and computational findings revealed large disturbances affecting several passages once the compressor entered the stalled performance branch. Similar to the previous section, the structure of the corresponding stall pattern is presented and discussed.

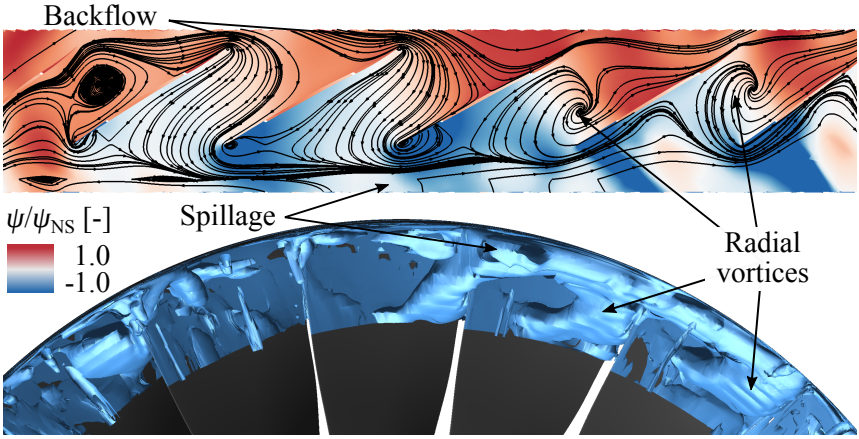

Figure 6.15: Stall cell structure exhibited in the computations applying the k-ω-SST model at RS-1

Figure 6.15 illustrates the contours of the pressure rise coefficient ψ in combination with the iso-surfaces of the λ_2 criterion derived from the computations using the k-ω-SST model. The depicted area corresponds to the region covered by the stall cell. Based on the indicated streamlines, three distinctive flow mechanisms can be observed which are involved in forming the passage blockage. These are the spillage along the rotor leading edges, the formation of radial vortices and the backflow entering the passages in proximity to the trailing edges. In contrast to the three-dimensional structure reported by Dodds and Vahdati (2015) [18] (see Section 2.4.2), the stall cell is not represented by a single vortex blocking multiple passages. Instead, the stall cell includes numerous radial vortices which appear to be triggered by the spill-forward. With respect to the radial extent, the stall cell is found to cover a region between 85% to 100% blade span.

6.3 Conclusions

In this chapter results of steady and unsteady computations were presented to study the performance as well as flow mechanisms of the TU Darmstadt high-speed compressor and create a numerical baseline for the subsequent low-fidelity computations. The general findings related to the initial research questions are as follows:

6.1-1: At steady conditions, the computational results matched the measured compressor performance characteristic within an error of 1%. With respect to the stability limit, the prediction of the stall onset varied for each investigated turbulence model. While the k-ω and k-ω-SST models underpredicted the stalling point by 2.2%, the Spalart-Allmaras model exhibited the performance drop at 7.1% higher mass flow rates.

6.1-2: The unsteady computations revealed the same spike-type inception mechanism prior to compressor stall as the experimental data. For both, the k-ω-SST and SA model the disturbance propagation speed was found to agree well with the measured value of $0.7\Omega_S$. More precisely, the discrepancies were about 1% and 5%, respectively. While the application of the k-ω-SST model led to an underprediction of the stalling point by about 6.7% in flow rate, the difference for the SA model computation was 3.2%.

6.1-3: At stalled conditions, the k-ω-SST model showed a single-cell rotating stall also observed in the experimental results. Cell speed and circumferential size, however, differed by about 15% and 7.9%. The Spalart-Allmaras model did not show a periodic rotating stall although the computations were performed for 35 revolutions. Despite the good agreement regarding the cell propagation velocity with a discrepancy of 3%, the discontinuously emerging rotating stall exhibited two cells. Furthermore, the disturbance pattern was affected by a rotating instability not observed in the experimental data. Consequently, the Spalart-Allmaras model is not used for further studies on rotating stall. Instead, the k-ω-SST model is applied exclusively.

6.2-1: The spike-type disturbance initiating the stalling process was found to correspond to a radial vortex in proximity to the blade tips. Initially, the perturbation originates from shock-induced boundary layer separations forming a tube while drawing tip leakage flow. In the early stage, the disturbance emerges near mid-chord only able to propagate downstream. As the operating point moves towards the stability limit, the vortex grows in size blocking the passage and leading to spill-forward. Due to the increased incidence, the adjacent blade exhibits a leading edge separation with the vortex tube forming further upstream. At this stage, the disturbance starts propagating circumferentially by triggering a leading edge separation on the next blade and initiating compressor stall.

6.2-2: After stall inception, the compressor encountered transient operating conditions with alternating pressure ratios and mass flow rates. Due to the oscillations, the emerging single-cell rotating stall varied in size and intensity.

6.2-3: The stall-cell was observed to mainly cover a fraction of the blades between about 85-100% span and is hence associated with part-span stall. The three-dimensional structure was found to include flow mechanisms like spill-forward, backflow and multiple radial vortices leading to the passage blockage.

Chapter 7
Low-fidelity computations

The development of reduced-order models for rotating stall predictions has been an active field of research for decades. Different approaches used to investigate the unsteady phenomenon were presented and discussed in Section 3.1.
In this chapter the principal idea behind those low-fidelity models only resembling a fraction of the annulus is picked up. As these were reported partly successful in reproducing the number of stall cells and their rotational speed, they are considered a promising approach.
Contrary to previous studies, however, the investigations are focusing on the part-span rotating stall exhibited in the high-fidelity computations. Moreover, the approaches applied do not rely on any additional simplifications other than radial contractions.
The main questions to be answered in this chapter are:

RQ 7.1 *To what extent are the applied low-fidelity models able to predict rotating stall?*

RQ 7.2 *What are the requirements and limitations of such an approach for accurate predictions?*

7.1 Methodology

In order to provide a general overview, the methodology pursued to predict and study rotating stall with less computational effort is described below. Thereupon, the different low-fidelity models applied in this work are presented.
In section 3.1.4 two-dimensional and quasi two-dimensional approaches used to study rotating stall were discussed. In many cases, the computational models were reported to show good agreement with experimental data. On the downside, all of these methods were limited to full-span stall with the computational domain resembling the compressor at mid-span. Apart from that, almost all of the reported models introduced additional simplifications to reduce computational costs. Examples are axially and circumferentially minimized domains as well as the neglect of viscous

or compressible effects. Any discrepancy observed in the predicted cell speed and size is hence assumed to originate from these additional constraints.

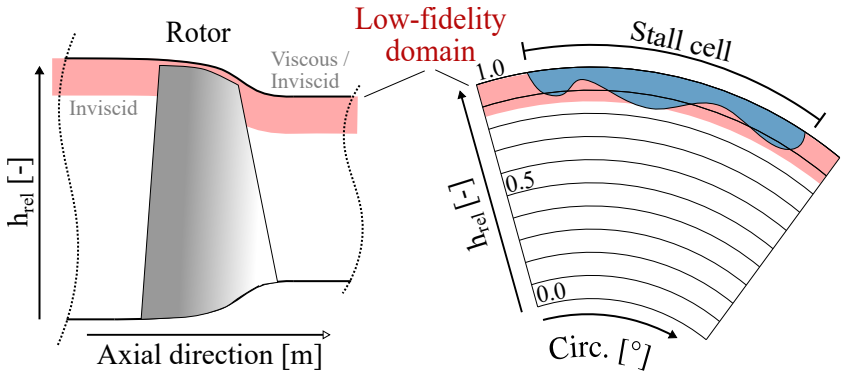

Figure 7.1: Sketch of the intersection between low- and high-fidelity domain

The models studied in this work differ from other reported methods in two ways. First and foremost, the general approach focuses on part-span rotating stall. For this reason, the high-fidelity computations are subsequently used as baseline or reference. Secondly, only radial effects are diminished or neglected. Further simplifications are not included in order to be consistent with the reference computations.
In general, the low-order models were characterized by reducing the high-fidelity domain to a narrow subregion at a determined radial location. As the part-span rotating stall was found to emerge in the tip region between 85% to 100% span, the reduced models resembled the compressor accordingly. The intersection between low- and high-fidelity domain is depicted exemplarily in Figure 7.1. To ensure comparable meshes, the amount of radial grid points was kept identical to the number of nodes applied in the corresponding model region within the baseline domain. While the hub boundary was always treated as inviscid to prevent any boundary layer growth, the tip boundary was either viscous or inviscid. If the actual casing contour of the high-fidelity model was included, a viscous boundary condition was used to be consistent with the baseline model. Otherwise the tip boundary was also treated as inviscid.

As the influence of both, radial location and extent was initially unknown, four different model variations were investigated. These are distinguished as follows:

Lofi-1: The reduced model reached from 85-100% span, fully resolving both, rotor and stator radial gaps.

Lofi-2: Similar to Lofi-1, the domain resembled all geometries located between 85-100% span. However, radial gaps were excluded in order to quantify related effects and verify whether they have to be included for accurate stall predictions.

Lofi-3: The model was located at 95% relative channel height with a radial width of 0.5% span. Due to the minimal extent it is considered quasi two-dimensional.

Lofi-4: Similar to Lofi-3, the model was of quasi two-dimensional nature and located at 90% span with a radial extent of 0.5%.

The procedure for all low-fidelity computations was similar to the baseline approach. Starting from a steady-state single passage calculation, the nozzle area ratio was reduced stepwise until the compressor reached its stability limit. Thereupon, unsteady full annulus computations were conducted. Each operating point was calculated for about 30-60 revolutions until the signal of the emerging disturbance was periodic within a time frame of at least 10 revolutions. With reference to the quasi two-dimensional models (Lofi-3/4), the wall clock time per revolution on 240 CPUs was approximately 15 minutes. This corresponds to a time reduction of 92% compared to the high-fidelity computations.

7.2 Performance characteristics

For an easy identification of the stalled and unstalled operating conditions, the compressor performance curves are presented.
Figure 7.2 shows the computed results of the different low-fidelity approaches. Also included is the data of the baseline model for reference. To enhance the comparability, the corresponding flow quantities were extracted at identical span locations as applied in the respective low-fidelity domains. Moreover, each compressor characteristic is divided into a stalled

and unstalled portion.

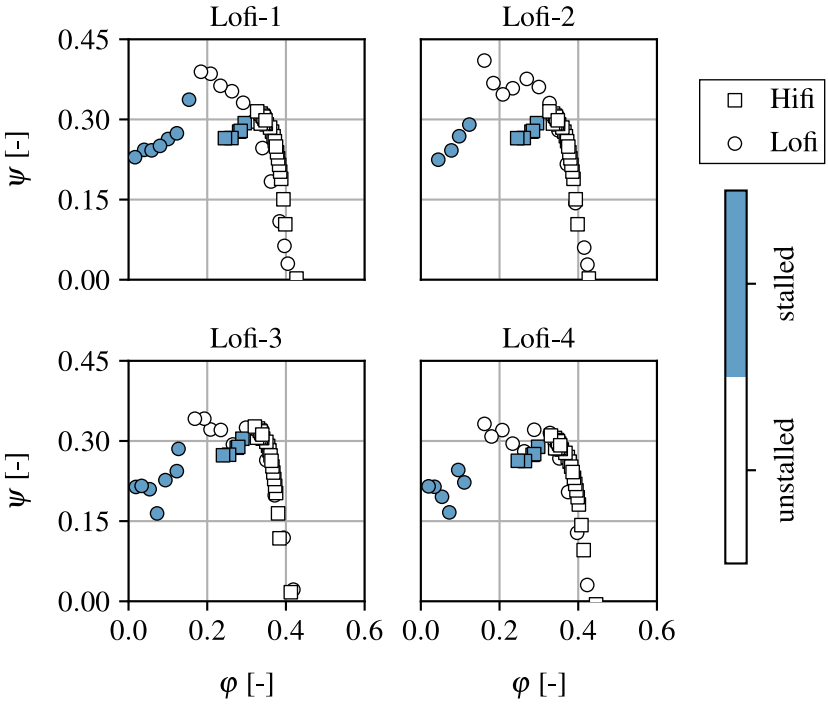

Figure 7.2: Comparison of the total-to-static pressure rise characteristics computed by the high- and low-fidelity models

Considering the unstalled performance branches, the reduced models match the reference characteristics well. The beginning of compressor stall, in turn, is shifted towards smaller flow coefficients in all low-fidelity computations. Also striking is the initial drop in the pressure rise coefficient ψ prior to the stalling point exhibited by those models without tip gaps (Lofi-2/3/4). The interim pressure loss was found to originate from a pre-stall disturbance which is discussed in section 7.4 in greater detail. With respect to the stalled performance branches, none of the reduced models matches the results of the high-fidelity calculations. The reason for this is most likely the delayed stall onset.

7.3 Stall onset

The investigated reduced-order models evinced the transition into compressor stall at smaller flow coefficients than the baseline computations. Subsequently, the origin of this behaviour is discussed.

$$DF = 1 - \frac{w_{ex}}{w_{in}} + \frac{\Delta w_\theta}{2\sigma \cdot w_{in}} \tag{7.1}$$

The maximum loading a compressor blade can bear is usually assessed using the well-known diffusion factor DF by Lieblein et al. (1953) [76]. The coefficient is defined by equation 7.1 and relates a blades pressure rise capability to the suction side boundary layer thickness. Based on this, the parameter can be applied to identify a critical value DF_{max} at which the blade row stalls.

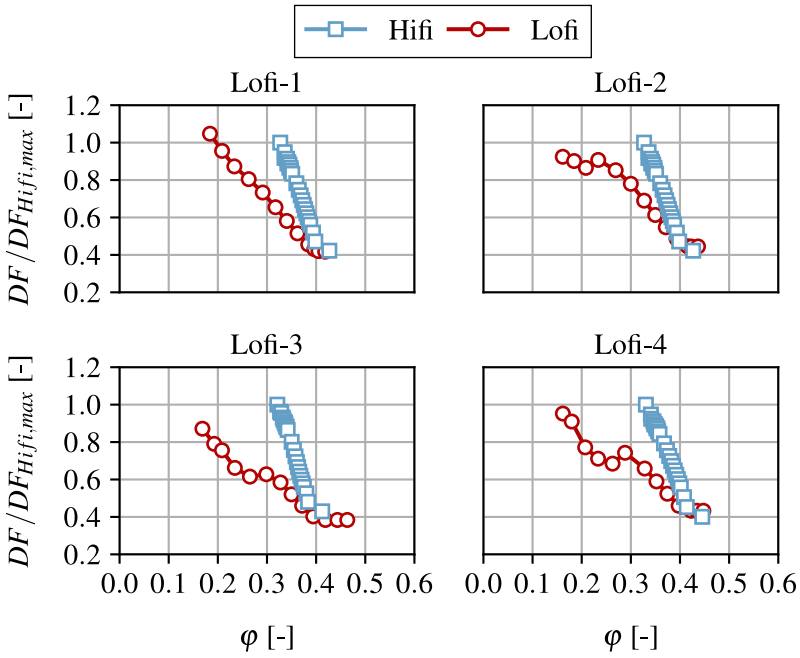

Figure 7.3: Comparison of the rotor diffusion factors $DF/DF_{Hifi,max}$ at stable operating conditions

In order to evaluate the differences in the maximum loading, Figure 7.3 depicts the diffusion factors against the flow coefficient for the high- and low-fidelity models. As before, the baseline data was extracted at span locations comparable to the respective low-fidelity domains. For an easier assessment, the diffusion factor DF is set in relation to the maximum loading exhibited in the high-fidelity computations $DF_{Hifi,max}$.
For all simulations a trend towards higher diffusion factors with decreasing flow coefficient can be observed. As expected, the blade loading hence increases as the compressor is throttled. However, for all reduced-order models a less progressive increase in $DF/DF_{Hifi,max}$ towards smaller values of φ can be noticed. With respect to the maximum diffusion coefficient in proximity to the stability limit, only slight discrepancies between the high- and low-fidelity calculations are identifiable. Thus, all investigated models exhibit stalled operating conditions at a similar rotor blade loading.
As the low-order models exhibit a weaker increase in $DF/DF_{Hifi,max}$ towards reduced φ, a closer look is taken upon the internal flow conditions. Thereupon, the origin of the delayed stall onset is determined. Therefore, Figure 7.4 illustrates the streamlines and velocities in the rotor domain at a constant flow coefficient of φ=0.36. The Lofi-1 model and the corresponding tip section of the high-fidelity simulation are shown.
Comparing the streamline contours, a less pronounced recirculation area within the rotor tip gap can be seen in the low-fidelity computation. With respect to the inlet profiles of the relative and circumferential velocities, w and w_θ, identical magnitudes are apparent. The exit profiles, in turn, exhibit larger discrepancies and generally higher velocities in the low-fidelity computation.
By taking the modelling approach of the reduced-order models into account, the mentioned observations are assumed to originate from the impeded radial flow diversion. In the high-fidelity computation, the tip region flow is able to migrate radially, leading to reduced rotor exit velocities. This diversion, in turn, is impeded by the hub line in the low-fidelity domain. Although modelled as inviscid, it still represents an impermeable border. As the flow does not divert radially, the velocities remain high at the rotor exit. With the diffusion coefficient depending on the ratio w_{ex}/w_{in} and the difference Δw_θ, the impeded radial migration hence reduces the rotor loading.

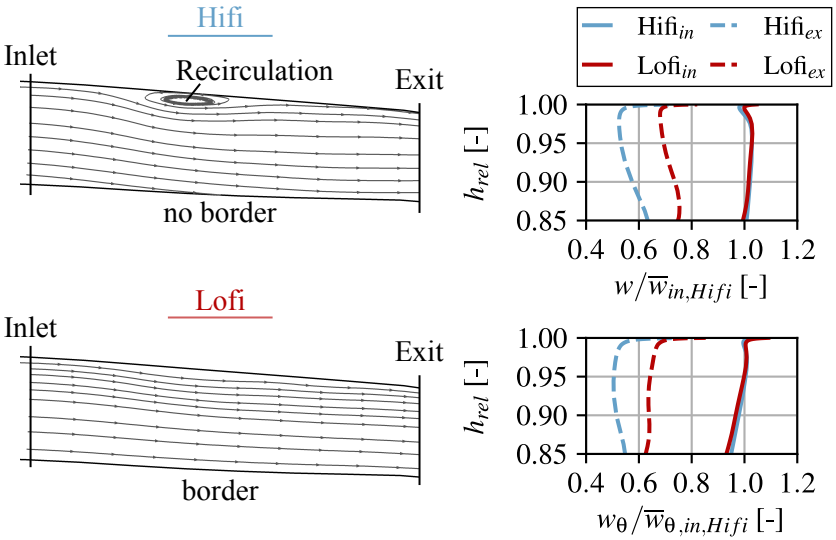

Figure 7.4: Streamline contours as well as inlet and exit profiles of the relative and circumferential velocities w and w_θ extracted from the Lofi-1 and high-fidelity model at φ=0.36

7.4 Pre-stall activity

The performance curves of those models without gaps (Lofi-2/3/4) exhibited secondary characteristics at near stall conditions. In this region, a slight drop in the total-to-static pressure rise was observed (see Figure 7.2). In order to understand the origin and nature of this performance loss, a more detailed evaluation is presented for the Lofi-3 computations. Note, that any of the three models evincing the pressure drop could have been applied at this point. As the Lofi-3 model was studied most extensively in this work, it was selected exemplarily.

The pressure rise characteristic of the Lofi-3 model is depicted in Figure 7.5. Therein, three regions are defined indicating the different compressor operating conditions. Besides the stable and stalled portions, a pre-stall branch is specified. The denotations (A) to (F) are introduced to refer to single operating points within these regions. As point (B) marks the beginning of the initial drop in pressure rise ψ, the corresponding circumferential flow field is additionally included in Figure 7.5. Clearly vis-

ible is a pattern of five distinct lobes with reduced levels of ψ explaining the drop in the performance characteristic.
For an enhanced view on the pattern movement, Figure 7.6 illustrates the histories of the rotor pressure rise for the selected operating points in the rotating frame of reference. In each sub-figure, the last 20 revolutions of each case are depicted, causing the broken x-axis. As in (A) the flow field is still steady and homogeneous, no pre-stall activity is visible. At point (B), in turn, the five-mode pattern is clearly identifiable. As the disturbance remains at a constant circumferential position over time, no relative motion to the rotor blades can be concluded. The individual speed of the lobes is hence $1.0\Omega_S$ and equal to the shaft speed. As the compressor is throttled towards the stall boundary, the pattern begins to slightly decelerate resulting in a movement contrary to the rotor. At point (E) the propagation velocity is $0.96\Omega_S$. As the compressor eventually crosses the stability limit at (F), rotating stall emerges with ω_{RS}/Ω_S=0.35.

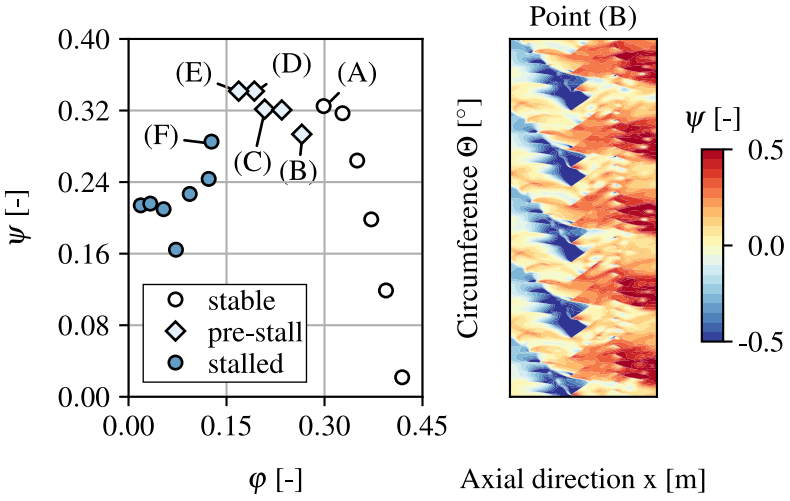

Figure 7.5: Total-to-static pressure rise characteristic of the model Lofi-3 including the unwrapped pressure contours at point (B)

Although the origin of the observed pre-stall disturbance remains unclear, the propagation mechanism is considered shock-related. A sketch of the

flow features assumed to be the primary drivers is illustrated in Figure 7.7. Depending on the relative position of the incoming flow to the shock pattern, the rotor blades either face increased or reduced incidences. At position (1), the upstream effect of the leading edge shock affects the inflow only marginally. As the compressor operates already at near stall conditions, the reduced flow rate results in a locally high incidence triggering a boundary layer suction side separation on the following blade. Due to the accompanied losses, the compressor performance drops. At position (2), the inflow encounters the oblique shock further upstream and is deflected as it passes the discontinuity. Due to the redirection, the rotor incidence is decreased leading to improved inlet conditions of the incoming blade. As the shocks are attached to the blades and hence travel at rotor speed, the pattern remains at a fixed circumferential position as observed for point (B).

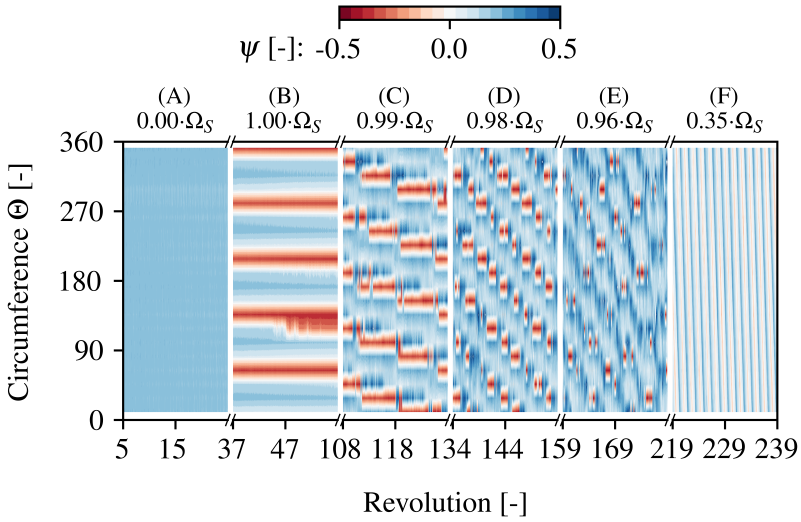

Figure 7.6: Circumferential pressure histories at operating conditions (A) to (F) illustrating the motion of the pre-stall disturbance in the rotating frame of reference

Towards smaller flow rates at near stall conditions, the rising incidence increases the induced flow separation on the blade suction side. As the blockage grows, spill forward is triggered on the leading edges. Accom-

panied with the flow skipping single passages, a distortion of the shock pattern begins to travel circumferentially. As a consequence, the flow disturbance propagates relative to the rotor as exhibited by points (C) to (E).

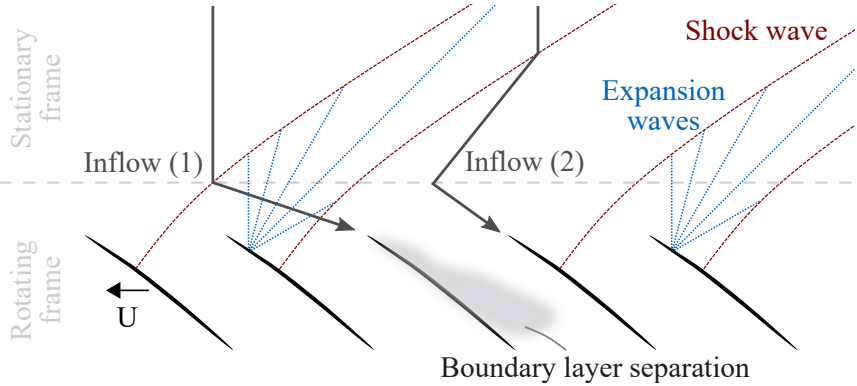

Figure 7.7: Sketch of the flow mechanisms involved in the propagation of the pre-stall disturbance

7.5 Stall cell speed and count

After analysing the near stall conditions and flow phenomena, the stalled compressor operation is explored in greater detail.
The discrepancy in rotating stall cell count Δn_{RS} and individual speed $\Delta\omega_{RS}/\Omega_S$ between the reduced and baseline computations is illustrated in Figure 7.8. As reference point RS-1 of the high-fidelity baseline computations was used. Among other stall cell details, the data is also listed in Table 7.1.
Regarding the number of stall cells, all investigated low-fidelity models initially show an equal pattern as the reference computation. The difference Δn_{RS} is hence found to be zero at most operation points. At flow coefficients of $\varphi < 0.08$, the quasi two-dimensional approaches (Lofi-3/4) exhibit a change from a single-cell to a twin-cell stall, wherefore $\Delta n_{RS} = 1$. The number of cells in the Lofi-1/2 computations, in turn, remains constant over the complete stalled operating range.
Regarding the stall cell speed, none of the models is found to match the baseline results. The smallest deviation at $\Delta n_{RS} = 0$ is brought forward by the Lofi-3 model with $\Delta\omega_{RS}/\Omega_S = -14.9\%$. It is hence considered the best

prediction and marked in Table 7.1.
Looking at the differences between the low-fidelity models, no significant discrepancies are noticeable for those configurations with equal span heights. The trends for the approaches 1 and 2 as well as for 3 and 4 are nearly identical. The main differences are the offsets in the stall onset as Lofi-1 and Lofi-3 enter stalled operating conditions at higher flow coefficients φ. The primary conclusion to be drawn from this is that the tip gap geometry included in Lofi-1 has no substantial impact on the stall cell properties.

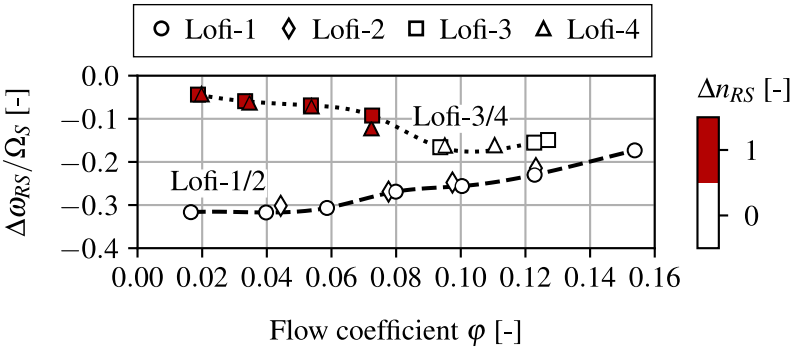

Figure 7.8: Differences in stall cell number Δn_{RS} and speed $\Delta\omega_{RS}/\Omega_S$ between the low- and high-fidelity computations

Model	φ [-]	$\Delta\frac{\omega_{RS}}{\Omega_S}$ [-]	Δn_{RS} [-]	$\Delta\Theta_{RS}$ [-]	$\Delta\lambda_{RS}$ [-]
Lofi-1	0.154	-0.173	0	0.000	0.271
	0.123	-0.230	0	0.028	0.438
	0.100	-0.256	0	0.079	0.512
	0.080	-0.269	0	0.142	0.577
	0.059	-0.307	0	0.227	0.642
	0.040	-0.317	0	0.318	0.697
	0.017	-0.316	0	0.255	0.766
Lofi-2	0.123	-0.214	0	0.033	0.456
	0.097	-0.248	0	0.112	0.538
	0.078	-0.269	0	0.139	0.599
	0.044	-0.302	0	0.309	0.693
Lofi-3	0.127	-0.149	0	-0.099	0.441
	0.123	-0.155	0	-0.070	0.470
	0.094	-0.166	0	0.023	0.555
	0.073	-0.092	1	-0.008	0.623
	0.054	-0.069	1	0.024	0.668
	0.033	-0.059	1	0.055	0.723
	0.019	-0.044	1	0.062	0.763
Lofi-4	0.110	-0.162	0	-0.037	0.513
	0.095	-0.162	0	0.014	0.549
	0.072	-0.122	1	-0.016	0.626
	0.054	-0.071	1	-0.002	0.671
	0.035	-0.063	1	0.060	0.720
	0.020	-0.044	1	0.076	0.760

Table 7.1: Relative stall cell details of all conducted low-fidelity computations

7.6 Stall cell sizes

In the following, the stall cell data is evaluated by focusing on the internal flow structures. Based on this, differences in the disturbance sizes are derived and discussed.

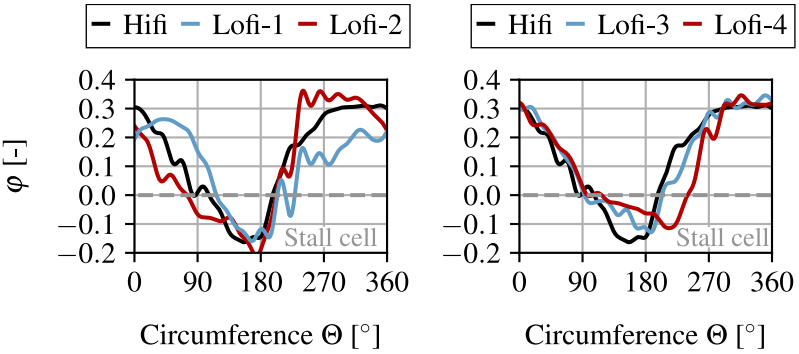

Figure 7.9: Circumferential profile of the flow coefficient φ extracted at the rotor leading edges used to evaluate the circumferential stall cell size Θ_{RS}

Figure 7.9 illustrates the circumferential distribution of the flow coefficient φ within the initial single-cell rotating stall. The profiles hence correspond to the first operating points in stall. The flow conditions were extracted at the rotor leading edge and represent a snapshot in time. Despite possible variations of the flow distributions per revolution, the instantaneous profiles are a useful indicator of the circumferential stall cell size. As the cells are considered as regions of recirculation, they are located at $\varphi < 0$ as depicted in the illustration. Based on this, the circumferential stall cell extent Θ_{RS} and the deviation from the high-fidelity computation $\Delta\Theta_{RS}$ are derived. In general, the differences to the high-fidelity results are observed to be comparably small. More precisely, the individual deviations $\Delta\Theta_{RS}$ are 0.0%, 3.3%, -9.9% and -3.7% for the models Lofi-1 to Lofi-4. The respective values are listed in Table 7.1 together with those at smaller flow rates.

A more global perspective is provided by the contour plots shown in Figure 7.10. Displayed is the instantaneous distribution of the flow coefficient

within the core compressor. Thereupon, the axial expansion of the single-cell rotating stall can be assessed.

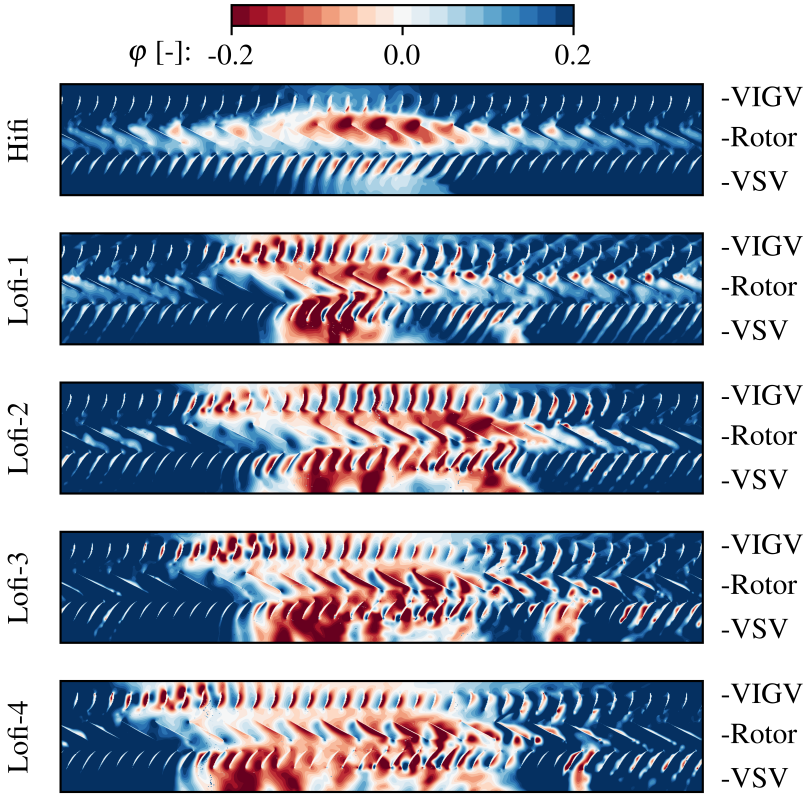

Figure 7.10: Unwrapped contours of the flow coefficient φ obtained from the low- and high-fidelity simulations

With respect to the high-fidelity computation, the stall cell is observed to comprise mainly the rotor blades with only small extension into the neighbouring rows. By contrast, the low-fidelity results exhibit a wide axial distribution of the stall cell. Regions of retarded flow are hence apparent within the VIGV, rotor and VSV. The smallest overall cell size is exhibited by the Lofi-1 model. For all subsequent models, the size of the recirculation region is found to be larger with the Lofi-4 approach evincing the broadest stall cell extent. A simple description of this observation

is provided by the difference in the blockage factor $\Delta\lambda_{RS}$. The deviations from the reference data regarding the stalled portion of the annulus are 27.1%, 45.6%, 44.1% and 51.3% for the models Lofi-1 to Lofi-4.

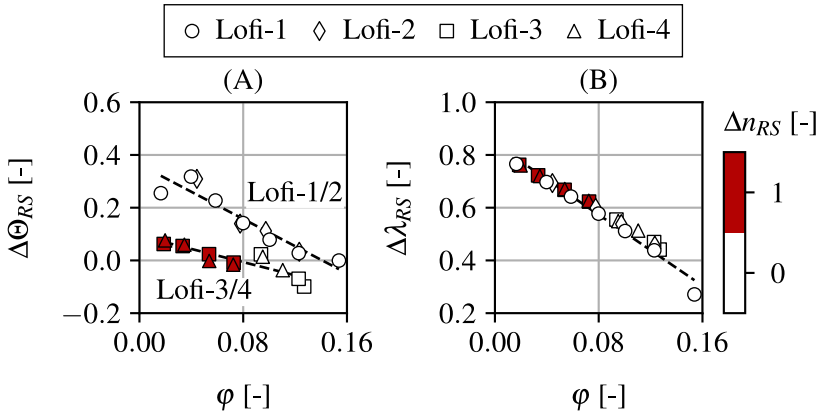

Figure 7.11: Differences in the circumferential disturbance size $\Delta\Theta_{RS}$ (A) and overall blockage factor $\Delta\lambda_{RS}$ (B) relative to the baseline computations

The derived disturbance sizes of each low-fidelity computation are shown in Figure 7.11. With respect to the difference in the circumferential extent $\Delta\Theta_{RS}$ a linear increase towards diminishing φ is identifiable. The growth rate, in turn, differs for the models Lofi-1/2 and Lofi-3/4. It appears, that the disturbances increase less rapidly in circumferential direction within the quasi two-dimensional domains. Despite the different trends, however, all of the investigated models evince a matching cell width at $\Delta\Theta_{RS}$=0.
By contrast, none of the approaches exhibits a satisfactory agreement with the blockage factor as depicted in Figure 7.11-B. The smallest discrepancy is noticeable for Lofi-1 with $\Delta\lambda_{RS}$=27.1%. For all models, in turn, a similar linear trend of $\Delta\lambda_{RS}$ towards reduced φ can be seen.

7.7 Rotating stall sensitivities

In the previous sections, the low-fidelity approaches were concluded to exhibit a discrepancy in stall cell speed and overall size compared to the

high-fidelity results. In the following, the link between these two stall cell properties is studied in further detail.
Figure 7.11-A illustrates the correlation between the deviation in relative cell speed $\Delta\omega_{RS}/\Omega_S$ and blockage factor $\Delta\lambda_{RS}$ for all low-order computations. For those cases with a matching stall cell count Δn_{RS}=0, the graphic shows an increasing discrepancy in propagation velocity with a rising difference in compressor blockage. The offset in $\Delta\lambda_{RS}$ is hence considered the main reason for the discrepancy in cell speed. In other words, as the reduced-order models initially exhibit large stall cells accompanied by high blockage factors, the individual cell speed is much smaller than experienced in the high-fidelity computations.

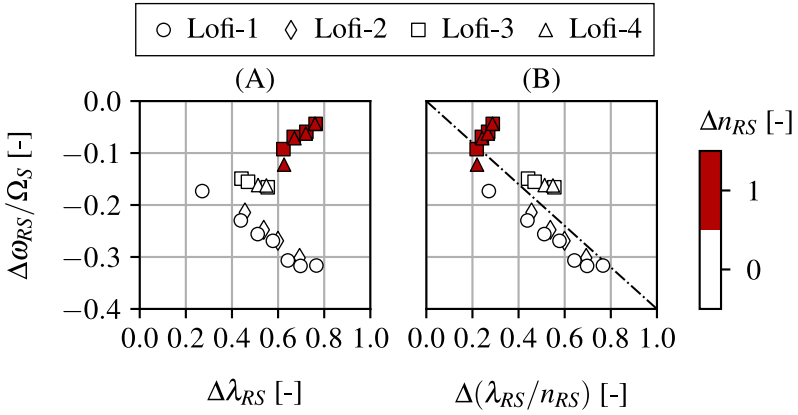

Figure 7.12: Correlation between $\Delta\omega_{RS}/\Omega_S$, $\Delta\lambda_{RS}$ and $\Delta(\lambda_{RS}/n_{RS})$

As the stall cells split up and form the twin-cell pattern at Δn_{RS}=1, the individual cell speed increases again leading to a diminished $\Delta\omega_{RS}/\Omega_S$, despite the large values of $\Delta\lambda_{RS}$. Considering, in turn, the individual blockage $\Delta(\lambda_{RS}/n_{RS})$ of each stall cell, the split-up results in two smaller flow disturbances. As the individual size is hence decreased, the cell movement increases again. The correlation between $\Delta\omega_{RS}/\Omega_S$ and $\Delta(\lambda_{RS}/n_{RS})$ is depicted in Figure 7.11-B. Clearly visible is the diminishing discrepancy in cell speed towards smaller differences in the individual blockage. Also included is the trend line through all points indicating an $\Delta\omega_{RS}/\Omega_S$ of zero at $\Delta(\lambda_{RS}/n_{RS})$=0.
Consequently, the accurate prediction of the stall cell details of the ref-

erence case requires the low-fidelity computations with Δn_{RS}=0 to eliminate the difference in $\Delta\lambda_{RS}$. As was shown in the previous section, the discrepancy in the blockage factor reduces linearly towards higher flow coefficients φ. At high values of φ, however, the reduced models operate on the stable branch of the performance characteristic as they exhibited a delayed stall onset due to an impeded radial migration. Low-fidelity models resembling only a fraction of the compressor annulus are hence concluded to be unsuited for predictions of part-span stall. This remains at least valid for those approaches including impermeable domain boundaries. On the other hand, the results explain the success of models applied to full-span stall which were reported in other works. As the blockage factor in full-span stall is usually large ($\lambda_{RS}\geq$30%, see Day (1976) [17]), the reduced-order methods are able to match the high values of λ_{RS} and hence the cell speed ω_{RS}/Ω_S.

7.8 Conclusions

In this chapter the capability of four different low-fidelity models to predict part-span rotating stall was investigated. The general approach was based on reduced-order models reported in the literature, only resembling a fraction of the compressor annulus. With respect to the opening research questions, the following conclusions can be drawn:

7.1-1 Each low-fidelity model initially matched the stall cell count n_{RS} exhibited in the high-fidelity computations.

7.1-2 The predicted stall cell speed did not show a satisfactory agreement. The minimum deviation from the reference data was $\Delta\omega_{RS}/\Omega_S$=-14.9%.

7.1-3 The single-cell rotating stall emerging in the low-order computations was found to have an equal circumferential extent Θ_{RS} as seen in the baseline simulation.

7.1-4 The reduced models evinced overall higher blockage factors λ_{RS} and axial expansions of the stall cells into the adjacent blade rows. The minimum discrepancy was $\Delta\lambda_{RS}$=27.1%.

7.2-1 The reason for the discrepancy in stall cell speed $\Delta\omega_{RS}/\Omega_S$ is found to be linked to the difference in the blockage factor $\Delta\lambda_{RS}$ and hence

overall cell size. In order to obtain matching cell speeds, the low-fidelity models are required to eliminate the difference in λ_{RS}.

7.2-2 In order to match the blockage λ_{RS} of the reference computation, the low-order approaches are required to drop into compressor stall at higher flow coefficients φ. Due to the impeded radial migration, however, the reduced models exhibit a delayed stall onset, wherefore they are not suitable for predictions of part-span rotating stall.

7.2-3 As full-span stall, in turn, is generally associated with higher blockage factors $\lambda_{RS} \geq 30\%$, the low-fidelity models are likely capable to match the overall cell size and hence the cell speed ω_{RS}/Ω_S. This may explain the success of comparable models used for full-span stall predictions which were reported in the literature.

Chapter 8
Design of experiments

The impact of compressor design parameters on rotating stall and its main properties stall cell count, size and speed are marginally understood. Moreover, little is known about the physics governing these stall cell details. The studies summarized in Section 3.2 indicate that some features influence rotating stall in one way or another. Due to parameter interactions, however, accurately assigning the measured effects is a formidable task.
In this chapter, the kinematics of rotating stall are studied numerically in greater detail. Therefore, due to particularly low wall clock times, the quasi two-dimensional Lofi-3 model is selected. With the model exhibiting a change in stall cell count it also offers the opportunity to have a closer look at the underlying mechanisms.
To ensure properly structured parameter investigations, a design of experiments (DoE) is conducted. The approach allows for a distinction of feature effects. In order to keep the design of experiments feasible, three main compressor parameters are varied, exclusively. These are the shaft speed, the guide vane angle and the nozzle throat area representing the throttle position.
The main research questions of this chapter are as follows:

RQ 8.1 *How do geometrical parameters affect the stall cell details?*

RQ 8.2 *What are the main flow physical drivers leading to a change in stall cell count and speed?*

8.1 Parameter space

For an enhanced understanding of the method used to study rotating stall sensitivities, the parameter space of the conducted design of experiments is presented.
As mentioned before, the DoE took three input factors or independent variables into account. These were the compressor shaft speed, the guide vane angle and the nozzle area ratio. For confidential reasons, the rotational speed and vane angles were quantified in relation to the reference configuration applied in the previous studies. Henceforth, the rela-

tive changes $\Delta\Omega_S$ and $\Delta\alpha$ are considered. For the nozzle throat area the non-dimensional ratio A^*/A was kept.

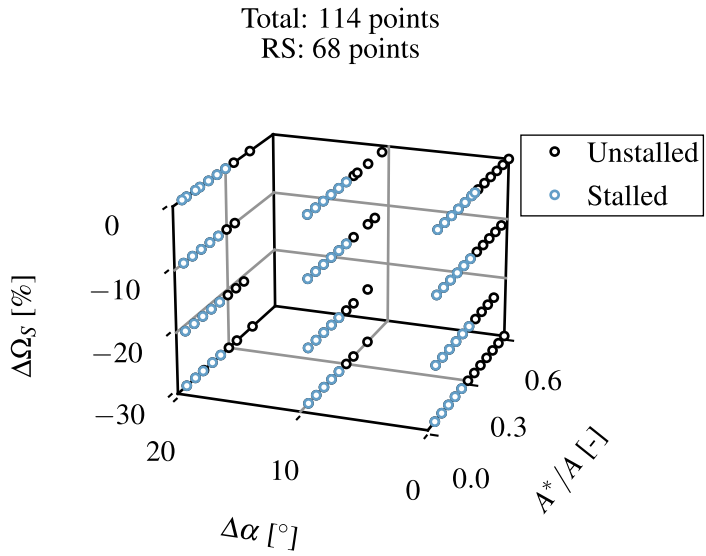

Figure 8.1: Parameter space of the conducted design of experiments including all unsteady computations with and without rotating stall

The parameter levels of each factor are given in Table 8.1 and, regarding $\Delta\Omega_S$ and $\Delta\alpha$, based on configurations investigated in the test facility. While the shaft speed was altered in steps of about 10%, the inlet guide vanes were varied incrementally by 10 degree with an increase in $\Delta\alpha$ indicating closing vanes. Note that changes made to the VIGV were always accompanied by variations of the VSV angle as well. The guide vane setting was based on the adjustment rule applied in the compressor test rig resulting in simultaneously closed or opened VIGV and VSV rows. The nozzle area ratio was reduced by increments of 5% starting near the stall onset point.
The complete parameter space is illustrated in Figure 8.1. In total 114 unsteady computations were conducted using the Lofi-3 model. Out of these calculations, 68 points exhibited rotating stall.

Parameter	Range
Shaft speed variation $\Delta\Omega_S$ [%]	0, -10, -21, -30
Guide vane angle variation $\Delta\alpha$ [°]	0, +10, +20
Nozzle area ratio A^*/A [-]	0.05 - 0.6

Table 8.1: Parameter levels investigated in the design of experiments

With the advantage of a highly resolved design space, the application of regression models and response surfaces becomes possible. By using such an approach, the rotating stall attributes can be estimated by means of the independent variables. The quality of the regression models is measured using the so called coefficient of determination R^2 defined by Equation 8.1. With $y, \widehat{y}$ and $\bar{y}$ representing the observed, predicted and mean values, R^2 indicates the proportion of the variance in the dependent variables that is predictable by the independent variables.

$$R^2 = 1 - \frac{\sum_i (y_i - \widehat{y}_i)^2}{\sum_i (y_i - \bar{y}_i)^2} \tag{8.1}$$

8.2 Performance characteristics

In order to get a first impression of the operational parameter influences, the overall compressor performances are presented and discussed.
Figure 8.2 depicts the total-to-static pressure rise characteristics of the different shaft speed and guide vane angle variations. Also included are the steady-state computations to visualize the stable branch of the performance curves. As both, the pressure rise and the flow coefficient are normalized by the circumferential speed, mainly adjustments of the inlet guide vanes are apparent. Hence, at steady conditions the characteristics of all three different guide vane settings are identifiable. As large values of $\Delta\alpha$ denote closed guide vanes, the corresponding performance curves are shifted towards smaller flow coefficients.
The regime of stalled compressor operation is located at flow coefficients of $\varphi \lesssim 0.15$ and denoted as region of interest (ROI). The number of stall cells n_{RS} in this region ranges from one to two and is indicated by the colour coding.

The pressure rise coefficient along the stalled branches is observed to be located around $\psi \approx 0.2$ which agrees reasonably well with the empirical correlation found by Day (1976) [17]. The formulation was introduced in Section 3.1.1 and approximates the stalled performance to $\psi \approx 0.225$.
The correlation postulated by Day (1976) [17] mainly takes the number of compressor stages into account. The current data, in turn, also indicates a dependency of ψ on the different rotating stall patterns. While the single-cell stall is located around $\psi \approx 0.25$, the twin-cell pattern exhibits an average pressure rise of about $\psi \approx 0.2$. Larger performance losses may hence be associated with a larger stall cell count.

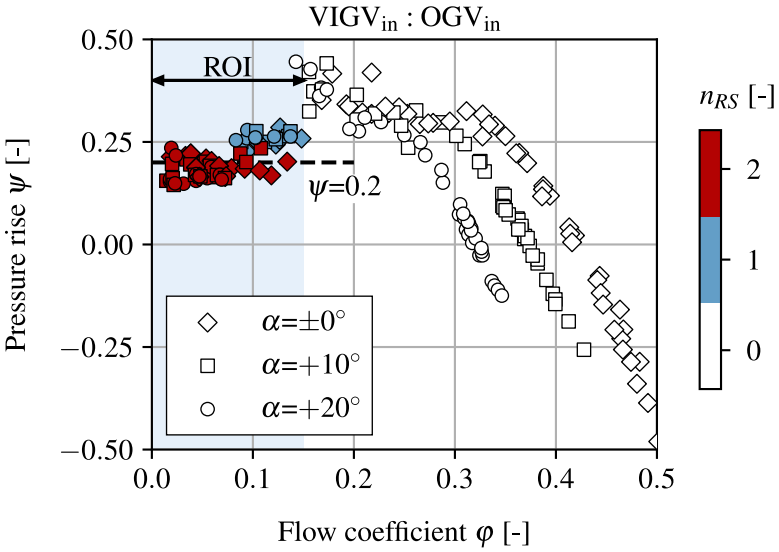

Figure 8.2: Total-to-static pressure rise characteristics of all computed parameter variations including the number of stall cells n_{RS}

8.3 Stall cell split-up

The analysis of the compressor performance curves already revealed the main rotating stall patterns emerging within the investigated design space. These are the single-cell and twin-cell rotating stall. For a closer look, the flow structures during the transition from one pattern to another are

presented.
Figure 8.3 illustrates the contours of the flow coefficient φ inside VIGV, rotor and VSV at three distinctive points in time denoted as (A), (B) and (C). Also shown in Figure 8.3-D are the unwrapped signals of φ captured by numerical probes in the stationary frame of reference. The different states (A) to (C) are denoted at the corresponding points in time.

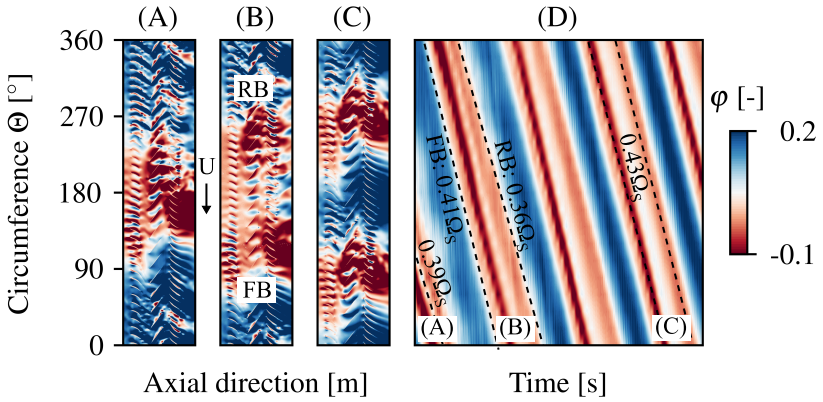

Figure 8.3: Contours of the flow coefficient φ inside the compressor at three different time steps (A), (B) and (C) as well as the unwrapped signals of the flow coefficient φ captured by numerical probes in the stationary frame of reference

From the distribution of the flow coefficient inside the compressor, the split-up of the single-cell rotating stall into two individual stall cells becomes visible. With respect to point (B) depicting the transition, the single cell can be seen to stretch out in circumferential direction resulting in an enlarged stall cell. Already identifiable, however, are two regions of high negative flow coefficient φ in proximity to the front (FB) and rear boundaries (RB) of the extended disturbance. As these slowly drift apart, they eventually form the final twin-cell pattern at point (C).
Based on the signal traces, the stall cell propagation velocities in circumferential direction can be derived. At point (A) for example, ω_{RS}/Ω_S is determined to 0.39. Moreover, the unwrapped signals indicate that the cell split-up results from a decelerating stall cell rear boundary. While at point (B) the front boundary is found to propagate at approximately $0.41\Omega_S$,

the rear boundary travels at about $0.36\Omega_S$ around the annulus. Due to the difference in speed, the single-cell rotating stall is finally divided into two stall cells. At point (C) both disturbances reach an equilibrium state again in which they rotate evenly with about $0.43\Omega_S$.

8.4 Rotating stall size considerations

Before evaluating the compressor parameter effects on rotating stall in greater detail, some considerations regarding the disturbance sizes are discussed.
In Section 7.6 an almost linear correlation between the flow coefficient φ and the circumferential stall cell extent Θ_{RS} was identified with the slope depending on the hub-to-tip ratio r_h/r_t. As the blockage factor λ_{RS} was found to be similarly linked to the flow coefficient φ, a correlation between λ_{RS}, Θ_{RS} and r_h/r_t can be derived.

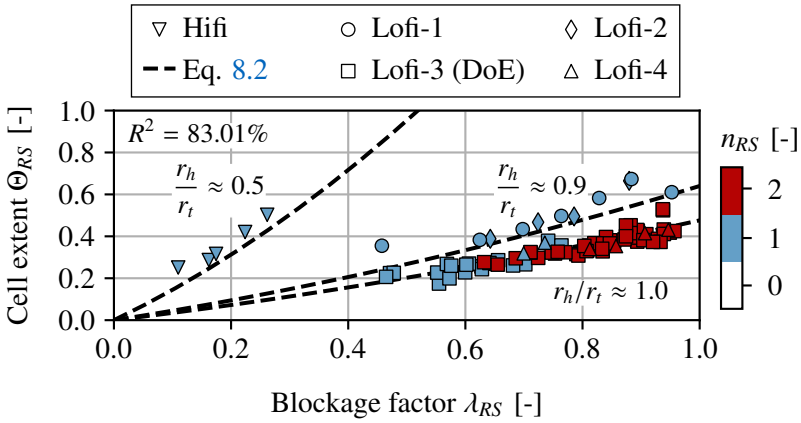

Figure 8.4: Correlation between the blockage factor λ_{RS}, the compressor hub-to-tip ratio r_h/r_t and the circumferential disturbance size Θ_{RS}

Figure 8.4 depicts the interdependencies for all computations conducted in this work. Clearly evident is the increasing circumferential extent Θ_{RS} towards higher blockages λ_{RS} for all models with equal hub-to-tip ratio. The growth rate, in turn, is found to decrease as the hub-to-tip ratio r_h/r_t rises. The parameter correlation is approximated by Equation 8.2. The

corresponding coefficient of determination indicates that the regression model is able to describe 83% of the variance in Θ_{RS} predictable from λ_{RS} and r_h/r_t. Especially with respect to the DoE results, the correlation is observed to match the data fairly well due to a marginal scattering of the points.

$$\Theta_{RS} = \frac{\lambda_{RS}^2}{7 \cdot \left(\frac{r_h}{r_t}\right)^3} + \frac{\lambda_{RS}}{3 \cdot \left(\frac{r_h}{r_t}\right)^2} \tag{8.2}$$

Consequently, the circumferential stall extent Θ_{RS} is without explicit consideration in the following sections. Instead, the stall cell sizes are solely evaluated on the basis of the blockage factor λ_{RS}. In case the circumferential extent is of particular interest, however, variations in λ_{RS} can be linked to changes in Θ_{RS} via Equation 8.2.

8.5 Operational parameter impact

Subsequently, the main effects of the independent variables $\Delta\Omega_S$, $\Delta\alpha$ and A^*/A are studied using statistical analysis and modelling where possible. The dependent variables or response quantities of interest are the rotating stall attributes λ_{RS}, n_{RS} and ω_{RS}/Ω_S.

8.5.1 Stall cell size

In Section 8.4 a link between the blockage factor λ_{RS} and the circumferential stall extent Θ_{RS} was established. In the following, the impact of the compressor parameters on λ_{RS} and hence Θ_{RS} is analysed.
For the present data a second-order polynomial regression model was applied. The formulation is represented by Equation 8.3. With a coefficient of determination of $R^2 = 97.54\%$ the model reflects the data sufficiently well. As some terms can be observed to show small constants, they generally have an insignificant impact on the predicted blockage value $\widehat{\lambda_{RS}}$. Neglecting these terms would still result in $R^2 = 95.16\%$. For the sake of completeness, however, they were kept.

$$\begin{aligned}\widehat{\lambda}_{RS} = &- \frac{29}{10} \cdot \left(\frac{A^*}{A}\right)^2 - \underbrace{\frac{64}{10^6} \cdot (\Delta\alpha)^2}_{\text{negligible}} + \underbrace{\frac{11}{10^7} \cdot (\Delta\Omega_S)^2}_{\text{negligible}} \\ &- \frac{40}{10^3} \cdot \frac{A^*}{A} \cdot \Delta\alpha + \frac{25}{10^3} \cdot \frac{A^*}{A} \cdot \Delta\Omega_S + \frac{78}{10^6} \cdot \Delta\alpha \cdot \Delta\Omega_S \\ &+ \frac{12}{10^2} \cdot \frac{A^*}{A} + \frac{54}{10^4} \cdot \Delta\alpha - \underbrace{\frac{13}{10^4} \cdot \Delta\Omega_S}_{\text{negligible}} + 0.914\end{aligned} \tag{8.3}$$

For an easier evaluation of the parameter effects, the model was used to create a response surface. The result is depicted in Figure 8.5. Shown is the variation of the estimated blockage factor $\widehat{\lambda}_{RS}$ for different combinations of the input parameters. In addition, scatter points are included representing the true values of λ_{RS} obtained from the numerical computations.

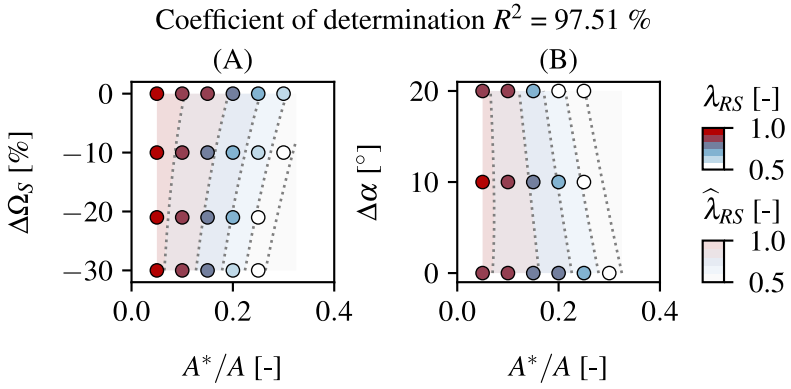

Figure 8.5: Response surface derived from Eq. 8.3 estimating the blockage factor λ

In general, the blockage factor can be observed to increase as the compressor is throttled by closing the nozzle throat area. Furthermore, assuming a

constant nozzle area ratio, the blockage decreases as the shaft speed is reduced. The effect becomes less prominent, however, towards small values of A^*/A. A similar impact can be seen for the guide vane variations. Closing the vanes at a constant nozzle area ratio reduces the blockage factor. The influence lessens at small A^*/A.

8.5.2 Stall cell number

Subsequently, a closer look is put upon the different rotating stall patterns observed in the design of experiments.

$$\pi(n_{RS,i} = j) = \frac{e^{f(i,j)}}{\sum_{k=1}^{J} e^{f(i,k)}} \dots \tag{8.4}$$

$$g(i,j) = a_j \cdot \left(\frac{A^*}{A}\right)_i + b_j \cdot \Delta\alpha_i + c_j \cdot \Delta\Omega_{S,i} + d_j \tag{8.5}$$

In order to improve the resolution of those regions exhibiting a distinct stall cell count within the investigated parameter space, a multinomial logistic regression model was applied. Such an approach is especially beneficial in case of a categorical distribution of the objective quantity. Each stall cell count is hence considered a class j enabling the model to capture abrupt changes in the cell count n_{RS} accurately. The multinomial logistic function is used to calculate the probabilities $\pi(n_{RS,i} = j)$ of the different cell counts to emerge at each observation i. Therefore, class-specific linear predictor functions $g(i,j)$ are applied. Both, $\pi(n_{RS,i} = j)$ and $g(i,j)$ are presented in their general forms by Equations 8.4 and 8.5. The coefficients used in the different predictor functions are listed in Table 8.2. Based on the calculated probabilities, the class exhibiting the highest score of π is chosen as prediction response. With a coefficient of determination of R^2=97.55%, the applied logistic regression model proves to have a sufficiently high quality for further investigations.
The response surface derived from the prediction model is illustrated in Figure 8.6. While the contour layers depict the estimated stall cell count $\widehat{n}_{RS}$, the scatter points indicate the number of stall cells n_{RS} obtained from the CFD. The correlation between $\Delta\Omega_S$ and A^*/A is depicted in (A), whereas (B) shows the relation between $\Delta\alpha$ and A^*/A. Clearly visible in all plots are the distinct regions of different patterns. Besides the unstalled

area without rotating stall, the single- and twin-cell regimes are apparent. The width of each region can be observed to depend on the operational parameters $\Delta\Omega_S$, $\Delta\alpha$ and A^*/A.

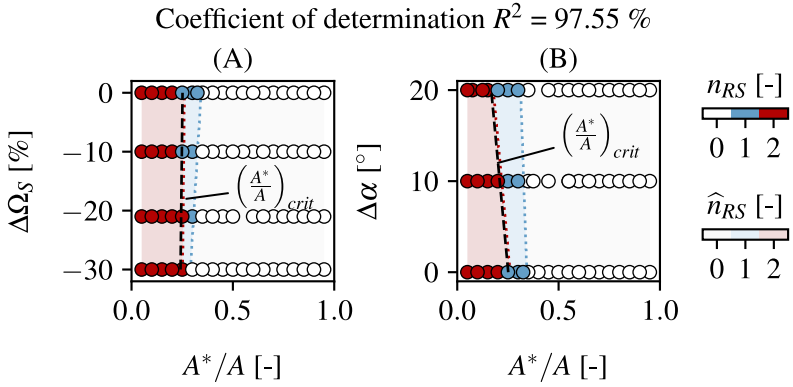

Figure 8.6: Impact of the varied compressor parameters on the number of stall cells n_{RS}

Regarding the beginning of the stalled regime, a shift towards higher nozzle area ratios is seen at increased shaft speeds and opened guide vanes. As the compressor total-to-total pressure characteristics are affected by $\Delta\Omega_S$ and $\Delta\alpha$, the respective stalling points move accordingly to other throttle or nozzle characteristics. Reaching characteristics and therefore stalling points that are shifted towards higher mass flow rates requires increased nozzle area ratios.

j	a_j	b_j	c_j	d_j
0	$2.53 \cdot 10^{2}$	$1.14 \cdot 10^{-1}$	1.16	−2.08
1	$-4.84 \cdot 10^{1}$	$-2.03 \cdot 10^{-1}$	$9.99 \cdot 10^{-1}$	42.64
2	$-1.80 \cdot 10^{2}$	$-4.76 \cdot 10^{1}$	$8.75 \cdot 10^{-1}$	55.85

Table 8.2: Class-specific coefficients used in the predictor functions

The regime of single-cell stall starts immediately after stall inception at almost all speeds and guide vane angles. The width of this area can be seen to decrease towards small values of $\Delta\Omega_S$ and $\Delta\alpha$, wherefore the twin-cell

region increases. In other words, reducing the shaft speed or vane angle at a constant nozzle area ratio within the single-cell regime results in the emergence of the twin-cell pattern. Moreover, the combination of the lowest parameter levels with $\Delta\Omega_S$=-30% and $\Delta\alpha$=0° leads to the occurrence of the twin-cell stall right after the stall onset without the appearance of the single-cell pattern. This can also be seen in Figure 8.6-A.

$$\left(\frac{A^*}{A}\right)_{crit} = -\frac{42}{10^4}\cdot\Delta\alpha + \frac{33}{10^5}\cdot\Delta\Omega_S + \frac{25}{10^2}$$
$$n_{RS} = \begin{cases} 2, & \text{if } \frac{A^*}{A} > \left(\frac{A^*}{A}\right)_{crit} \\ 1, & \text{Otherwise} \end{cases} \tag{8.6}$$

With the single and twin-cell regions being distinctively separated, the line in between is henceforth denoted as transition line or boundary. Along this line, the stall cell split-up takes place. As the boundary was observed to depend on the independent variables, it can be described by a regression function as well. The corresponding relation is given by Equation 8.6 and defines a critical nozzle area ratio $(A^*/A)_{crit}$ that depends on $\Delta\alpha$ and $\Delta\Omega_S$. Hence, for values of A^*/A greater than the critical nozzle area ratio, the twin-cell pattern can be expected. Otherwise, the single-cell stall emerges. Note that the conditions for n_{RS} in Equation 8.6 are only valid within the stalled operation regime.

8.5.3 Stall cell speed

After the evaluation of both stall cell size and number, the impact of the varied compressor parameters on the stall cell speed ω_{RS}/Ω_S is investigated.
Due to the combination of continuous slopes for n_{RS}=const. and discontinuous trends caused by cell count changes, a regression model of reasonable quality could not be derived for the given dataset. As mainly the influence of the operational parameters on ω_{RS}/Ω_S is of interest, however, the analysis of the individual main effects is considered satisfactory at this point. The corresponding plots are depicted in Figure 8.7. The main effects are derived by calculating the average of the objective quantity represented by $\overline{\omega_{RS}/\Omega_S}$ at each level of the input factors. This was done for

each cell count variation in order to study possible interdependencies.

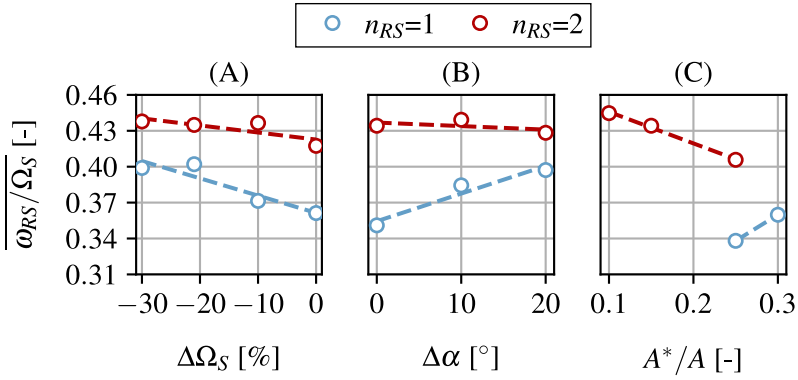

Figure 8.7: Averaged impact of the independent variables on the stall cell speed ω_{RS}/Ω_S for n_{RS}=1 and n_{RS}=2

The impact of $\Delta\Omega_S$ on ω_{RS}/Ω_S is illustrated in Figure 8.7-A. For both conditions, n_{RS}=1 and n_{RS}=2 a decrease in cell speed with increasing shaft speed can be noticed. The effect is less significant, however, with respect to the twin-cell stall. Since the pattern emerged at smaller values of A^*/A, the decreasing influence can also be linked to decreased nozzle area ratios. A similar behaviour of $\Delta\Omega_S$ was already observed for the blockage factor λ_{RS}.

For the guide vane angle variation $\Delta\alpha$, depicted in Figure 8.7-B, an increase of ω_{RS}/Ω_S with closing vanes is identifiable. Equivalent to $\Delta\Omega_S$, the overall effect is almost negligible for n_{RS}=2. The data may even suggest a contrary impact on the twin-cell stall with decreasing values of ω_{RS}/Ω_S towards higher $\Delta\alpha$. As the inclination of the trend line is almost zero, however, the marginally negative slope may also be based on random variances in the dataset.

Figure 8.7-C shows the effect of the nozzle area ratio on the stall cell speed. Two different trends are noticeable. While ω_{RS}/Ω_S decreases towards smaller A^*/A for n_{RS}=1, the opposite is apparent for n_{RS}=2. In other words, the single-cell stall appears to slow down as the mass flow rate is reduced, whereas the twin-cell stall accelerates.

8.6 Fundamental mechanisms

By means of statistical analysis methods the effects of geometrical compressor features on the main stall cell properties have been identified. The derived regression models even allow for predictions of the disturbance size and count. The models, however, are only valid within the investigated design space which makes them hardly applicable beyond design space boundaries.
To gain deeper insight to the nature of rotating stall, the subsequent sections take a closer look at general flow parameters and their impact. Based on these, a more universal explanation for the different effects is given. Furthermore, where possible, simple models are derived governing the dynamics of rotating stall and the underlying mechanisms.

8.6.1 Stall cell size

In the following, a more fundamental view on the disturbance growth is given by means of the blockage factor λ_{RS}.

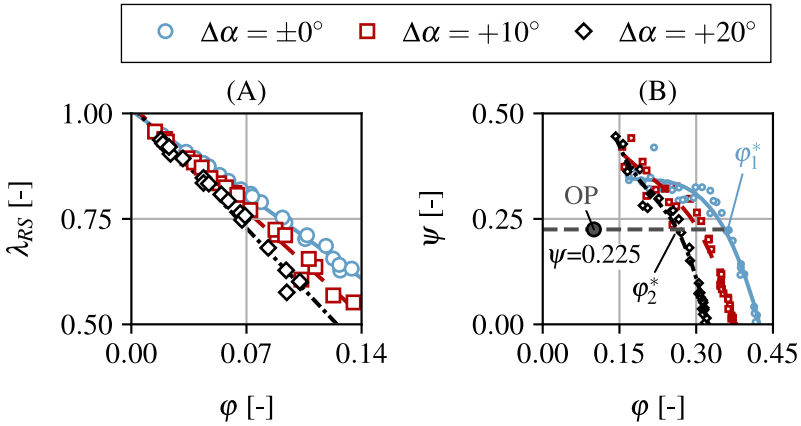

Figure 8.8: Correlation between the blockage factor λ_{RS} and the flow coefficient φ

Figure 8.8-A illustrates the correlation between λ_{RS} and the flow coefficient φ for the different guide vane angle variations $\Delta\alpha$. Clearly visible

for all settings is the linear increase of λ_{RS} towards decreasing φ. Furthermore, the functions negative inclination intensifies with rising $\Delta\alpha$. The disturbance growth rate towards small flow rates φ thus increases with $\Delta\alpha$. Consequently, closing the guide vanes at a constant flow coefficient reduces the blockage factor λ_{RS} and therefore the disturbance size. The effect lessens, in turn, at small flow coefficients.
The mechanism behind the decrease in cell size due to closed guide vanes at φ=const. is shown in Figure 8.8-B. Depicted are the total-to-static pressure rise characteristics of the different guide vane settings. Also included is the horizontal line at ψ=const.=0.225 as the compressor was previously found to operate closely to this value while in stall (see Section 8.2). Assuming the operating point (OP) to be located at φ=0.1, the guide vane effect on λ_{RS} can be explained by Equation 3.1. Therein, the main factor influenced by a change in $\Delta\alpha$ is φ^* indicating the conditions within the unstalled portion of the annulus. As the guide vanes are closed, the coefficient reduces from φ_1^* to φ_2^* as depicted in the Figure. As a consequence, λ_{RS} reduces according to Equation 3.1.
The dependence of λ_{RS} on the location of the performance curve within the compressor map impedes the determination of the disturbances sizes a priori. As both, the unstalled and stalled branches are required to calculate λ_{RS}, steady and unsteady computations have to be performed. However, the results provide valuable insights into the flow effects on the rotating stall sizes.

8.6.2 Stall cell number

In Section 8.5.2 a transition line was defined separating the single-cell and twin-cell rotating stall regimes. That boundary can be described by a combination of the operational parameters as given by Equation 8.6. For a more physical interpretation, the cell split-up is considered in further detail, subsequently.
As there exists an unambiguous line dividing regions of different stalling patterns, this transition boundary may also be considered as an iso-line of an unknown quantity χ_{RS}. The hypothesis would therefore state that the parameter χ_{RS} is of constant value along the transition boundary. Accordingly, the value corresponding to the iso-line would denote a critical magnitude $\chi_{RS,crit}$ similar to the critical nozzle area ratio $(A^*/A)_{crit}$. Slightly higher or smaller values of χ_{RS} would hence govern the single-

cell or twin-cell rotating stall, respectively.
By looking at the previously derived response surfaces depicted in Figure 8.6, the following two conditions for χ_{RS} become apparent:

(1) The parameter χ_{RS} remains constant when decreasing A^*/A while simultaneously increasing $\Delta\alpha$.

(2) The parameter χ_{RS} remains almost constant at A^*/A=const. while simultaneously increasing $\Delta\Omega_S$.

With the insights gained about the blockage factor λ_{RS} in Sections 8.5.1 and 8.6.1, similarities related to condition (1) become apparent. As small A^*/A generally lead to higher λ_{RS}, large $\Delta\alpha$ can be found to decrease λ_{RS}. A combination of both effects hence results in a constant blockage factor. With respect to condition (2), however, the blockage factor is not representing the parameter χ_{RS}. Increasing the shaft speed at a constant nozzle area ratio does not lead to constant values of λ_{RS}. Setting the blockage factor, however, into relation with the rotational speed of the compressor, as shown by Equation 8.7, fulfils conditions (1) and (2). The parameter χ_{RS} is henceforth denoted as relative blockage.

$$\chi_{RS} = \frac{\lambda_{RS}}{1 + \Delta\Omega_S} \tag{8.7}$$

The correlation between the relative blockage χ_{RS} and the number of stall cells n_{RS} is depicted in Figure 8.9-A. Clearly visible is the change in the stall cell count in proximity to a χ_{RS}=$\chi_{RS,crit}$≈0.8 which is designated as the critical relative blockage. Below this limit, the single-cell rotating stall is observed to be the dominant disturbance, whereas otherwise the twin-cell pattern emerges. Although two points are not evincing the expected behaviour, the overall validity is found remarkable in light of the transient nature of rotating stall.

$$\lambda_{RS,crit} = 0.8 \cdot (1 + \Delta\Omega_S) \tag{8.8}$$

Moreover, the parameter allows for further interpretations. With the cell count change relying mainly on λ_{RS} and $\Delta\Omega_S$, it becomes apparent that for each compressor shaft speed there must exist a critical blockage factor $\lambda_{RS,crit}$ defined by Equation 8.8. For a given speed, the single-cell pattern is hence limited to a certain blockage or size. If this size is exceeded,

the stall cell cannot sustain its extent anymore, wherefore it splits up. Towards lower speed, this critical size decreases with the twin-cell pattern becoming more prominent. At higher speeds, in turn, a single-cell pattern can maintain a larger extent. This may be due to the increase in kinetic energy transferred from the rotor into the stall cell. The effect is shown in Figure 8.9-B.

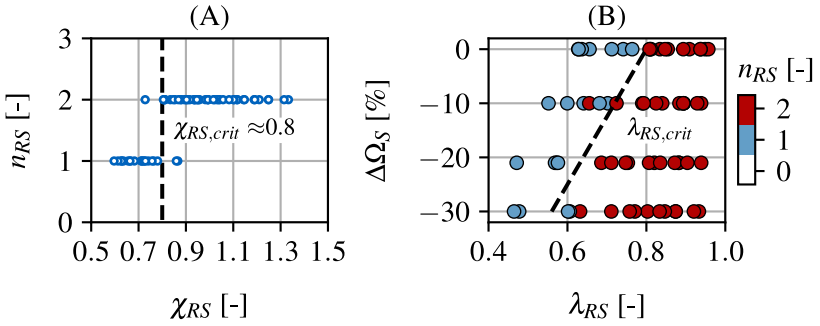

Figure 8.9: Correlation between the relative blockage χ_{RS}, the blockage factor λ_{RS} and the number of stall cells n_{RS}

8.6.3 Stall cell speed

In Section 7.7 a link between the differences in individual cell blockage $\Delta(\lambda_{RS}/n_{RS})$ and stall cell speed $\Delta\omega_{RS}/\Omega_S$ was already established. The discrepancy in the individual blockage was concluded to be the main reason for the offset in cell speed with respect to the high-fidelity computations. In the following, a deeper analysis of the correlation between both parameters is presented.

Depicted in Figure 8.10-A is the stall cell speed ω_{RS}/Ω_S against the individual blockage λ_{RS}/n_{RS} for the data derived from the design of experiments. Within the investigated design space only small differences in the cell speed can be observed. The results slightly suggest a trend of decreasing ω_{RS}/Ω_S towards increasing values of λ_{RS}/n_{RS}.

A clearer picture is illustrated in Figure 8.10-B. Included are all numerical results obtained from both, the high- and low-fidelity computations. The decreasing cell speed towards an increasing individual blockage is unmis-

takably identifiable. The trend is estimated by the regression line defined by Equation 8.9. Despite a less sophisticated R^2 of 71.7% compared to the previous models, the regression reflects the correlation sufficiently accurate. The cell speed is hence linked to the individual size of the stall cells.

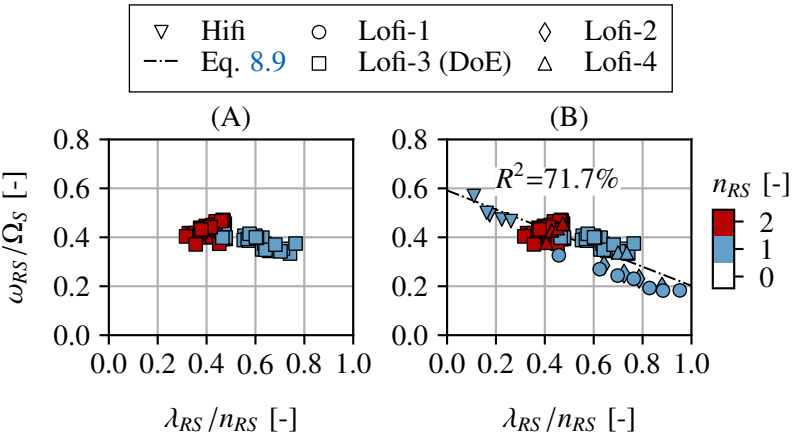

Figure 8.10: Correlation between the individual blockage λ_{RS}/n_{RS} and the stall cell speed ω_{RS}/Ω_S

$$\frac{\omega_{RS}}{\Omega_S} = -0.4 \cdot \frac{\lambda_{RS}}{n_{RS}} + 0.6 \tag{8.9}$$

8.7 Conclusions

In this chapter the impact of the geometric compressor parameters A^*/A, $\Delta\alpha$ and $\Delta\Omega_S$ on the stall cell details λ_{RS}, n_{RS} and ω_{RS}/Ω_S was investigated by means of a design of experiments. Based on the results, deeper analyses were performed having a closer look at the underlying mechanisms governing the cell details. With respect to the research questions defined in the beginning of this chapter, the following aspects can be concluded:

8.1-1 The stall cell size λ_{RS} was found to rise at decreasing nozzle area ratios as well as higher speeds and opened guide vanes.

8.1-2 The stall cell count n_{RS} was observed to increase towards smaller nozzle area ratios, reduced speeds and opened guide vanes.

8.1-3 For the stall cell speed an increase was generally exhibited towards reduced speeds and closed guide vanes. The impact of a decreasing nozzle area ratio was ambiguous, leading to a decrease in ω_{RS}/Ω_S for the single-cell pattern, but larger speeds for the twin-cell stall.

8.2-1 As the blockage factor λ_{RS} relies on the flow coefficient φ, the stall cell size increases linearly towards reduced flow rates. The corresponding growth rate depends on the location of the total-to-static characteristic within the compressor map and can be affected by e.g. guide vane angle variations.

8.2-2 For the stall cell count n_{RS} a correlation to the derived relative blockage χ_{RS} was found. The transition from the single-cell to the twin-cell pattern was exhibited at an critical value of $\chi_{RS,crit}$=0.8. As the parameter defines the ratio between the cell blockage λ_{RS} and the shaft speed Ω_S, the cells are observed to split up as they exceed a limiting size $\lambda_{RS,crit}$ at a constant speed. The magnitude of $\lambda_{RS,crit}$ decreases towards smaller speeds, wherefore the twin-cell pattern becomes the dominant disturbance.

8.2-3 With respect to the cell speed, a relation was found describing the decrease of ω_{RS}/Ω_S towards an increasing individual blockage λ_{RS}/n_{RS}.

Chapter 9
Transferability of findings

The findings derived in the previous chapter provide a deeper insight into the compressor parameter effects on rotating stall and allow for an interpretation of the underlying physical mechanisms.
As the knowledge was generated on the basis of defined use cases, this chapter aims at cross-validating the results with regard to additional compressor data. The objective is to examine the universal applicability and transferability of the findings. Therefore, experimental information from single- and multi-stage compressors is used where possible. With respect to the limited amount of available data, however, in some parts the verification can solely be performed rudimentarily.
The research questions defined in this chapter are as follows:

RQ 9.1 *Are the correlations predicting the stall cell speed (Eq. 8.9) and cell count change (Eq. 8.7) applicable to other compressors?*

RQ 9.2 *Do the operational parameters exhibit the same impact on rotating stall in other compressors?*

9.1 Governing relations

The stall cell speed ω_{RS}/Ω_S and number n_{RS} were observed to rely on the individual blockage λ_{RS}/n_{RS} and relative blockage χ_{RS}. Assuming a known blockage factor λ_{RS}, the relations can theoretically be used for rotating stall predictions. In the following, the general validity of Equations 8.7 and 8.9 is hence examined by applying them to different compressor builds.

9.1.1 Individual blockage

As validation case for the correlation between the stall cell speed ω_{RS}/Ω_S and the individual blockage λ_{RS}/n_{RS}, the three-stage axial compressor studied in Lavrich (1988) [43] is applied. The work comprised investigations of three different builds with high, medium and low reaction.
In Figure 9.1-A the measured data is plotted against the values predicted

by Equation 8.9. In general, a slight deviation between both datasets is apparent. While the propagation velocity is underpredicted at lower speeds, it is overpredicted towards higher values of ω_{RS}/Ω_S. The maximum absolute discrepancy is found to be 9.90% relative to the shaft speed.

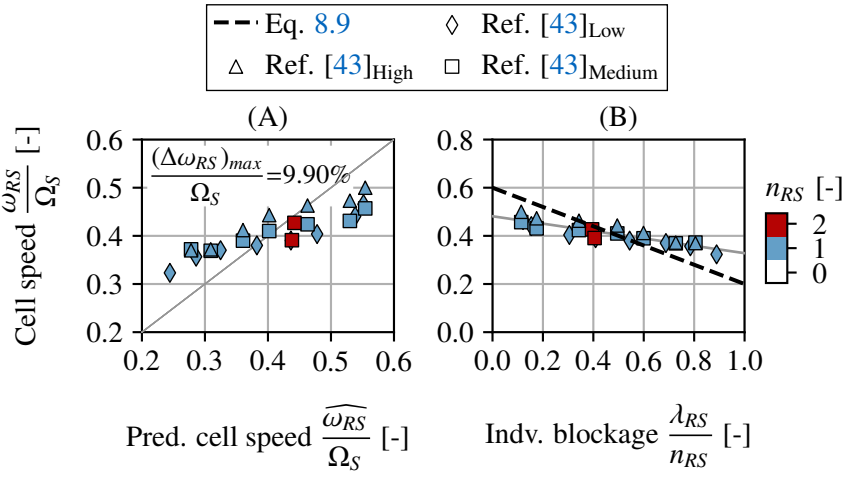

Figure 9.1: Differences in measured and predicted stall cell speed with respect to the three-stage axial compressor studied in Lavrich (1988) [43]

The relation between cell speed ω_{RS}/Ω_S and individual blockage λ_{RS}/n_{RS} for the multi-stage compressor is shown in Figure 9.1-B. Also included is the theoretical line based on Equation 8.9. Overall, the expected trend of diminishing cell speeds towards higher individual cell sizes is identifiable. The decrease, in turn, appears to be weaker than predicted by the model resulting in the previously observed differences. The correlation between ω_{RS}/Ω_S and λ_{RS}/n_{RS} is therefore assumed to differ for each compressor build. A more generic model for accurate predictions may hence have to include additional parameters like e.g. the number of compressor stages, as suggested by the data at hand.

9.1.2 Relative blockage

In section 8.6.2 the relative blockage χ_{RS} was derived in dependence upon the relative difference in shaft speed $\Delta\Omega_S$. Further validation of the parameter is hence only possible for compressors with an equal reference speed $\Omega_{S,ref}$. Therefore, experimental data cannot be considered at this point which subsequently leads to a verification based on computational results.

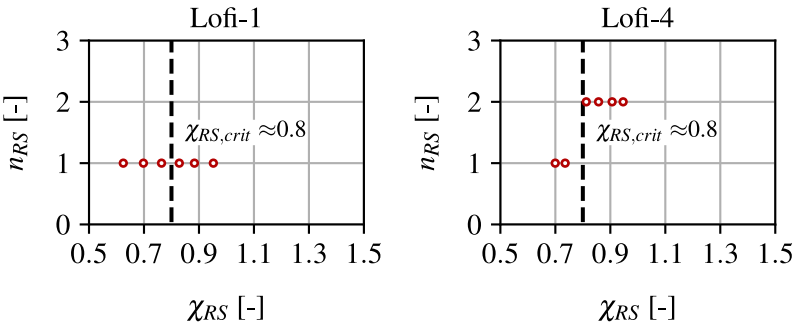

Figure 9.2: Correlation between the stall cell count n_{RS} and the relative blockage χ_{RS} for the reduced models Lofi-1 and Lofi-4

In Figure 9.2 the relationship between the stall cell count n_{RS} and the relative blockage χ_{RS} is presented for the Lofi-1 and Lofi-4 models. Also indicated is the previously derived critical value of $\chi_{RS,crit}$=0.8 denoting the transition from single- to twin-cell stall.
With respect to the Lofi-1 model the expected change in the number of stall cells at the defined boundary is seen to remain absent. The opposite, in turn, becomes apparent for the Lofi-4 model. In proximity to χ_{RS}=$\chi_{RS,crit}$=0.8, the cell count changes from one to two.
The cause for both observations is presumably traceable to the geometric deviations from the Lofi-3 model used to derive the parameter χ_{RS}. With the differences between Lofi-1 and Lofi-3 being comparably large, the prior findings are less transferable. As Lofi-3 and Lofi-4 by contrast, share the same span width at slightly different radial locations, the stall cell behaviour is alike.
The data generally indicates that the findings related to the relative block-

age are mainly transferable to compressors of similar architecture as Lofi-3. For other builds the critical value $\chi_{RS,crit}$=0.8 is hence not applicable and may be of different magnitude. For a more generic formulation able to predict the cell count change, further parameters as for example the hub-to-tip ratio r_h/r_t may be required. Additionally, a more general link to the rotational speed, independent of a reference speed, is needed. Despite these shortcomings, χ_{RS} remains the first non-dimensional quantity that has been found to explain the mechanisms involved in a cell count change. It hence represents a solid basis for future investigations.

9.2 Parameter effects

Previously, the impacts of different compressor parameters on the stall cell details were identified. As the findings are mainly based on the low-fidelity models, however, the established effects may only be valid for single-stage compressors with a high hub-to-tip ratio exclusively exhibiting full-span rotating stall.
The subsequent sections compare the parameter influences for varying compressor builds in order to determine similarities and differences. In case of deviating observations, interpretations are given on the basis of knowledge gained about the underlying stall mechanisms.

9.2.1 Shaft speed

The impact of the shaft speed Ω_S on the stall cell propagation velocity ω_{RS}/Ω_S is verified for three different datasets. These include the results of the DoE, experimental data of the TU Darmstadt test rig as well as measurements conducted in a multi-stage compressor of a large gas turbine. For all datasets constant cell counts and guide vane angles are considered to exclude additional interactions.
In Figure 9.3-A the findings of the DoE are shown in combination with data recorded in the TU Darmstadt compressor rig. Both incorporate a stall cell count of n_{RS}=1 and nominal guide vane angle of $\Delta\alpha$=0 degree. Clearly visible are the different trends in both sets at equal compressor shaft speeds. While the experimental data exhibits an increase of ω_{RS}/Ω_S with increasing $\Delta\Omega_S$, the computed results show a decrease in the relative stall cell speed.
The deviating trends are presumably based on the different rotating stall

types. With respect to the Lofi-3 model full-span stall was observed, comprising a large portion of the compressor annulus. As most of the blades operate at stalled conditions, an increase in shaft speed Ω_S is without significant impact on pressure ratio and mass flow rate. In other words, the axial velocity remains mainly unchanged in the single-stage build despite the higher rotor speeds. Due to the fixed axial velocity, however, the increase in Ω_S is accompanied by a decrease in the flow coefficient φ and hence a rising individual cell blockage λ_{RS}/n_{RS}. According to Figure 9.1, the decreasing individual blockage subsequently results in the diminished stall cell speed.

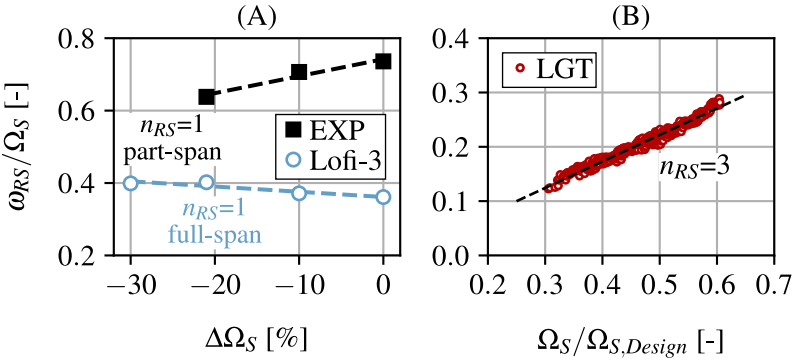

Figure 9.3: Influence of the compressor shaft speed Ω_S on the stall cell speed ω_{RS}/Ω_S for different compressor builds

On the basis of the conducted high-fidelity computations, in turn, the high hub-to-tip ratio single-stage compressor was concluded to initially exhibit part-span stall. With the disturbance hence comprising only a small fraction of the annulus ($\lambda_{RS} < 30\%$, see Day (1978) [15]), an increase in shaft speed still moves the operating point to higher pressure ratios and mass flow rates. Hence, together with the axial velocity, the flow coefficient φ rises leading to a decreasing individual blockage λ_{RS}/n_{RS}. Consequently, the stall cell speed is observed to increase towards higher compressor shaft speeds.

Figure 9.3-B presents the stall cell data acquired in a gas turbines multi-stage compressor. As the disturbance is usually evinced in the front-stages, a similar effect as concluded for the test rig is assumed. With

the rear-stages operating under stable conditions, increasing rotational speed Ω_S are accompanied with rising flow coefficients φ. Independent of the stalling type, part-span or full-span, the individual blockage hence reduces, wherefore the stall cell speed ω_{RS}/Ω_S increases.

9.2.2 Stagger angle

In the design of experiments, the influence of stagger angle variations with respect to the inlet guide vanes was investigated. In general, closing the rows was observed to decrease the blockage and increase the cell speed.

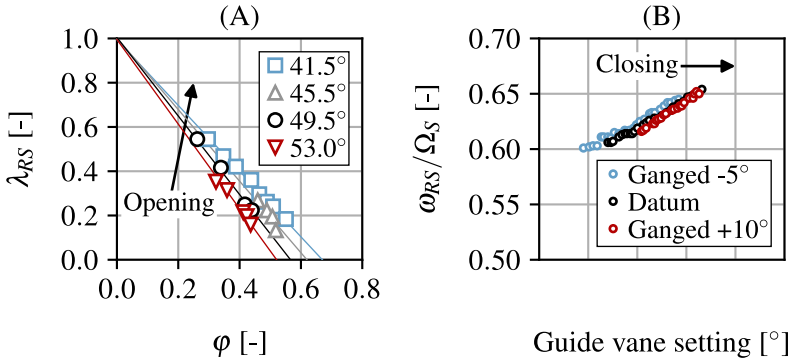

Figure 9.4: Impact of the rotor stagger angle on the stall cell size based on Fabri and Siestrunck (1957) [39] (A) and effect of guide vane angle variations on the stall cell speed extracted from Dodds (2016) [50] (B)

Figure 9.4-A illustrates the relation between stall cell size and flow coefficient for different rotor stagger angles. The data is based on experimental results of a single rotor investigated in Fabri and Siestrunck (1957) [39]. Clearly identifiable is the similarity to the guide vane angle impact previously presented in Figure 8.8. Opening the rotor at an otherwise constant flow coefficient can be seen to result in an increase in stall cell size. The effect diminishes towards smaller flow rates. The mechanism behind these trends is assumed to be identical to the principle described in Section 8.6.1. As the total-to-static performance curve is affected by the rotor

stagger angle, closing the row shifts the characteristic towards lower flow coefficients. Consequently, the parameter φ^* reduces, leading to an increasing blockage λ_{RS} and stall cell size.
The effect of guide vane angle adjustments on the stall cell speed in a multi-stage compressor is shown in Figure 9.4-B. The experimental data is extracted from Dodds (2016) [50]. The influence is depicted for three different schedules in which the offset between inlet guide vane and stator vane angle was -5°, nominal and +10°. Closing the vanes is noticeably resulting in an increase of the stall cell speed ω_{RS}/Ω_S. The trend is hence in agreement with findings derived from the design of experiments.

9.3 Conclusions

In this chapter the findings established in this work were put into a broader context by cross-validating them against additional data. Therefore, where possible, experimental results of single- and multi-stage compressors were used. Regarding the research questions specified in the introduction of this chapter, the subsequent conclusion are drawn:

9.1-1 The correlation between stall cell speed ω_{RS}/Ω_S and the individual blockage λ_{RS}/n_{RS} was found to generally reflect the correct trend in a multi-stage compressor. The maximum deviation of the predicted cell speed from the measured values was about 9.9%. The data suggests, that additional parameters such as the number of stages may have to be considered when deriving a universally applicable relation for cell speed predictions.

9.1-2 The relation between the number of stall cells n_{RS} and the relative blockage χ_{RS} was validated against the Lofi-1 and Lofi-4 model. While a cell count change remained absent at $\chi_{RS,crit}$=0.8 for the former, the theory correctly predicted the twin-cell pattern for Lofi-4. The results indicate that the transferability of the findings for χ_{RS} is limited to compressors alike the Lofi-3 model which was used to derive the parameter. However, since χ_{RS} is the first non-dimensional quantity able to explain the mechanisms involved in a cell count change, it represents a solid basis for future investigations.

9.2-1 The impact of the shaft speed Ω_S on the stall cell speed ω_{RS}/Ω_S at n_{RS}=const. was found to depend on the compressor build and type of stall. In general, however, the effect of the shaft speed on the flow coefficient is assumed to play a superior role. In case the stalled compressor still raises the mass flow rate during a ramp-up, the cell speed increases as well. Otherwise, the opposite trend can be expected.

9.2-2 The influence of rotor stagger angle adjustments on the stall cell size was observed to resemble the effect of guide vane angle variations. The impact of closing guide vanes on the stall cell speed in a multi-stage compressor was found to be comparable to the observations made for the design of experiments.

Chapter 10
Main conclusions and future work

Within the present work, the subject of rotating stall in axial flow compressors has been studied in order to tackle the current needs associated with the mitigation of the unsteady phenomenon. Therefore, a low-fidelity approach was developed that aims at predicting characteristic features like stall cell speed and number. The reduced-model was then applied for an in-depth parameter study pointing out sensitivities of rotating stall towards selected operational compressor features. From the analysis, driving mechanisms and relations were identified explaining the sensitivities on a more fundamental level. In the following, main conclusions are presented and possible future work on the subject is suggested.

10.1 Main conclusions

With respect to the main research questions (RQ 1.1-1.5) of this thesis, defined in Chapter 1, key findings and conclusions are presented.

1.1-1 In Chapter 3, different analytical and computational low-order models and methods were reviewed in order to identify the most suitable approaches for rotating stall predictions.
Of those able to derive the stall cell characteristics, such as speed and count, the approaches only resembling a fraction of the compressor annulus at a predefined radial location were found to be most promising. The reason for this is their comparably low complexity in combination with a generally good agreement with experimental data. More precisely, matching stall cell counts and discrepancies in cell speed of about ±10% were reported. The differences were assumed to have arisen from additionally introduced simplifications in order to reduce computational costs. Omitting these modifications was hence concluded to result in an increased prediction accuracy.

1.2-1 In order to provide a computational reference which the low-fidelity method could be compared to in greater detail, high-fidelity calculations were conducted and validated against experimental data in

Chapter 6.
The best results were achieved using the k-ω-SST model which was then applied to all computations in this work. With respect to the stall onset, the unsteady high-fidelity CFD disagreed by about -6.7% in flow rate and +6% in pressure rise. The accompanied spike-stall disturbance was correctly predicted with a discrepancy in propagation speed by about 1%. Subsequently, the computation matched the single-cell rotating stall with a difference of about 15% in relative stall cell speed and 7.9% in circumferential size. In addition, the calculations revealed a part-span tip-region stall reaching from 85% to 100% span.

1.2-2 For a more feasible prediction of the rotating stall, four different low-fidelity models were investigated in Chapter 7.
Each of the tested variations resembled only a fraction of the compressor tip region considering different radial locations and span widths. All of the models initially matched the single-cell rotating stall, whereas the minimum deviation in cell speed from the high-fidelity data was about -14.9% relative to the shaft speed. Despite the matching circumferential cell extent, the reduced models exhibited overall higher blockage factors and hence axial expansions of the stall cells into neighbouring rows. The discrepancy in cell speed was found to be linked to the difference in blockage factor and stall cell size. In order to obtain an accurate prediction of the propagation velocity, the low-fidelity models are hence required to match the blockage exhibited in the high-fidelity data. The findings, however, indicate that the impeded radial migration in the reduced domains is accompanied by initially higher blockage factors due to a delayed stall onset. Consequently, the approach is considered not suitable for predictions of part-span stall. In contrast, it might be more applicable to large disturbances such as full-span stall which explains the success of those models reported in the literature.

1.3-1 In Chapter 3, various studies on compressor features influencing the rotating stall characteristics (speed, count and size) were reviewed. Due to ambiguous observations and parameter interdependencies, the findings were inconclusive.
For a more precise determination of effects, a design of experiments

was presented in Chapter 8. As independent variables, the compressor shaft speed, the guide vane angle and the nozzle area ratio representing the throttle position were used.
By means of statistical modelling and analysis, the overall stall cell size was identified to rise towards decreasing nozzle area ratios, higher shaft speeds and opened guide vanes. For the stall cell count an increase was observed as the compressor was throttled, the speed was reduced or the vanes were opened. The relative stall cell speed, in turn, was exhibited to increase at smaller shaft speeds and closed guide vanes. The impact of a decreasing nozzle area ratio was found to depend on the stall cell count with a decelerating single-cell stall and an accelerating twin-cell pattern.

1.4-1 Based on an in-depth analysis of the design of experiments in Chapter 8, some of the underlying physical mechanisms determining the stall cell characteristics were identified.
As the blockage factor depends linearly on the flow coefficient, the stall cell size increases towards reduced flow rates or higher speeds. Additionally, the growth rate is affected by the location of the performance characteristic within the compressor map and hence increased by e.g. closed guide vanes.
The number of stall cells was found to depend on the relative blockage factor which represents the ratio between stall cell size and compressor shaft speed. As a critical value of 0.8 is exceeded, the single-cell stall transitions into a twin-cell pattern. The parameter indicates that for each speed the single-cell stall can only bear a maximum size until it splits up. The critical size was found to decrease towards smaller speeds, wherefore the twin-cell stall becomes the dominant disturbance.
With respect to the stall cell speed, a relation was found describing the decrease in propagation velocity towards higher individual stall cell sizes.

1.5-1 In order to verify generality and transferability, the results were cross-validated against additional compressor data in Chapter 9.
The correlation between stall cell speed and individual cell size was found to reflect the trend in a multi-stage compressor accurately with a maximum deviation of 9.9%. However, the data suggests

that additional parameters such as the number of stages may have to be considered for a universally applicable relation.
The correlation between the relative blockage factor and the cell count change was concluded to be mainly valid for compressor builds that are similar to the model used to derive the parameter. It is hence assumed that additional features like the hub-to-tip ratio may have to be included in the relation.
The effect of the shaft speed on the relative stall cell speed was found to depend on the compressor build and type of stall. In general, if the compressor is able to raise the mass flow rate during ramp up, the cell speed is likely to increase. Otherwise, decelerating cells are expected.

10.2 Future work

The high-fidelity results presented in Chapter 6 exhibited some discrepancies to the experimental data and left room for improvement. In order to ensure more accurate predictions of prospective rotating stall investigations, numerical as well as experimental sources of error have to be identified and eliminated. Possible enhancements of the computational setup are for example the integration of the strut and radial diffuser geometry to study the volume effects on the transient performance curve and development of the stall cell. Additionally, the number of time steps per pitch is considered as an important factor influencing e.g. the stall inception point. An increase might hence resolve disturbances on a smaller scale leading to a more accurate prediction of the stalling point. Moreover, the experimental operating point at stalled conditions is required to improve the validation. The measurement of the flow coefficient could for example be realised by hot-wire measurements.
With respect to the low-fidelity computations discussed in Chapter 7, a modal pre-stall disturbance propagating near rotor speed was observed. The propagation mechanism is assumed to be shock-related and associated with the upstream effect of discontinuities on the incoming flow. However, more evidence is required to prove this assumption.
In Chapter 8, the stall cell split-up was considered in greater detail and observed to originate from a difference in speed at the cell leading and trailing edges. Of particular interest is hence the cause of this speed difference which should be investigated in future work.

The transferability of certain findings derived from the design of experiments was concluded to be constraint in Chapter 9. The correlation between stall cell speed and individual cell size might hence be improved by including further compressor features such as the number of stages. Similar to this, the prediction of a cell count change on the basis of the relative blockage is assumed to enhance by including parameters such as the hub-to-tip ratio. Therefore, future studies should continue identifying relevant compressor and flow features determining the stall cell characteristics.

Bibliography

[1] M. Kaltschmitt and U. Neuling. Biokerosene - Status and Prospects. *Springer*, 2018.

[2] H. Ritchie and M. Roser. Energy. *Our World in Data*, 2020. www.ourworldindata.org/energy (Accessed in January 2021).

[3] S. C. Gülen. Gas Turbines for Electric Power Generation. *Cambridge University Press*, 2019.

[4] C. Lechner and J. Seume. Stationäre Gasturbinen. *Springer*, VDI-Book, 2019.

[5] S. Luo and S. Wu. Fatigue failure analysis of rotor compressor blades concerning the effect of rotating stall and surge. *Engineering Failure Analysis*, 68:1–9, 2016.

[6] N. Cumpsty. Compressor Aerodynamics. *Krieger Publishing Company*, 2004.

[7] T. R. Camp and I. J. Day. A Study of Spike and Modal Stall Phenomena in a Low-Speed Axial Compressor. *ASME Turbo Expo: Power for Land, Sea, and Air*, 1:V001T03A109, 1997.

[8] F. K. Moore and E. M. Greitzer. A Theory of Post-Stall Transients in Axial Compression Systems: Part I—Development of Equations. *ASME Journal of Engineering for Gas Turbines and Power*, 108(1):68–76, 1996.

[9] N. M. McDougall, N. A. Cumpsty, and T. P. Hynes. Stall Inception in Axial Compressors. *ASME Journal of Turbomachinery*, 112(1):116–123, 1990.

[10] I. J. Day. Stall Inception in Axial Flow Compressors. *ASME Journal of Turbomachinery*, 115(1):1–9, 1993.

[11] M. Inoue, M. Kuroumaru, T. Tanino, S. Yoshida, and M. Furukawa. Comparative Studies on Short and Long Length-Scale Stall Cell

Propagating in an Axial Compressor Rotor. *ASME Journal of Turbomachinery*, 123(1):24–30, 2000.

[12] G. Pullan, A. M. Young, I. J. Day, E. M. Greitzer, and Z. S. Spakovszky. Origins and Structure of Spike-Type Rotating Stall. *ASME Journal of Turbomachinery*, 137(5):051007, 2015.

[13] I. J. Day. Stall, Surge, and 75 Years of Research. *ASME Turbo Expo: Power for Land, Sea, and Air*, 6:V006T47A001, 2015.

[14] H. Grieb. Verdichter für Turbo-Flugtriebwerke. *Springer*, 2009.

[15] I. J. Day, E. M. Greitzer, and N. A. Cumpsty. Prediction of Compressor Performance in Rotating Stall. *ASME Journal of Engineering for Gas Turbines and Power*, 100(1):1–12, 1978.

[16] H. Emmons, C. Pearson, and H. Grant. Compressor Surge and Stall Propogation. *Transactions of the ASME*, 77:455–469, 1955.

[17] I. J. Day. Axial compressor stall. *University of Cambridge*, Ph.D. thesis, 1976.

[18] J. Dodds and M. Vahdati. Rotating Stall Observations in a High Speed Compressor—Part II: Numerical Study. *ASME Journal of Turbomachinery*, 137(5):051003, 2015.

[19] W. Bräunling. Flugzeugtriebwerke: Grundlagen, Aero-Thermodynamik, Kreisprozesse, thermische Turbomaschinen, Komponenten- und Auslegungsberechnungen. *Springer*, VDI-Book, 2001.

[20] J. P. Longley and T. P. Hynes. Stability of Flow Through Multistage Axial Compressors. *ASME Journal of Turbomachinery*, 112(1):126–132, 1990.

[21] N. A. Cumpsty and E. M. Greitzer. A Simple Model for Compressor Stall Cell Propagation. *ASME Journal of Engineering for Gas Turbines and Power*, 104(1):170–176, 1982.

[22] F. K. Moore. A Theory of Rotating Stall of Multistage Axial Compressors: Part I-Small Disturbances. *ASME Journal of Engineering for Gas Turbines and Power*, 106(2):313–320, 1984.

[23] F. K. Moore. A Theory of Rotating Stall of Multistage Axial Compressors: Part II-Finite Disturbances. *ASME Journal of Engineering for Gas Turbines and Power*, 106(2):321–326, 1984.

[24] F. K. Moore. A Theory of Rotating Stall of Multistage Axial Compressors: Part III-Limit Cycles. *ASME Journal of Engineering for Gas Turbines and Power*, 106(2):327–334, 1984.

[25] E. M. Greitzer and F. K. Moore. A Theory of Post-Stall Transients in Axial Compression Systems: Part II—Application. *ASME Journal of Engineering for Gas Turbines and Power*, 108(2):231–239, 1996.

[26] C. Backi, J. Gravdahl, and S. Skogestad. Robust control of a two-state Greitzer compressor model by state-feedback linearization. *Proceedings of the 2016 IEEE Multi-Conference on Systems and Control*, pages 1226–1231, 2016.

[27] C. Hős, A. Champneys, and L. Kullmann. Bifurcation analysis of surge and rotating stall in the Moore–Greitzer compression system. *IMA Journal of Applied Mathematics*, 68(2):205–228, 2003.

[28] J. T. Gravdahl and O. Egeland. A Moore-Greitzer axial compressor model with spool dynamics. *Proceedings of the 36th IEEE Conference on Decision and Control*, 5:4714–4719, 1997.

[29] T. Nishizawa and H. Takata. Numerical Study on Rotating Stall in Finite Pitch Cascades. *ASME Turbo Expo: Power for Land, Sea, and Air*, 1:V001T01A094, 1994.

[30] A. R. Kriebel, B. S. Seidel, and R. G. Schwind. Stall Propagation in a Cascade of Airfoils. *NASA Technical Report*, R-61, 1960.

[31] E. Outa, D. Kato, and K. Chiba. An N-S Simulation of Stall Cell Behavior in a 2-D Compressor Rotor-Stator System at Various Loads. *ASME Turbo Expo: Power for Land, Sea, and Air*, 1:V001T01A093, 1994.

[32] H. M. Saxer-Felici, A. P. Saxer, A. Inderbitzin, and G. Gyarmathy. Prediction and Measurement of Rotating Stall Cells in an Axial Compressor. *ASME Journal of Turbomachinery*, 121(2):365–375, 1999.

[33] M. Ferlauto and S. R. Taddei. Reduced order modelling of full-span rotating stall for the flow control simulation of axial compressors. *Proceedings of the Institution of Mechanical Engineers, Part A: Journal of Power and Energy*, 229(4):352–366, 2015.

[34] D. R. Seyler and J. P. Gostelow. Single stage experimental evaluation of high Mach number compressor rotor blading. Part 2 - performance of rotor 1B. *NASA*, CR-54582, 1967.

[35] M. Righi, V. Pachidis, L. Könözsy, and L. Pawsey. Three-dimensional through-flow modelling of axial flow compressor rotating stall and surge. *Aerospace Science and Technology*, 78:271–279, 2018.

[36] A. H. J. Eastland. An Experimental Investigation of Compressor Performance in Rotating Stall. *Massachusetts Institute of Technology*, Ph.D. thesis, 1982.

[37] R. N. Gamache. Axial Compressor Reversed Flow Performance. *Massachusetts Institute of Technology*, Ph.D. thesis, 1985.

[38] D. Romera and R. Corral. Efficient Passage-Spectral Method for Unsteady Flows Under Stall Conditions. *ASME Turbo Expo: Power for Land, Sea, and Air*, Volume 2C: Turbomachinery:V02CT41A035, 2019.

[39] J. Fabri and R. Siestrunck. Rotating Stall in Axial Flow Compressors. *Journal of the Aeronautical Sciences*, 24(11):805–812, 1957.

[40] S. Tanaka and S. Murata. On the Partial Flow Rate Performance of Axial-Flow Compressor and Rotating Stall : 1 st Report, Influences of Hub-Tip Ratio and Stators. *Bulletin of JSME*, 18(117):256–263, 1975.

[41] A. R. Hickman and S. C. Morris. Characteristics of Stable Rotating Stall Cells in an Axial Compressor. *ASME Turbo Expo: Power for Land, Sea, and Air*, 2D:V02DT46A029, 2017.

[42] A. R. Hickman and S. C. Morris. Observations of the Growth and Decay of Stall Cells during Stall and Surge in an Axial Compressor. *Hindawi International Journal of Rotating Machinery*, 2017.

[43] P. L. Lavrich. Time resolved measurements of rotating stall in axial flow compressors. *Massachusetts Institute of Technology*, Ph.D. thesis, 1988.

[44] E. L. Costilow and M. Huppert. Some effects of guide-vane turning and stators on the rotating stall characteristics of a high hub-tip ratio single stage compressor. *NACA*, TN 3711, 1956.

[45] F. H. Calvert, A. A. Medeiros, and J. D. F. Effect of inlet-guide-vane angle on blade vibration and rotating stall of 13-stage-axial-flow compressor in turbojet engine. *NACA*, RM-E55K03, 1956.

[46] M. Choi, M. Vahdati, and M. Imregun. Effects of Fan Speed on Rotating Stall Inception and Recovery. *ASME Journal of Turbomachinery*, 133(4):041013, 2011.

[47] M. Choi, N. H. S. Smith, and M. Vahdati. Validation of Numerical Simulation for Rotating Stall in a Transonic Fan. *ASME Journal of Turbomachinery*, 135(2):021004, 2012.

[48] M. Huppert, H. F. Calvert, and A. J. Meyer. Experimental investigation of rotating stall and blade vibration in the axial-flow compressor of a turbojet engine. *NACA*, RM E54A08, 1954.

[49] J. Dodds and M. Vahdati. Rotating Stall Observations in a High Speed Compressor—Part I: Experimental Study. *ASME Journal of Turbomachinery*, 137:051002, 2015.

[50] J. Dodds. Rotating stall in variable geometry compressors. *Imperial College London*, Ph.D. thesis, 2016.

[51] C. Kunkel, J. Werner, D. Franke, H.-P. Schiffer, F. Wartzek, C. Biela, and C. Starke. Introduction and Commissioning of the New Darmstadt Transonic Compressor Test Facility. *ASME Turbo Expo: Power for Land, Sea, and Air*, 2A:V02AT39A023, 2019.

[52] C. Kunkel and J. Werner. Detaillierte Vermessung einer dreidimensional optimierten transsonischen Verdichterbeschaufelung. *Final report of the AG-Turbo COOREFLEX project 1.2.5a*, 2019.

[53] J. D. Denton. Some Limitations of Turbomachinery CFD. *ASME Turbo Expo: Power for Land, Sea, and Air*, 2010.

[54] M. Vahdati, G. Simpson, and M. Imregun. Unsteady Flow and Aeroelasticity Behavior of Aeroengine Core Compressors During Rotating Stall and Surge. *ASME Journal of Turbomachinery*, 130(3):031017, 2008.

[55] N. Gourdain, S. Burguburu, F. Leboeuf, and G. J. Michon. Simulation of rotating stall in a whole stage of an axial compressor. *Computers and Fluids*, 39(9):1644 – 1655, 2010.

[56] M. Choi and M. Vahdati. Numerical strategies for capturing rotating stall in fan. *Proceedings of the Institution of Mechanical Engineers, Part A: Journal of Power and Energy*, 225(5):655–664, 2011.

[57] Y. Li and A. Sayma. Effects of Blade Damage on the Performance of a Transonic Axial Compressor Rotor. *ASME Turbo Expo: Power for Land, Sea, and Air*, 8:2427–2437, 2012.

[58] Y. Li. Numerical Simulations of Rotating Stall in Axial Flow Compressors. *University of Sussex*, Ph.D. thesis, 2013.

[59] K.-B. Lee, J. Dodds, M. Wilson, and M. Vahdati. Validation of a Numerical Model for Predicting Stalled Flows in a Low-Speed Fan—Part II: Unsteady Analysis. *ASME Journal of Turbomachinery*, 140(5):051009, 2018.

[60] S. Kim, G. Pullan, C. A. Hall, R. P. Grewe, M. J. Wilson, and E. Gunn. Stall Inception in Low-Pressure Ratio Fans. *Journal of Turbomachinery*, 141(7):071005, 2019.

[61] G. Ashcroft, K. Heitkamp, and E. Kuegeler. High-Order Accurate Implicit Runge-Kutta Schemes for the Simulation of Unsteady Flow Phenomena in Turbomachinery. *ECCOMAS CFD*, 2010.

[62] K. Becker, K. Heitkamp, and E. Kuegeler. Recent Progress In A Hybrid-Grid CFD Solver For Turbomachinery Flows. *ECCOMAS CFD*, 2010.

[63] German Aerospace Center (DLR). TRACE User Guide. *TRACE*, 2018. www.trace-portal.de/userguide/trace (Accessed in January 2021).

[64] P. Spalart and S. Allmaras. A One-Equation Turbulence Model for Aerodynamic Flows. *AIAA 30th Aerospace Sciences Meeting and Exhibit. AIAA*, 439, 1992.

[65] F. Menter, M. Kuntz, and R. Langtry. Ten Years of Industrial Experience with the SST Turbulence Model. *Heat and Mass Transfer*, 4, 2003.

[66] M. Vahdati, A. I. Sayma, C. Freeman, and M. Imregun. On the Use of Atmospheric Boundary Conditions for Axial-Flow Compressor Stall Simulations. *ASME Journal of Turbomachinery*, 127(2):349–351, 2004.

[67] W. Zhang and M. Vahdati. A Parametric Study of the Effects of Inlet Distortion on Fan Aerodynamic Stability. *ASME Turbo Expo: Power for Land, Sea, and Air*, 2A:V02AT39A036, 2018.

[68] W. Zhang, S. Stapelfeldt, and M. Vahdati. Influence of the inlet distortion on fan stall margin at different rotational speeds. *Aerospace Science and Technology*, 98:105668, 2020.

[69] F. Crevel, N. Gourdain, and S. Moreau. Numerical Simulation of Aerodynamic Instabilities in a Multistage High-Speed High-Pressure Compressor on Its Test-Rig—Part I: Rotating Stall. *ASME Journal of Turbomachinery*, 136(10):101003, 2014.

[70] J. W. Cooley and J. W. Tukey. An Algorithm for the Machine Calculation of Complex Fourier Series. *Mathematics of Computation*, 19(90):297–301, 1965.

[71] M. Gasior and J. L. Gonzalez. Improving FFT Frequency Measurement Resolution by Parabolic and Gaussian Spectrum Interpolation. *AIP Conference Proceedings*, 732(1):276–285, 2004.

[72] R. B. Blackman and J. W. Tukey. The measurement of power spectra from the point of view of communications engineering — Part I. *The Bell System Technical Journal*, 37(1):185–282, 1958.

[73] J. S. Bendat and P. A. G. Random Data: Analysis and Measurement Procedures, Fourth Edition. *John Wiley & Sons*, 2010.

[74] A. Gnanasampanthan. Strömungssimulation eines 1.5 stufigen Verdichters mit dem Strömungslöser TRACE. *Siemens AG / University of Duisburg-Essen*, Master thesis, 2019.

[75] D. C. Wilcox. Reassessment of the scale-determining equation for advanced turbulence models. *AIAA Journal*, 26(11):1299–1310, 1988.

[76] S. Lieblein, F. C. Schwenk, and R. L. Broderick. Diffusion factor for estimating losses and limiting blade loadings in axial-flow-compressor blade elements. *NACA Research Memorandum*, NACA-RM-E53D01, 1953.